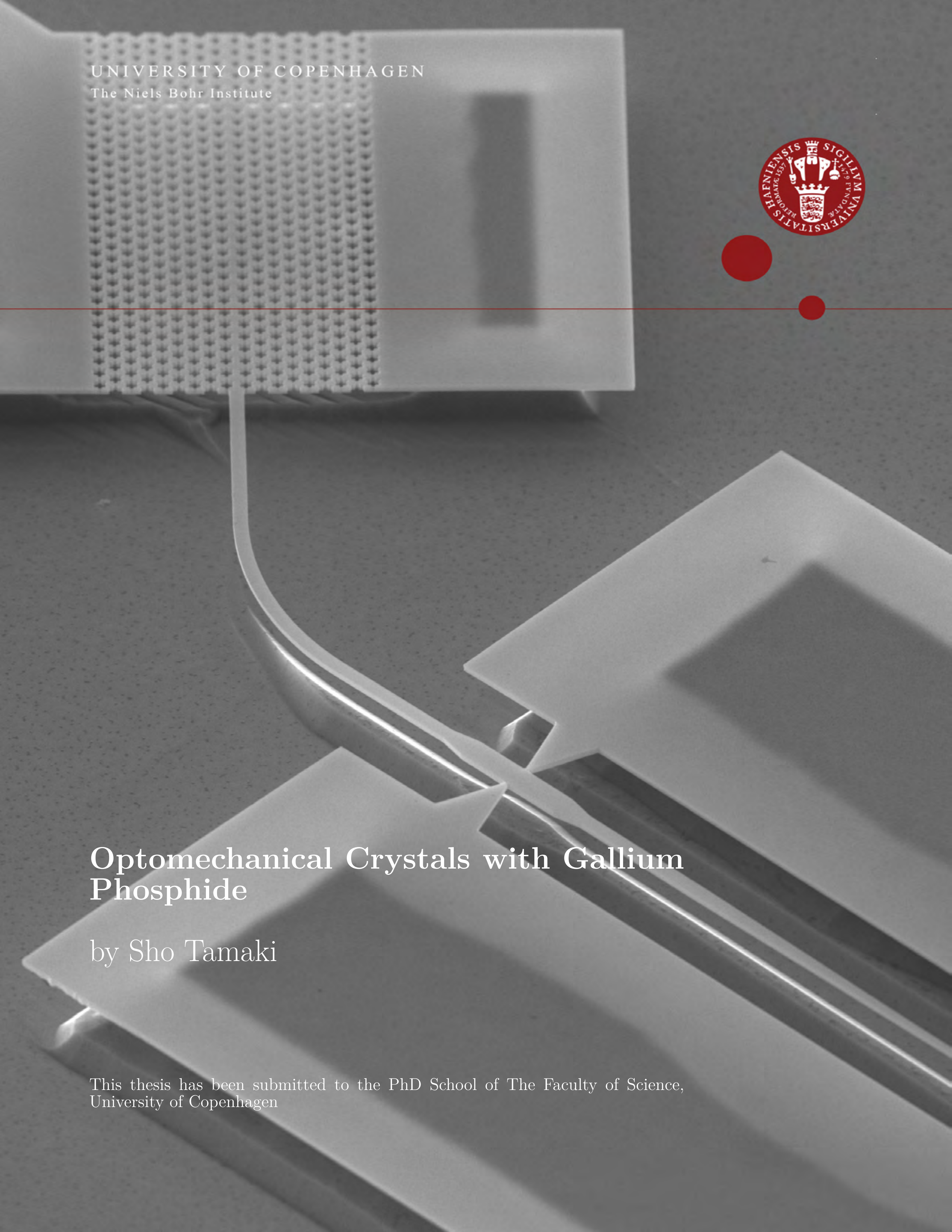

UNIVERSITY OF COPENHAGEN
The Niels Bohr Institute

Optomechanical Crystals with Gallium Phosphide

by Sho Tamaki

This thesis has been submitted to the PhD School of The Faculty of Science,
University of Copenhagen

Academic Supervisor: Prof. Albert Schliesser

External Referees: Dr. Paul Seidler
Prof. Simon Gröblacher

Internal Referee: Assoc. Prof. Leonardo Midolo

Submission Date: 03 October 2024

Abstract

Faithful quantum state transfer between telecom photons and microwave frequency mechanical oscillations necessitate a fast conversion rate and low thermal noise. Gallium Phosphide (GaP) is a promising material thanks to its large electronic bandgap of 2.26 eV, which suppresses two-photon absorption, and to its high refractive index n = 3.05 at the telecom C-band, leading to a high-Q optical mode.

In this thesis, we propose 2 designs of optomechanical crystals (OMCs) made of GaP. The first design is two-dimensional OMC which enables sufficiently high mechanical frequency (1-10 GHz). This places our device in the resolved-sideband regime, a prerequisite for many quantum protocols. It can also support higher thermal conductance than 1D structures, mitigating the parasitic laser absorption heating. The other design is a Su–Schrieffer–Heeger (SSH) based topological nanobeam. The topologically protected optical and mechanical modes are expected to be robust against geometrical impurity and to have consistent eigenfrequencies. This will make those modes indistinguishable and thus suitable for quantum communication and computations.

We fabricate and characterise the 2D OMC made of GaP. We realise a high optical Q-factor of 7.9×10^4, corresponding to a linewidth $\kappa/2\pi = 2.5$ GHz at the telecom frequency 195.6 THz. This optical mode couples to several mechanical modes, whose frequencies all exceed the optical linewidth. The most strongly coupled mode oscillates at 7.7 GHz, more than 3 times the optical linewidth, while achieving a substantial vacuum optomechanical coupling rate $g_0/2\pi = 450$ kHz. This makes the platform a promising candidate for a long-lived, deterministic quantum memory for telecom photons at low temperatures.

Resumé

Trofast kvantetilstandsoverførsel mellem telekommunikationsfotoner og mekaniske svingninger i mikrobølgefrekvenser nødvendiggør en hurtig konverteringshastighed og lav termisk støj. Gallium phosphid (GaP) er et lovende materiale takket være dets store elektroniske båndgab på 2.26 eV, som undertrykker to-fotonsabsorption, og til sit høje brydningsindeks n = 3.05 ved telekommunikations C-båndet, hvilket fører til en optisk tilstand med høj Q-faktor.

I denne afhandling foreslår vi 2 designs af optomekaniske krystaller (OMC'er) lavet af GaP. Det første design er todimensionel OMC, som muliggør tilstrækkelig høj mekanisk frekvens (1-10 GHz). Dette placerer vores enhed i regimet med opløst sidebånd, en forudsætning for mange kvanteprotokoller. Det kan også understøtte højere termisk ledningsevne end 1D-strukturer, hvilket mindsker den parasitære opvarmning fra laserabsorption. Det andet design er en Su–Schrieffer–Heeger (SSH) baseret topologisk nanostråle. De topologisk beskyttede optiske og mekaniske tilstande forventes at være robuste over for geometriske urenheder og at have ensartede egenfrekvenser. Dette vil gøre disse tilstande ens og dermed egnede til kvantekommunikation og beregninger.

Vi fremstiller og karakteriserer 2D OMC lavet af GaP. Vi realiserer en høj optisk Q-faktor på 7.9×10^4, svarende til en linjebredde $\kappa/2\pi = 2.5$ GHz ved telefrekvensen 195.6 THz. Denne optiske tilstand kobles til flere mekaniske tilstande, hvis frekvenser alle overstiger resonatorens linjebredde. Den stærkest koblede tilstand oscillerer ved 7.7 GHz, mere end 3 gange den optiske linjebredde, samtidig med at den opnår en betydelig optomekanisk vakuumkoblingshastighed $g_0/2\pi = 450$ kHz. Dette gør platformen til en lovende kandidat til en langvarig, deterministisk kvantehukommelse til telekommunikationsfotoner ved lave temperaturer.

Acknowledgements

This thesis would not have been possible without the support and encouragement of many individuals, to whom I am deeply grateful.

First and foremost, I express my deepest gratitude to my academic supervisor, Albert Schliesser, for offering me this exciting project. I would like to thank my splendid SLAB colleagues Eric L., Thibault, Felix, Xiang, Ilia, Teresa, Aida, Andrea, Michael, Leopold, Clinton, and Vishnu for helping with experiments, having discussions and just having fun. I would also like to acknowledge the legendary alumni members Mads, Lucio, Eric P., Letizia, Yannick, Nenad, and Sampo, who have greatly enriched my PhD life. I appreciate cheerful office mates Felix, Atefeh, Eric L., Patrik, and Carlos, for creating such a supportive and lively environment. My appreciation also goes to Théo and Rémy at C2N for device preparation and advice for the initial stage of the experiment. Thanks to everyone in the Center for Hybrid Quantum Networks (Hy-Q) at the Niels Bohr Institute.

I am deeply grateful to those who encouraged me to engage socially through playing board games, football, badminton, and other activities which provided me with a good work-life balance.

And finally, I would like to express my heartfelt gratitude to my family and friends for their unwavering support throughout these three and a half years.

Table of Contents

List of Figures

Chapter 1

Introduction

Since the invention of the laser [1] and the following optical tweezer technique [2], the coherent electromagnetic field has been an excellent tool to access the degree of freedom of mechanical motion. The application ranges from controlling the motion of atoms to micro- or nano-objects. Cavity optomechanics has emerged where the light field is confined in an optical cavity effectively enhancing the radiation pressure onto the objects. This hybrid system has enabled us not only to access mechanical motion but also to study the interplay between optical and mechanical oscillators with completely different frequencies.

After witnessing milestones such as ground state cooling [3], strong coupling [4], and measurement below the standard quantum limit [5], this field has entered a new era where those techniques are to be implemented to quantum technologies. One of the particularly interesting applications is the mechanical quantum memory [6], a device that can store information of a single photon, then it can be read out after a desired time. Such a device is a key component of the quantum repeater protocol [7], a method to send quantum information over long distances. The first demonstration of quantum memory [8] and repeater [9] were realised by using atomic gases. Cavity optomechanical systems have gained significant attention in recent researches [6, 10, 11], driven by the growing demand for telecom-band quantum memories, which remain challenging to achieve with atomic systems.

However, despite decades of rapid and intense progress, the optical heating of mechanical motion caused by incoherent absorption has remained. This degrades the mechanical coherence time with an increase of the thermal bath temperature [12, 13]. In the case of quantum memory, this limits the storage time and information conversion efficiency. Since mechanical coherence plays an important role in various applications, this is a common problem to overcome for better performance.

A possible solution is to find a material that absorbs less light and still shows decent optical and mechanical performance. One of the dominant origins of heat is the two-photon absorption by electrons, which is determined by the band gap (note that surface roughness and impurity also cause laser heating together with the bulk properties). When a single-photon energy of the driving laser exceeds half of the bandgap energy, this nonlinear phenomenon occurs according to the laser intensity. For that, a wide electron bandgap is a prerequisite to suppress temperature increases.

Considering the above background, we propose gallium phosphide (GaP) optomechanical systems. Recent studies [14, 15] have suggested GaP as a favourable choice among many material candidates thanks to several properties. First, it has a large electronic bandgap of 2.26 eV exceeding the energy of two telecom photons ($\sim$1.6 eV), which can suppress the two-photon-absorption-induced heating. Second, its relatively high refractive index $n = 3.05$ enables a high-Q optical mode and good vacuum optomechanical coupling rate g_0, requiring less driving laser power. On top of that, GaP inherently possesses sufficient piezoelectricity. This enables mechanical-microwave coupling [16, 17] without the need to deposit additional piezoelectric materials, such as an AlN layer on top of the silicon medium [18]. Therefore, there will be less risk of degrading the mechanical and optical properties and less fabrication complexity.

In this thesis, we explore the GaP platform for developing optomechanical crystals (OMCs) [19]. Among a wide variety of cavity optomechanical systems, the OMCs exceptionally stand out thanks to their high degrees of freedom in structural design as well as their relatively strong optomechanical coupling rate. Therefore, many efforts have enriched the field by providing unique structural concepts such as two-dimensional [20, 21], topological [22, 23], and clamped [24] structures. OMCs are also known as promising platforms to connect cavity optomechanics to microwave photons with the help of their high mechanical frequencies $\sim$GHz. In this thesis, we propose two different classes of OMC designs; a two-dimensional design based on the snowflake holes [21], and a one-dimensional topological structure inspired by the Su–Schrieffer–Heeger (SSH) topological chain model [25].

Our 2D structure is motivated by the need for an even more robust device to release the laser heating problem. Recent studies [13, 22] have suggested that 2D OMCs, compared to conventional 1D OMCs, are advantageous for solving the heating problem. That is because the geometries allow the thermal phonons to dissipate faster than other structures, suppressing temperature increase. They can also achieve higher mechanical frequencies than 1D structures making thermal occupation lower at the same temperature and the sideband-resolved regime easier.

The other work on SSH topological design is encouraged by the demand for consistent performance on optical/mechanical frequencies over many fabricated devices. This is due to the fact that their implementation in quantum operations, such as the generation of entangled states [26] or the occurrence of Hong-Ou-Mandel interference [27], necessitates indistinguishable modes. The topologically protected mode will enable fabricated devices to possess reduced eigenfrequency deviation, thus leading to indistinguishable modes. We especially, employ an edge mode of SSH topological design consisting of periodical dimers in 1D nanobeam.

This thesis begins with basic knowledge of cavity optomechanics in chapter 2 covering the historical discovery of radiation pressure and theoretical treatment of more modern cavity optomechanical systems. Then, in chapter 3, we provide the working principle and recent progress of OMCs. The optomechanical coupling mechanisms, namely the moving boundary and photoelastic contributions are explained. This chapter also provides a broad map of material differences. Next, in chapter 4, we move on to the device geometry, presenting our 2D design and simulation results. The design procedure starts with unit cell simulation and then induces the line defect followed by the 2D defect. In the same chapter, we also see our evanescent fibre coupling strategy. Chapter 5 presents simulated results of another SSH-based design, where correspondence to the polyacetylene molecules is also discussed. Chapter 6 shows details of device fabrication including fibre etching. With the resulting device, we carry out the characterisation experiments in chapter 7. The optical and mechanical spectrum is analysed including the dynamical backaction effect on the mechanical frequency and linewidth. The vacuum optomechanical coupling rate is estimated using the calibration method. The thesis is then concluded in chapter 8.

Chapter 2

Cavity Optomechanics

This chapter introduces the basic concept and theoretical background of cavity optomechanics. We start with the historical discovery of optical radiation and then move on to the principle of cavity optomechanics considering the Fabry-Pérot cavity example. The corresponding Hamiltonian and the time evolution derived from the quantum Langevin equations are explained. Furthermore, we see how the system behaves differently according to the laser detuning, by introducing an approximation method called linearisation.

2.1 Radiation Pressure

The nature of light has been at the centre of enormous interest for millenniums as it has strongly been related to our eyesight, on which we rely on a lot of information we receive. However, it was not until the 17th century that Johannes Kepler postulated for the first time that light may exert force on objects [28], now called radiation pressure or optical force (actually, a comet has several tails due to the existence of solar wind as well as the radiation. This combined effect creates several tails made of different materials, gasses or debris). The discovery was deduced from the observation fact that a comet's tails always point in the opposite direction to the sun. Surprisingly, ancient Chinese astronomers left detailed records on comet tails in 7th-century BCE [29] in which they already pointed out that the direction is opposite to the sun.

With classical electromagnetism, the radiation pressure on comet tails is well understood as the result of energy transportation from electromagnetic

(EM) waves to the object. This is due to the energy flux (energy transport per time and space) of the EM wave given by the Poyinting vector **S**:

$$\mathbf{S} = \mathbf{E} \times \mathbf{H}, \tag{2.1}$$

where **E** and **H** are the electric field and magnetic field strength. Objects receive force when the EM energy is converted to its kinetic energy. On the other hand, from the particle picture of quantum mechanics, the force is described as the momentum transport from photons to the object through reflection, deflection, and absorption. The energy of a particle from the special relativity is given as:

$$E^2 = (m_0 c^2)^2 + (cp)^2, \tag{2.2}$$

where we define the relativistic energy of a particle E, invariant mass m_0, the speed of light in vacuum c, and momentum p. For a photon, $m_0 = 0$, the absolute value of the momentum becomes $p = E/c$. When a photon impinges on and is perfectly reflected by an object, the object obtains $2p$ of momentum as a result of the conservation of momentum and thus feels force.

However, it was only after the invention of the laser [1] that researchers began to control/manipulate objects through radiation pressure since the pressure by natural light or light bulbs is extremely tiny and non-directional. One of the first milestones was the optical tweezers [2, 30] demonstrated by Ashkin *et al.*, where a laser is used to trap a micro-particle with its radiation pressure. In those experiments, the laser beam is focused with a lens to create a strong intensity gradient with which tiny particles feel a so-called gradient force. Note that the gradient force is based on the wave behaviour of light, which is essentially a wave behaviour different from the particle behaviour of the momentum transfer from photons to objects. This optical tweezer technique is now widely implemented ranging from single-molecule studies to cell biology [31].

Despite these significant achievements, radiation pressure can occasionally impair certain applications. Researchers have revealed the sensitivity of gravitational detectors (more generally, the precision of measured displacement of any objects) is affected by laser noise through radiation pressure also known as quantum backaction. This originates from the quantum fluctuation in the number of photons by a laser (namely, intensity fluctuation), which works as a noise to the mirror displacement [32], and thus it increases as laser power. In the weak laser intensity regime, the phase fluctuation also

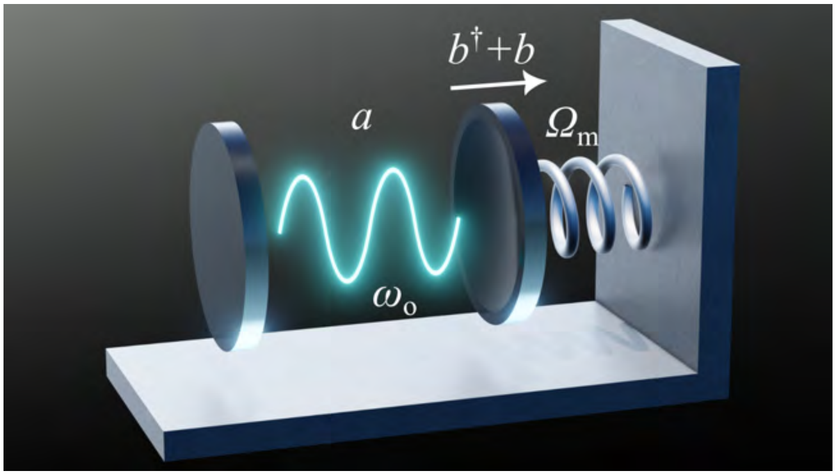

Figure 2.1: Schematic image of a Fabry-Pérot type optomechanical system. An optical cavity mode a with eigenfrequency ω_o is coupled to a movable mirror b with mechanical frequency Ω_m through the change in cavity length.

induces imprecision noise which inversely scales with laser power. With the combination of these noises, the limitation known as the standard quantum limit (SQL) [33] emerges, establishing a lower bound of the measurement precision.

2.2 Principle of Optomechanics

With technological progress in micro- and nano-device fabrication in the 21st century, combined with laser optics, there came a fairly new and active research field called 'Cavity Optomechanics' [34]. There, the interaction between the optical resonator and mechanical vibrations is investigated with the aim of enhancing measurement sensitivity and exploring its potential as a novel tool for quantum technology. The interaction between the optical and mechanical modes is often explained through a Fabry-Pérot optical cavity with a moving end mirror attached to a spring as drawn in Fig. 2.1. The Hamiltonian of this closed system $\hat{H}_0$ is given as:

$$\frac{\hat{H}_0}{\hbar} = \omega_\mathrm{o}\hat{a}^\dagger\hat{a} + \Omega_\mathrm{m}\hat{b}^\dagger\hat{b} - g_0\hat{a}^\dagger\hat{a}\left(\hat{b}^\dagger + \hat{b}\right), \tag{2.3}$$

where we define bosonic annihilation operator of cavity photon $\hat{a}$ and mechanical vibration $\hat{b}$, eigenfrequency of the optical mode ω_{o} and mechanical mode Ω_{m}, and the vacuum optomechanical coupling rate g_0. The origin of this Hamiltonian can be understood as follows: the mechanical displacement $\hat{x} := \hat{b}^\dagger + \hat{b}$ shifts the optical eigenfrequency by $-g_0\hat{x}$ since it depends on the cavity length. Note that in this situation, the actual displacement of the moving mirror X is given as $X = x_{\mathrm{zpf}}\,\langle\hat{x}\rangle$, where $x_{\mathrm{zpf}} = \sqrt{\hbar/m_{\mathrm{eff}}\Omega_{\mathrm{m}}}$ is the zero-point fluctuation of the mechanical vibration and m_{eff} is the effective mass of the vibration (mass of the mirror in this case). However, generally speaking, X is not always a suitable value to be considered. This is because many systems, such as toroidal micro-cavities or optomechanical crystals, have a multi-dimensional distribution of mechanical displacement. And the actual displacement becomes position-dependent $X(\mathbf{r})$ and it is hard to choose at which point X should be defined. Therefore, the unitless displacement operator $\hat{x}$ or the annihilation operator $\hat{b}$ is a more fundamental quantity.

A considerable amount of rich physics can take place when introducing output optical fields e.g., the driving laser or single-photons. Here we consider the driving laser Hamiltonian $\hat{H}_{\mathrm{L}}$,

$$\frac{\hat{H}_{\mathrm{L}}}{\hbar} = i\sqrt{\kappa_{\mathrm{ex}}}s_{\mathrm{in}}e^{-i\omega_{\mathrm{L}}t}\hat{a}^\dagger + \mathrm{h.c.}, \tag{2.4}$$

we define the external cavity loss rate (refers to the coupling between the optical cavity and the external input field) κ_{ex} and the amplitude of input photon flux s_{in} in the unit of $1/\sqrt{\mathrm{s}}$. For the sake of simplicity, we take the rotation frame with respect to the laser frequency by applying:

$$\hat{U} = \exp(i\omega_{\mathrm{L}}\hat{a}^\dagger\hat{a}t), \tag{2.5}$$

$$\hat{H} \to \hat{U}\hat{H}\hat{U}^\dagger - i\hbar\hat{U}\frac{\partial}{\partial t}\hat{U}^\dagger, \tag{2.6}$$

to the total Hamiltonian $\hat{H} = \hat{H}_0 + \hat{H}_{\mathrm{L}}$. This corresponds to the shift in the optical frequency by $-\omega_{\mathrm{L}}$. The resulting total Hamiltonian becomes

$$\hat{H} = -\Delta\hat{a}^\dagger\hat{a} + \Omega_{\mathrm{m}}\hat{b}^\dagger\hat{b} - g_0\hat{a}^\dagger\hat{a}(\hat{b}^\dagger + \hat{b}) + \sqrt{\kappa_{\mathrm{ex}}}(is_{\mathrm{in}}\hat{a}^\dagger + \mathrm{h.c.}), \tag{2.7}$$

where $\Delta = \omega_{\mathrm{L}} - \omega_{\mathrm{o}}$ is the laser detuning. Then the quantum Langevin equations of motion become,

$$\frac{d}{dt}\hat{a} = \left(i\Delta - \frac{\kappa_0 + \kappa_{\mathrm{ex}}}{2}\right)\hat{a} + ig_0\hat{a}(\hat{b}^\dagger + \hat{b}) + \sqrt{\kappa_{\mathrm{ex}}}s_{\mathrm{in}}, \tag{2.8}$$

$$\frac{d}{dt}\hat{b} = \left(-i\Omega_{\mathrm{m}} - \frac{\Gamma_{\mathrm{m}}}{2}\right)\hat{b} + ig_0\hat{a}^\dagger\hat{a} + \sqrt{\Gamma_{\mathrm{m}}}\hat{f}_{\mathrm{m}}, \tag{2.9}$$

where we define intrinsic decay rate of the optical mode κ_0 and mechanical mode Γ_{m}, and mechanical thermal noise $\hat{f}_{\mathrm{m}}$.

An often-used treatment for these equations of motion is so-called linearization. We split the optical annihilation operator into classical mean amplitude and quantum fluctuation parts:

$$\hat{a} = \bar{\alpha} + \delta\hat{a}, \tag{2.10}$$

where $\bar{\alpha} = \langle\hat{a}\rangle$, and $\delta\hat{a}$ is the quantum fluctuation with zero mean value. The mean number of cavity photons is given as $n_{\mathrm{cav}} = |\bar{\alpha}|^2$. Inserting eq.(2.10) into eq.(2.3) and assuming $|\bar{\alpha}|^2 \gg \langle\delta\hat{a}^2\rangle$, we have

$$\frac{\hat{H}_0}{\hbar} \approx -\Delta\delta\hat{a}^\dagger\delta\hat{a} + \Omega_{\mathrm{m}}\hat{b}^\dagger\hat{b} - g_0(\bar{\alpha}\delta\hat{a}^\dagger + \bar{\alpha}^*\delta\hat{a})(\hat{b}^\dagger + \hat{b}). \tag{2.11}$$

Here we ignore constant terms, $-g_0\delta\hat{a}^\dagger\delta\hat{a}(\hat{b}^\dagger + \hat{b})$ since it is sufficiently smaller than the remaining terms. Also $-g_0|\bar{\alpha}|^2(\hat{b}^\dagger + \hat{b})$ is neglected as it only shifts the mirror position and does not contribute to the dynamics. By rewriting $\delta\hat{a}$ as $\hat{a}$ and assuming $\bar{\alpha}$ to be real without loss of generality, we have

$$\frac{\hat{H}_0}{\hbar} \approx -\Delta\hat{a}^\dagger\hat{a} + \Omega_{\mathrm{m}}\hat{b}^\dagger\hat{b} - (g\hat{a}^\dagger + g^*\hat{a})(\hat{b}^\dagger + \hat{b}), \tag{2.12}$$

where $g = g_0\bar{\alpha} = g_0\sqrt{n_{\mathrm{cav}}}$ is the photon-enhanced optomechanical coupling rate. For the specific case known as sideband-resolved regime $\kappa = \kappa_0 + \kappa_{\mathrm{ex}} \gg \Omega_{\mathrm{m}}$, the interaction term in eq.(2.12) behaves differently with detuning due to the fast- and slow-rotating terms.

(i) At $\Delta = -\Omega_{\mathrm{m}}$, from the Langevin equation of motion eq.(2.8),(2.9) both $\hat{a}$ and $\hat{b}$ time-evolve with phase $e^{-i\Omega_{\mathrm{m}}t}$. By keeping the resonant terms (or in other words, by taking the rotating wave approximation ignoring the terms with $e^{\pm i\Omega_{\mathrm{m}}t}$), the interaction Hamiltonian leads to

$$-(g\hat{a}^\dagger\hat{b} + g^*\hat{a}\hat{b}^\dagger). \tag{2.13}$$

This interaction is called the beam-splitter interaction and is used for state swapping between optical and mechanical modes. The transition rate g is controllable as it scales with the cavity photon number n_{cav}. The optomechanical state swap can also work as the laser cooling of mechanical motion, given that the thermal occupation of optical photons at 200 THz is considerably small ~ 0.006 even at room temperature, and optical modes typically have faster decay rates compared to that of mechanical modes. The first demonstration of ground-state cooling with this method was achieved in an optomechanical crystal system [3]. This interaction is also the key part of an optomechanical memory protocol [11].

(ii) At $\Delta = \Omega_{\mathrm{m}}$ blue-detuning, following the similar process before, the interaction term leads to

$$-(g\hat{a}^{\dagger}\hat{b}^{\dagger} + g^{*}\hat{a}\hat{b}). \tag{2.14}$$

This is called the two-mode squeezing Hamiltonian since it gives rise to the time evolution operator

$$\hat{S}^{g}_{AB}(t) = \exp\left[i\left(g\hat{a}^{\dagger}\hat{b}^{\dagger} + g^{*}\hat{a}\hat{b}\right)t\right], \tag{2.15}$$

which is the same as the generator of the two-mode squeezed states [35]. Here A and B stand for the optical and mechanical modes, respectively. This interaction creates photon-phonon pairs in entangled states as [35]

$$\hat{S}^{g}_{AB}(t)\left|0\right\rangle_{AB} = \operatorname{sech}(|gt|)\sum_{n=0}^{\infty}\left[-e^{i\arg(-igt)}\tanh(|gt|)\right]^{n}\left|n\right\rangle_{A}\left|n\right\rangle_{B}, \tag{2.16}$$

where we only consider the vacuum two-mode squeezed state. The state in eq.(2.16) is clearly seen as a superposition of cavity photons and phonons with the same excitation number (therefore the total excitation is always an even number). However, for some applications, only the first excited state $\left|1\right\rangle_{A}\left|1\right\rangle_{B}$ is necessary and the rest of the superposition states may cause unwanted effects, e.g. low teleportation fidelity [36]. Therefore, a protocol called DLCZ (Duan-Lukin-Cirac-Zoller) [37] is often utilised to selectively create $\left|1\right\rangle_{A}\left|1\right\rangle_{B}$ state. In the protocol, interaction time t is set sufficiently short so that the higher-order entangled states are negligible. And then the non-excited state $\left|0\right\rangle_{A}\left|0\right\rangle_{B}$ is filtered out, thus we get the desired state probabilistically.

As we have mentioned already, in order to obtain those different Hamiltonians separately, we require the resolved-sideband regime $\kappa \ll \Omega_{\mathrm{m}}$. This is the case where the mechanical sidebands $\omega_{\mathrm{o}} \pm \Omega_{\mathrm{m}}$ exist outside the optical lineshape. In such a situation, we can selectively drive one of the sidebands because the other sideband is barely driven. While non-resolved-sideband regime, both the red- and blue-detuned Hamiltonians occur simultaneously.

Within the sideband-resolved regime, the red- and blue-detuned Hamiltonian stated above in eq. (2.13) and eq. (2.14) can be selectively driven, since only one of the mechanical sideband $\omega_{\mathrm{o}} \pm \Omega_{\mathrm{m}}$ exists within the optical lineshape. This is not the case for a non-sideband-resolved regime where both sidebands exist within the lineshape and thus both red- and blue-detuned Hamiltonian occur simultaneously.

Chapter 3

Optomechanical Crystals

Optomechanical crystal [19] is one of the most actively studied platforms in the field of cavity optomechanics. The basic idea is to design a periodic pattern that simultaneously opens bandgaps for optical and mechanical modes (this is possible as both follow wave equations). Since those devices are essentially photonic crystals as well, they can be fabricated with the same technique as is used for nanophotonics devices. It can achieve relatively high mechanical frequencies (typically $\Omega_\mathrm{m}/2\pi = 1 \sim 10$ GHz), and the coupling strength ($g_0/2\pi = 10^2 \sim 10^3$ kHz). Therefore, it is considered a strong tool for fast photon-phonon conversion and/or an interface between flying photons and superconducting qubits through GHz mechanical modes.

This chapter provides the background and basic knowledge of optomechanical crystals, one of the optomechanical platforms. We explain the principle of the optomechanical coupling mechanism, i.e. the moving boundary and photoelastic contributions, and their calculation method. Advantages and disadvantages of different materials, including diamond, silicon and some III-V semiconductors, are described. Recent studies on different structural designs are also shown.

3.1 Coupling Principles

One of the most crucial parts of the OMC design is how well we confine those modes so that they have strong mode overlap since the optomechanical coupling strength depends on the product of the electric and mechanical field (displacement or strain). Understanding the coupling principle will help us

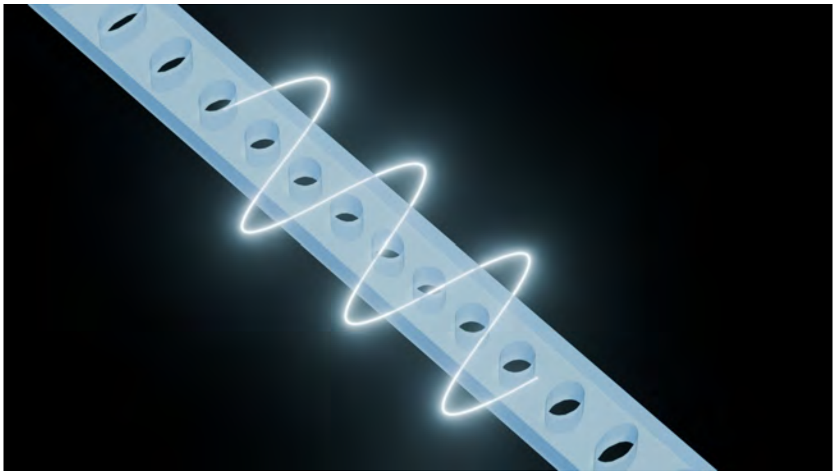

Figure 3.1: Schematic image of a 1D nanobeam optomechanical crystal.

to come up with better structures. Here, we explain the origins of the optomechanical coupling, namely the moving boundary (MB) and photoelastic (PE) contributions in the following.

3.1.1 Moving Boundary Contribution

The optomechanical coupling derives from an effect that the geometry deformation of the photonic crystal shifts its optical resonance. This is because the displacement changes the local dielectric tensor $\boldsymbol{\varepsilon}(\mathbf{r})$ at position $\mathbf{r}$. From the perturbation theory for the Maxwell equations with the shifted boundary of material [38], the frequency shift (therefore the coupling strength g_0) can be calculated within the first order of perturbation,

$$g_0 = \frac{d\omega}{d\bar{\alpha}} = -\frac{\omega_\mathrm{o}}{2} \frac{\langle \mathbf{E} | \frac{d\boldsymbol{\varepsilon}(\mathbf{r})}{d\bar{\alpha}} | \mathbf{E} \rangle}{\langle \mathbf{E} | \boldsymbol{\varepsilon}(\mathbf{r}) | \mathbf{E} \rangle}, \tag{3.1}$$

where we define the unperturbed optical resonance frequency ω_o and electric field $|\mathbf{E}\rangle$, the generalized displacement amplitude $\bar{\alpha}$. Note that the denominator of eq.(3.1) is simply the energy density of the electric field. It is sometimes more useful by denoting with $\bar{\alpha}$ rather than the actual displacement vector $\boldsymbol{u}(\mathbf{r})$, shown in Fig. 3.2, as it reduces the problem from complex 3D vibrational mode to a canonical 1D harmonic oscillator with an effective

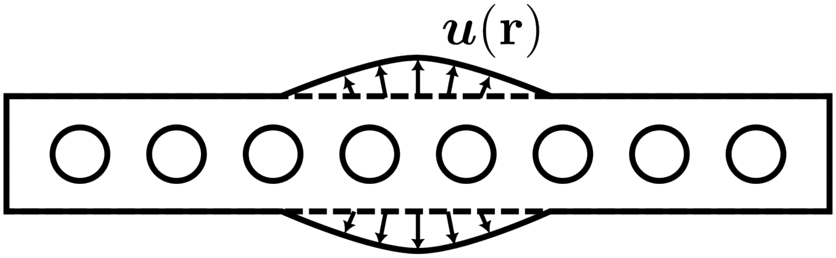

Figure 3.2: Schematic image of the mechanical displacement $\boldsymbol{u}(\mathbf{r})$ in a 1D OMC.

mass of m_{eff}. Here, the conversions are given as [39]

$$\bar{\alpha} = \max(|\boldsymbol{u}(\mathbf{r})|), \tag{3.2}$$

$$m_{\text{eff}} = \frac{\int \rho(\mathbf{r})|\boldsymbol{u}(\mathbf{r})|^2 dV}{\bar{\alpha}^2}, \tag{3.3}$$

where $\rho(\mathbf{r})$ is a local mass density of the device. For the MB contribution to optomechanical coupling g_0^{mb} is then obtained as [38, 40],

$$g_0^{\text{mb}} = -\frac{\omega_{\text{o}}}{2} \frac{\int (\boldsymbol{Q} \cdot \hat{\mathbf{n}}) \left(\Delta\boldsymbol{\varepsilon} \mathbf{E}_{\parallel}^2 - \Delta\boldsymbol{\varepsilon}^{-1} \mathbf{D}_{\perp}^2 \right) dS}{\langle \mathbf{E} | \, \boldsymbol{\varepsilon}(\mathbf{r}) \, | \mathbf{E} \rangle}, \tag{3.4}$$

where we define the normalized displacement vector $\boldsymbol{Q} = \boldsymbol{u}(\mathbf{r})/\bar{\alpha}$, the unit vector normal to the surface $\hat{\mathbf{n}}(\mathbf{r})$, tangential (normal) component of electric (electric displacement) field at the surface $\mathbf{E}$ ($\mathbf{D}$), $\Delta\boldsymbol{\varepsilon} = \boldsymbol{\varepsilon}_{\text{medium}} - \boldsymbol{\varepsilon}_{\text{air}}$, and $\Delta\boldsymbol{\varepsilon}^{-1} = \boldsymbol{\varepsilon}_{\text{medium}}^{-1} - \boldsymbol{\varepsilon}_{\text{air}}^{-1}$. It should be noted that eq.(3.4) depends on the surface integral over the medium-air boundary. These naively result in the orientation of device design which is that the more the surface is the stronger the g_0^{MB} becomes. Recently proposed so-called "C" shape design in 2D OMC [12] is based on this guideline to enhance the MB contribution.

3.1.2 Photoelastic Contribution

The other contribution derives from the photoelastic effect where the strain of the medium changes the refractive index. A component of the strain tensor $\boldsymbol{S}$ is given as [41]:

$$S_{ij} = \frac{1}{2} \left(\frac{\partial u_i}{\partial i} + \frac{\partial u_j}{\partial j} \right), \text{ for } i, j = x, y, z. \tag{3.5}$$

As $S_{ij} = S_{ji}$, only 6 of the 9 matrix components of $\boldsymbol{S}$ are independent. Therefore we can convert the 3×3 matrix to a 6×1 vector

$$\boldsymbol{S} \rightarrow \begin{bmatrix} S_1 \\ S_2 \\ S_3 \\ S_4 \\ S_5 \\ S_6 \end{bmatrix} := \begin{bmatrix} S_{xx} \\ S_{yy} \\ S_{zz} \\ 2S_{yz} \\ 2S_{zx} \\ 2S_{xy} \end{bmatrix}. \tag{3.6}$$

Additionally, we define the relative dielectric tensor in 3×3 matrix $\boldsymbol{\varepsilon}_r(\mathbf{r})$ as

$$\mathbf{E} = \frac{1}{\varepsilon_0} \left(\boldsymbol{\varepsilon}_r\right)^{-1} \mathbf{D}, \tag{3.7}$$

and the relative dielectric impermeability tensor [41] as

$$\boldsymbol{B} := \left(\boldsymbol{\varepsilon}_r\right)^{-1} = \begin{bmatrix} B_{11} & B_{12} & B_{13} \\ B_{21} & B_{22} & B_{23} \\ B_{31} & B_{32} & B_{33} \end{bmatrix}. \tag{3.8}$$

For optically isotropic materials, $\boldsymbol{\varepsilon}_r$ and thus $\boldsymbol{B}$ is diagonal (off-diagonal components are zero). Here we use the abbreviation notation to express the relative permeability tensor in 6×1 similar to the strain tensor,

$$\boldsymbol{B} \rightarrow \begin{bmatrix} B_1 \\ B_2 \\ B_3 \\ B_4 \\ B_5 \\ B_6 \end{bmatrix} := \begin{bmatrix} B_{11} \\ B_{22} \\ B_{33} \\ B_{23} \\ B_{13} \\ B_{12} \end{bmatrix}. \tag{3.9}$$

The shift in $\boldsymbol{B}$ due to the strain is given as [41]

$$\Delta \boldsymbol{B} = \boldsymbol{p} \boldsymbol{S}, \tag{3.10}$$

where $\boldsymbol{p}$ is the photoelastic tensor of the material. For materials with crystallographic point groups of $\bar{4}$3m, 432 and m3m of the cubic crystal system, this becomes [42],

$$\boldsymbol{p} = \begin{bmatrix} p_{11} & p_{12} & p_{12} & 0 & 0 & 0 \\ p_{12} & p_{11} & p_{12} & 0 & 0 & 0 \\ p_{12} & p_{12} & p_{11} & 0 & 0 & 0 \\ 0 & 0 & 0 & p_{44} & 0 & 0 \\ 0 & 0 & 0 & 0 & p_{44} & 0 \\ 0 & 0 & 0 & 0 & 0 & p_{44} \end{bmatrix}. \tag{3.11}$$

Note that $p_{44} = (p_{11} - p_{12})/2$ for isotropic materials, and $p_{11} = p_{12}$, $p_{44} = 0$ for liquid. From eq.(3.10) and (3.11) we have

$$\begin{aligned} \Delta B_1 &= p_{11}S_{xx} + p_{12}(S_{yy} + S_{zz}), \\ \Delta B_2 &= p_{11}S_{yy} + p_{12}(S_{zz} + S_{xx}), \\ \Delta B_3 &= p_{11}S_{zz} + p_{12}(S_{xx} + S_{yy}), \\ \Delta B_4 &= 2p_{44}S_{yz}, \\ \Delta B_5 &= 2p_{44}S_{zx}, \\ \Delta B_6 &= 2p_{44}S_{xy}. \end{aligned} \tag{3.12}$$

Now we come back to the 6 × 6 expression for $\boldsymbol{B}$. The shift in the inverse of the relative permittivity is

$$\boldsymbol{\varepsilon}_r + \Delta\boldsymbol{\varepsilon}_r = (\boldsymbol{B} + \Delta\boldsymbol{B})^{-1}. \tag{3.13}$$

We the shift is small that is, $|\Delta B_i|$ is much smaller than the diagonal components of $\boldsymbol{B}$ (note here again that the unperturbed $\boldsymbol{B}$ and $\boldsymbol{\varepsilon}_r$ are diagonal matrices). Then we have

$$\begin{aligned} \boldsymbol{\varepsilon}_r + \Delta\boldsymbol{\varepsilon}_r &= (\boldsymbol{B} + \Delta\boldsymbol{B})^{-1} \\ &= \boldsymbol{B}^{-1}(\mathbf{1} + \Delta\boldsymbol{B}\boldsymbol{B}^{-1})^{-1} \\ &\simeq \boldsymbol{B}^{-1}(\mathbf{1} - \Delta\boldsymbol{B}\boldsymbol{B}^{-1}) \\ &= \boldsymbol{B}^{-1} - \Delta\boldsymbol{B}\boldsymbol{B}^{-2} \end{aligned}, \tag{3.14}$$

therefore

$$\Delta\boldsymbol{\varepsilon}_r = -\Delta\boldsymbol{B}\boldsymbol{B}^{-2}. \tag{3.15}$$

In eq.(3.14), we used $(1+x)^{-1} \simeq 1 - x$ for $|x| \ll 1$. We consider optically isotropic material,

$$\boldsymbol{B} = \begin{bmatrix} B_{11} & B_{12} & B_{13} \\ B_{21} & B_{22} & B_{23} \\ B_{31} & B_{32} & B_{33} \end{bmatrix} = \frac{1}{n^2} \begin{bmatrix} 1 & 0 & 0 \\ 0 & 1 & 0 \\ 0 & 0 & 1 \end{bmatrix}, \tag{3.16}$$

where n is the refractive index of the material. Then we have

$$\Delta \boldsymbol{\varepsilon}_r = -\Delta \boldsymbol{B} \boldsymbol{B}^{-2} = -n^4 \Delta \boldsymbol{B} \tag{3.17}$$

From eq.(3.12),(3.17) and assume $\varepsilon_0 \Delta \boldsymbol{\varepsilon}_r \simeq d\boldsymbol{\varepsilon}/d\bar{\alpha}$, we have the photoelastic contribution to the vacuum coupling rate

$$g_0^{\mathrm{pe}} = -\frac{\omega_{\mathrm{o}}}{2} \frac{\langle \mathbf{E} | \frac{d\boldsymbol{\varepsilon}(\mathbf{r})}{d\bar{\alpha}} | \mathbf{E} \rangle}{\langle \mathbf{E} | \boldsymbol{\varepsilon}(\mathbf{r}) | \mathbf{E} \rangle}, \tag{3.18}$$

where

$$\begin{aligned}
&\langle \mathbf{E} | \frac{d\boldsymbol{\varepsilon}(\mathbf{r})}{d\bar{\alpha}} | \mathbf{E} \rangle && (3.19) \\
&\simeq -\varepsilon_0 n^4 \langle \mathbf{E} | \Delta \boldsymbol{B} | \mathbf{E} \rangle, && (3.20) \\
&= -\varepsilon_0 n^4 \int (E_x, E_y, E_z) \\
&\times \begin{pmatrix} p_{11} S_{xx} + p_{12}(S_{yy} + S_{zz}) & 2p_{44} S_{xy} & 2p_{44} S_{zx} \\ 2p_{44} S_{xy} & p_{11} S_{yy} + p_{12}(S_{zz} + S_{xx}) & 2p_{44} S_{yz} \\ 2p_{44} S_{zx} & 2p_{44} S_{yz} & p_{11} S_{zz} + p_{12}(S_{xx} + S_{yy}) \end{pmatrix} \\
&\times \begin{pmatrix} E_x^* \\ E_y^* \\ E_z^* \end{pmatrix} dV. \\
& && (3.21)
\end{aligned}$$

Therefore, the total vacuum optomechanical coupling rate g_0^{tot} reads,

$$g_0^{\mathrm{tot}} = g_0^{\mathrm{mb}} + g_0^{\mathrm{pe}}. \tag{3.22}$$

Note that each contribution, therefore the total coupling rate too, can be negative but only its absolute value plays a role in many cases. Especially in the linearised case detailed in chapter2, the effective coupling rate $g = g_0 \alpha$ depends on the phase of the driving laser as well.

3.2 Material Choice

3.2.1 Silicon

As the base technology for OMC device fabrications is quite similar to that of conventional nanophotonics such as photonic crystals, there are quite diverse material options according to the purposes. The first OMC has been realised with silicon platform [19], which is still one of the most commonly used materials in the field of OMC. One can precisely make the OMC structure with a well-established and sophisticated fabrication process. It is advantageous in terms of both optical and mechanical properties. Also, silicon is currently at the very heart of the complementary metal–oxide–semiconductor (CMOS) technology which makes silicon OMC strongly advantageous for industrial applications.

Its refractive index $n = 3.48$ at 1550 nm is one of the highest among commonly used materials. Also, silicon is a relatively hard material (Young's modulus of 130-188 GPa depending on its crystalline axis [43]) thanks to the diamond cubic structure, and the mechanical frequency tends to be high (typically $\sim$ 5 GHz for 1D structure [44] and $\sim$ 10 GHz for 2D [12, 13]) compared to that of other materials e.g., III-V semiconductors.

3.2.2 Diamond

Diamonds are well known as the hardest natural material found on the earth. Therefore, OMCs made of the diamond show even higher mechanical frequencies than silicon, as high as 9.5 GHz for 1D has been realised [45] for 1D nanobeam. Additionally, diamond is a really good thermal conductor; the pure type-IIa natural diamond has a thermal conductance of $\sim$ 20 W/cmK [46] at 300 K. Remarkably, this value is even higher than that of silver $\sim$4 W/cmK, the most thermally conductive metal. Therefore, it is assumed that heat can dissipate through diamonds quickly thus reducing the thermal noise. Moreover, current developments in colour centres in diamond [47], have attained even more attention together with the abovementioned advantages. The defects in a diamond crystal, usually nitrogen, silicon or germanium atomic defects, have spin states that are well decoupled from the almost spinless carbon lattice, leading to a long spin coherence time. A nitrogen-vacancy (NV), silicon-vacancy (SiV), and germanium-vacancy (GeV) centres each has achieved spin coherence time T_2 of >1 s [48],

>10 ms [49], and >100 ns [50], respectively. For that, many efforts have tried to couple the mechanics to the colour centre for advanced quantum communication or processing [51–55]. However, the refractive index of a diamond is not among the highest (typically ∼2.4 for 1550 nm), which may result in a relatively small vacuum optomechanical coupling rate. Indeed, a reported coupling rate $g_0/2\pi$ ∼220 kHz in a 1D diamond OMC [45] is a factor of 4-5 lower than that typically achievable in 1D silicon OMCs [6, 44].

3.2.3 Gallium Arsenide

Another promising material is gallium arsenide (GaAs). This III-V semiconductor has quite a large refractive index n=3.37 at 1550 nm, just below that of silicon, enabling a large $g_0/2\pi \sim 1$ MHz [56, 57] in a nanobeam OMC making it comparable to that of silicon platforms. The crystal is not as stiff as diamond or silicon, resulting in relatively low mechanical frequencies (∼ 2.4 GHz fo 1D OMC). One of the particularly attractive material properties of GaAs is their sufficiently high piezoelectricity. That enables us to access the mechanical motion electrically and to achieve optics-to-microwave conversion [57, 58]. A possible direction of development with this material will be to combine it with the quantum dots (QDs) [59]. GaAs is one of the most common platforms for the QD-based single-photon source [60] which is now considered a key component for quantum networking.

3.2.4 Gallium Phosphide

Gallium phosphide is also a III-V semiconductor and has recently been studied intensely thanks to some advantageous features favorable to quantum optomechanics; (i) a sufficiently large refractive index $n = 3.05$ at 1550 nm beneficial to high optical quality factor and vacuum optomechanical coupling, (ii) a large electronic bandgap 2.26 eV which is larger than the two-photon energy at 1550 nm (1.6 eV) suppressing the two-photon-absorption-induced thermalization, (iii) it is a piezo material that can directly couple the mechanical signal to electrical signals [16,17]. Although the material has already been employed in microdisk optomechanics [61], it was not until 2019 when the first GaP OMC was reported with 1D structure at room temperature [14] and cryogenic environment [15]. The mechanical frequency of 1D GaP OMC is typically ∼3 GHz [14–17] and reported optomechanical coupling rate $g_0/2\pi$ rages around 200-800 kHz.

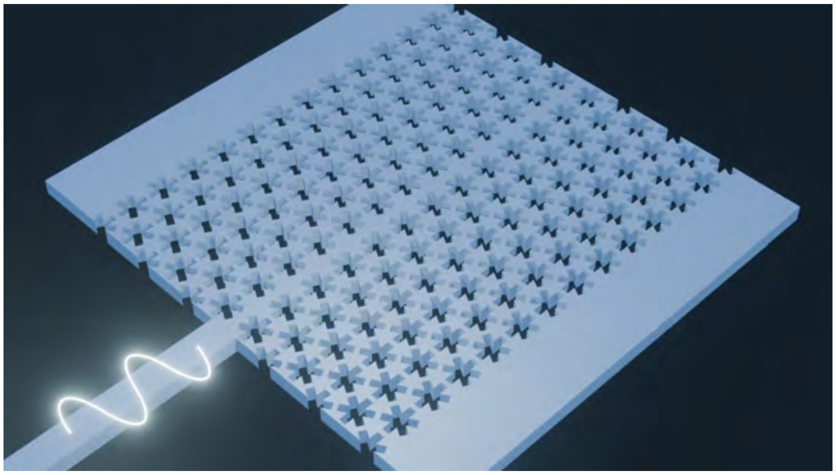

Figure 3.3: Schematic image of a 2D optomechanical crystal with snowflake holes.

3.3 Structural Variations

The first OMC has a 1D nanobeam structure with rectangle holes [19], then soon later an optimized design with ellipse holes has been proposed [40]. For 1D OMCs, the ellipse-based design has now become a more popular structure. In either case, the mechanical mode that couples to the light most strongly is the so-called 'breathing mode' whose in-plane displacement is roughly perpendicular to the nanobeam (most of the displacement is confined around the edge of the nanobeam). Another type of motion e.g., a flexural mode is also often utilized [23, 62]. As well as the single-nanobeam design, there are also dual-nanobeam structures [63], which mainly utilize flexural and out-of-plane motion.

Beyond the 1D structures, 2D design has also been proposed and realised [20, 21]. The basic concept is to design the holes with a complex 'snowflake' shape having more degrees of freedom to engineer both mechanical and optical modes. A schematic is shown in Fig. 3.3. A typical strategy for 2D OMC structural engineering is to (i) design a unit cell so that target mechanical/optical frequencies are placed within the bandgaps, (ii) introduce a line defect to break a symmetry along an axis resulting in 1D confinement, (iii) finally vary the unit cell size to realise 2D confinement. There are some variations regarding the line defect. Originally realised device [21] has a row of removed snowflakes while recently developed devices [12, 13, 64] have C-shaped holes in the middle of the line. The C-shaped holes enable more surface area in the OMC giving rise to more MB contribution to the coupling rate. This is especially beneficial to materials with relatively small photoelastic constants like silicon (note that MB is given by surface integral while PE is by volume integral).

Generally, 2D breathing modes can achieve a factor of 2 times higher mechanical frequency compared to 1Ds [12, 44] making it favourable in terms of quantum optomechanics due to its lower thermal occupation. The dimensional difference in OMC design gives rise to distinct optical/mechanical features. One of the most motivating advantages of 2D designs is higher resilience to laser-absorption-induced heating compared to 1D structures thanks to the higher thermal conductance. Thermal phonons in a 2D OMC can dissipate two-dimensionally and thus are expected to dissipate faster than that of 1D in which phonons dissipate only along the nanobeam. This results in a suppressed temperature increase in the OMC. The laser-absorption-induced thermal phonons in both designs have been measured and compared in silicon devices [12, 13], and the advantage has been strongly supported. However, 2D structures usually have larger mechanical linewidth because the mechanical mode also dissipates faster.

3.4 Overview of the Field

Compared to other optomechanical systems, OMCs place themselves in a unique position due to their high degree of freedom in the structural design and integrity. The variety of the design enables different parameter regimes on both optics and mechanics. The high mechanical frequencies allow them to achieve the ground state relatively easily and to operate in quantum regimes. Indeed, a silicon OMC was the first optomechanical device that achieved mechanical ground state by laser cooling [3].

OMCs are also considered one of the promising platforms bridging different quantum systems to the telecom photons e.g., microwave photons of the superconducting circuit. On top of that, recent studies have made use of the piezoelectric feature of some materials such as GaP [17]. This allows the mechanical oscillation to be converted into voltage directly through the piezoelectric effect. This can be one of the electric-mechanical couplings which is a key to achieving telecom-microwave transduction. The high integrity of OMCs has enabled piezoelectric-based transduction even for silicon platforms that are inherently not piezoelectric. This is done by depositing another piezo material such as aluminium nitride on top of a silicon device [18]. What is especially unique to OMCs is that those conversions can be done on one integrated chip that has all the necessary components [13, 17, 18]. This is useful for scaling up the devices for quantum communication. Those high degrees of freedom will attract even more amount of attention.

While the promising feature for quantum communication, OMCs tend to have slightly limited mechanical coherence time. This is due to its high mechanical frequency which acts as a double-edged sword. Recently, 130 μs of mechanical coherence time has been reported on silicon OMC [44], while 140 ms has been reported on the soft-clamped membrane [65]. This may imply that such devices are better suited for communications rather than sensing.

Chapter 4

2D Snowflake Optomechanical Crystal

This chapter shows the details of our 2D GaP OMC design. We begin with a unit cell snowflake design in a hexagonal pattern. The unit cell simulation of both mechanical and optical modes shows band gaps at desired frequency ranges. Next, we introduce the line defect which is the removal of a row of snowflakes forming a waveguide-like confinement. Finally, we arrive at the 2D defect design which is based on a gradient change of snowflake hole size and achieves gentle confinement. We show simulated mode profiles and the vacuum optomechanical coupling rates.

Numerical simulations for the fibre-waveguide couplings are also shown. The simulated travelling electromagnetic field reveals how the light mode exists in the waveguide and becomes hybridized with the fibre.

4.1 Unit Cell Design

We employ the snowflake holes [20, 21] whose geometry is shown in Fig. 4.1(a). Our design comprises 3 rotated rectangles with width w which form a 6-folded symmetric design. To make the geometry feasible, we smooth the corners by adding additional circles and fillets. We add circles with diameter w at the outer spike of the snowflake and fillets with diameter r at the inner corners. For the band diagram, we simulate the mechanical and optical modes by sweeping the wavenumber. The sweep is carried out along the edge of the yellow-highlighted area in Fig . 4.1(b). The hexagon is the

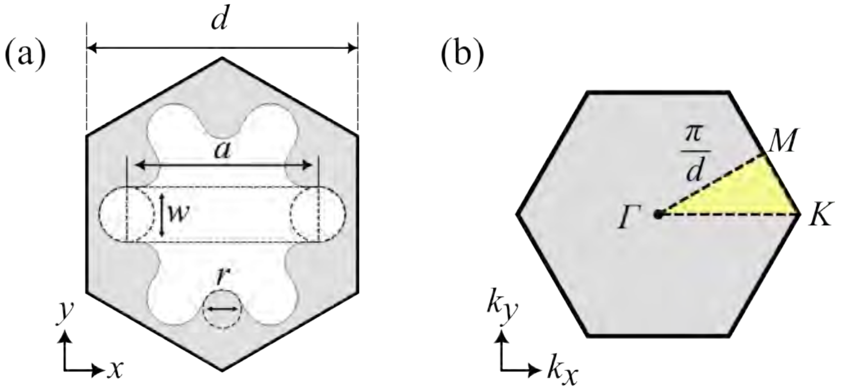

Figure 4.1: (a) Geography of a unit cell. (b) The 1st Brillouin zone of the reciprocal space.

1st Brillouin zone of the reciprocal space where $\Gamma - M$ distance is π/d. We use the finite element solver COMSOL [66] in which the Floquet periodicity condition is applied on the boundaries in Fig. 4.1(a).

We set the geometrical parameters (a, w, r, d) = (370, 120, 80, 577) nm and the thickness of 260 nm. The r-parameter, the fillet diameter of an inner corner of the snowflake, requires special consideration as the limit of large fillet $r \gg d$ the snowflake shape eventually coincides with a hexagon, and loses its degree of freedom. The minimum value of the fillet diameter r is fabrication dependent, namely, the precision of the electron beam writer, etching process, and all the following processes must be considered. For our fabrication technique specifically, $r = 80$ nm is quite feasible.

For a cubic crystal lattice, e.g. GaP or GaAs, the mechanical property is determined by an anisotropic elastic tensor

$$\begin{pmatrix} C_{11} & C_{12} & C_{12} & 0 & 0 & 0 \\ C_{12} & C_{11} & C_{12} & 0 & 0 & 0 \\ C_{12} & C_{12} & C_{11} & 0 & 0 & 0 \\ 0 & 0 & 0 & C_{44} & 0 & 0 \\ 0 & 0 & 0 & 0 & C_{44} & 0 \\ 0 & 0 & 0 & 0 & 0 & C_{44} \end{pmatrix}, \tag{4.1}$$

where the elastic tensor components are (C_{11}, C_{12}, C_{44}) = (140.5, 62.0, 70.3) GPa for GaP [67]. Fig. 4.2(a) is the simulated band diagram of the mechanical modes. The mechanical modes with yz-symmetry at the Γ point

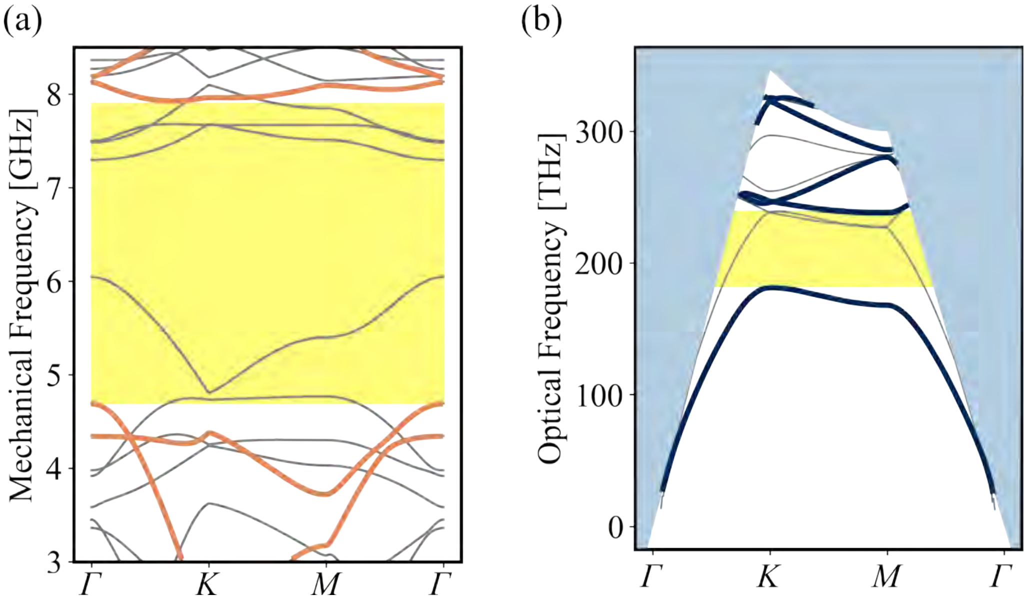

Figure 4.2: (a) Mechanical band structure of the unit cell shown in Fig. 4.1. The parameters of the design are (a, w, r, d) = (370, 120, 80, 577) nm and the thickness is set to 260 nm. The relevant bands are emphasized with orange lines. (b) Optical band diagram of the unit cell. yz-symmetric modes are indicated by the blue curves. The area beyond the light cone is filled with light blue. For both band diagrams, the band gaps of the relevant modes are shaded in yellow.

are indicated by orange lines in Fig. 4.2(a), which is a prerequisite for the mechanical mode to possess a sufficient optomechanical coupling rate to a TE optical mode. A large mechanical bandgap of relevant modes > 3 GHz is achieved around the frequency of ~ 6.5 GHz, shaded in yellow, together with a full bandgap > 1 GHz. It well separates confined mechanical modes from the continuous leaky modes. Fig. 4.2(b) is the simulated optical band structure. Relevant modes with yz-symmetric electromagnetic field are shown in blue. The area filled by yellow is the pseudo bandgap around the telecom C-band between 181-238 THz. Note that this is not a complete bandgap which may result in a leaky optical mode although the detail is not studied

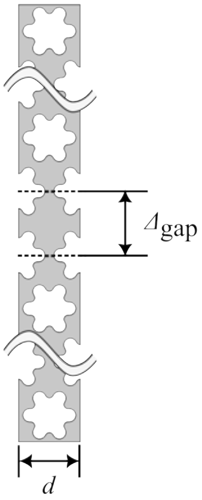

Figure 4.3: Schematic of the 1-dimensional unit structure with the line defect. Δ_{gap} determines the separation gap distance.

in this thesis. The area filled in blue is beyond the light cone

$$\text{Optical frequency} > \frac{ck_0}{2\pi}, \tag{4.2}$$

where c is the speed of light in a vacuum and k_0 is the absolute value of the wave vector in a vacuum. Any optical mode beyond the cone must have a refractive index below unity $n < 1$, which is ignored in our analysis.

4.2 Line Defect

As a first step to realise 2D confinement, we need to break the y-symmetry. For that, we remove a row of snowflakes along the x-axis and modify the gap distance Δ_{gap} between the two regions. This creates a line defect which confines those modes along the x-axis resulting in a waveguide-like mode. This is an often used method for photonic crystal waveguides through which light propagates with very small loss or slowed down [68]. For our full device, the line defect eventually end-couples to the travelling waveguide for optical access. The line defect design enables the optical mode to spread along the x-axis (namely along the line defect) whose distribution tail can reach

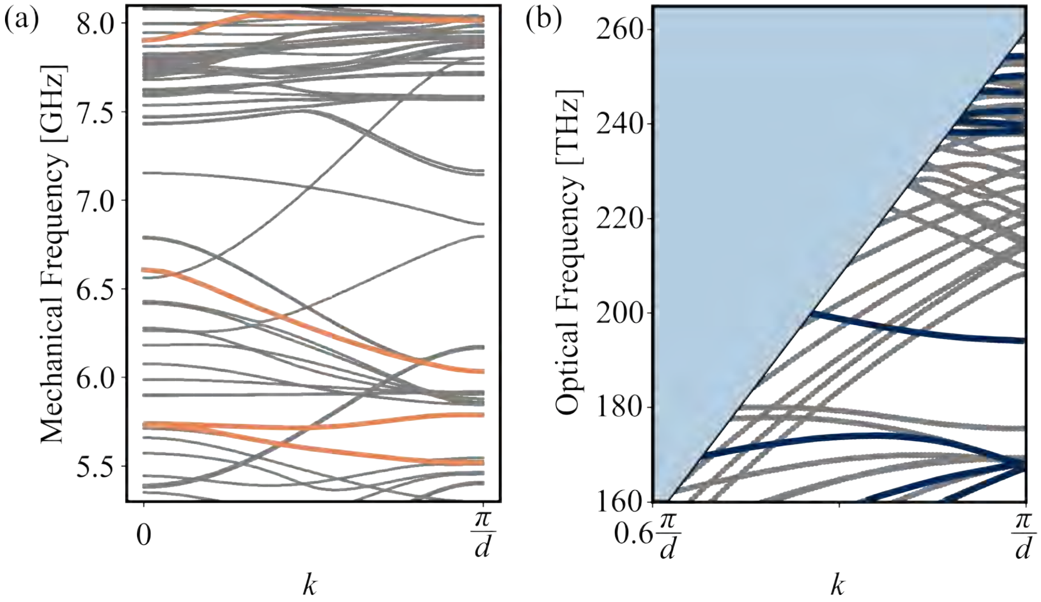

Figure 4.4: Band diagrams for the line defect unit cell. (a) Mechanical band diagram. Orange curves are the modes with yz-symmetry. (b) Optical band diagram. The shaded area is above the light cone. Modes with yz-symmetry are indicated by blue curves.

the access waveguide and couples to the travelling modes. For some designs without line defects and perfectly 2D confined modes, one can either place a photonic crystal waveguide by the defect region and make them evanescently couple each other [69, 70], or directly approach it with a coupling fibre from above [71, 72]. The gap size Δ_{gap} not only determines the confinement mode profile, mode volume etc., but also changes optical and mechanical frequencies. Therefore, it is an important parameter to tailor the frequency for the requirement, especially to make the optical frequency around the telecom C-band.

Fig. 4.4 shows the band diagrams of mechanical and optical modes with a line defect for $\Delta_{\text{gap}} = 600$ nm. For both plots, the indicated curves have yz-symmetry and therefore have the potential to achieve sufficient optomechanical coupling for the full structure. The blue-shaded area in the optical diagram is the light cone eq. (4.2). The optical mode at around 200 THz eventually becomes the relevant optical cavity mode when 2D confinement is introduced.

4.3 Full Device Design

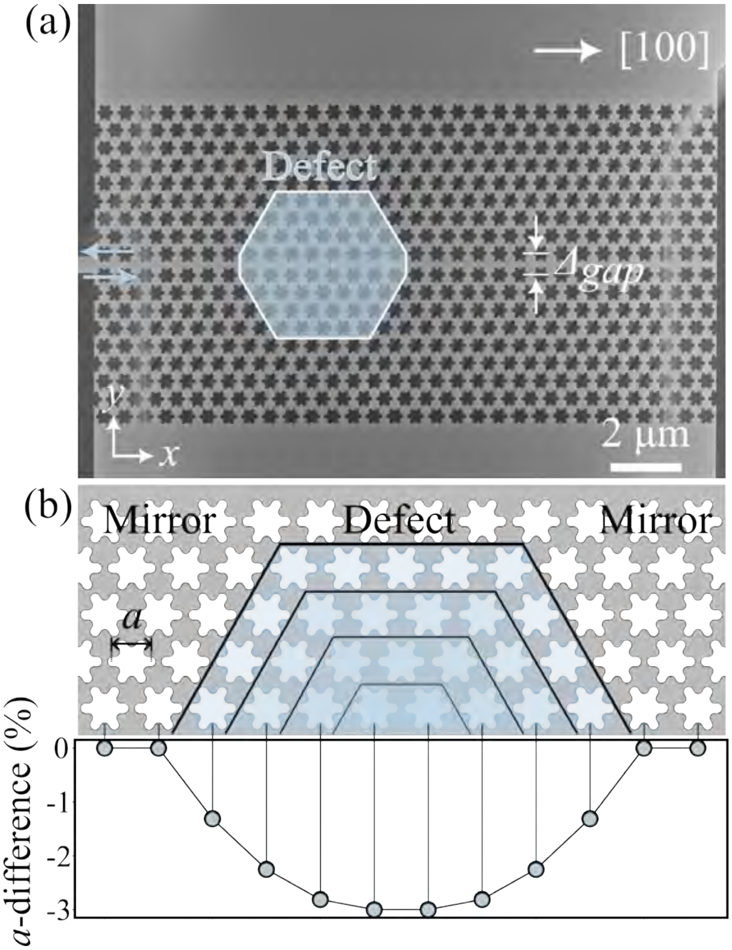

Figure 4.5: (a) SEM image of the whole structure (b) Schematic description of the full structure design. The quadratic variation of the *a*-parameter is shown.

We can now design a full device structure to confine the modes two-dimensionally (rigorously speaking, they are already confined along *z*-axis due to the finite thickness of the slab) to form optical and mechanical cavities for which we need another defect that breaks xy-symmetry. In the context of photonic crystals, some variations in structural engineering have been proposed to realise the defect [69]. One of the most commonly used methods is to gradually change geometrical parameters (e.g., lattice constant, hole size, etc.) around the cavity so that the device confines the optical mode gently. This gentle defect gives rise to a less lossy cavity mode compared to a steep defect. Here we employ the gradual variation in the snowflake size, more specifically the a parameter in Fig. 4.1(a), over a certain area. Fig. 4.5(a) is an SEM image of a fabricated device, where the blue-shaded area indicates the defect region. It spans over 8 snowflakes along the x-axis making it a hexagon-like defect region. The detail of the variation is depicted in Fig. 4.5(b). The a-parameter of the geometry quadratically changes within the defect region with a minimum value of 3% smaller than that of the mirror region. The cavity mode confinement is strongly affected by how much the defect region varies the snowflake size from the mirror region. The larger size difference shifts the mode frequency larger, while it makes the confinement less gentle leading to leaky modes. Additionally, the fabrication precision limits the possible minimum value of a-difference.

Fig. 4.6 is the profiles of absolute mechanical displacement of the three relevant modes. As a prerequisite, those mechanical modes need to have xyz-symmetry so that their parities match that of the TE optical mode of concern. This can be understood by considering eq. (3.4) and eq. (3.19), where the overlap of optical and mechanical modes gives rise to the optomechanical coupling. In the case of an anti-symmetric mechanical mode, one contribution is cancelled by another contribution from the opposite side of the structure.

Fig. 4.7 shows the optical mode profile (E_y) of the TE-like cavity mode in the xy-plane located at the centre of the device thickness. It has eigenfrequency of $\omega_o/2\pi = 192.7$ THz and is symmetric along the yz-axis. An isotropic refractive index $n = 3.05$ is used for this simulation.

For both mechanical and optical simulations, we limit the number of snowflakes to make it computable. We set 8 snowflakes along the y-axis and 17 along the x-axis but some of them are cleaved in half at the edge shown in Fig. 4.7. This is enough number to simulate the actual device considering both modes are well confined within the area simulated. See the appendix A.1.3 for more details.

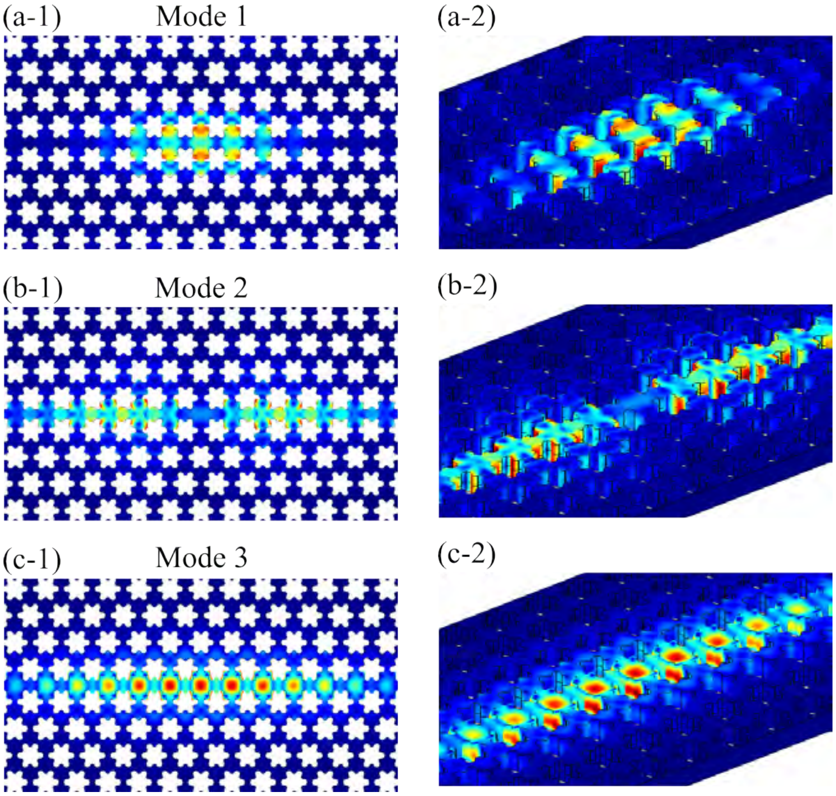

Figure 4.6: (a,b,c) Simulated mechanical displacement of modes labelled 1-3 from top to bottom. They have eigenfrequencies $\Omega_\mathrm{m}/2\pi$ = 5.75, 6.57 and 7.85 GHz respectively.

4.4 Optomechanical Coupling

The vacuum optomechanical coupling rate is calculated with COMSOL by taking the spatial integral of the electromagnetic and mechanical displacement field (see appendix for more details). The actual expressions are eq. (3.4) for the MB and eq. (3.19) for the PE contribution. Fig. 4.8 shows the simulated vacuum optomechanical coupling rates for some mechanical eigenmodes ranging from 5.5 to 8.0 GHz. For the three dominant modes, we find $(g_0, g_0^{\mathrm{MB}}, g_0^{\mathrm{PE}})/2\pi$ = (-718, -305, -414) kHz for mode 1, (-256, -156, -101) kHz for mode 2, and (-983, -755, -228) kHz for mode 3. Note that only the absolute value of the total coupling rate $|g_0|$ is directly measurable in our device and characterisation technique in this thesis. For the mechanical modes to

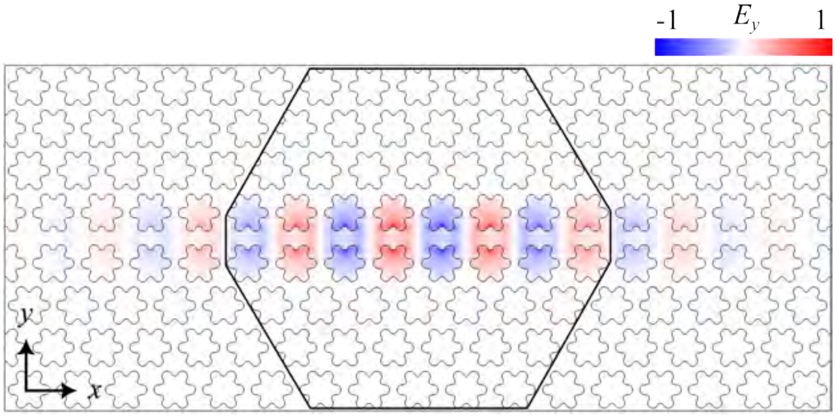

Figure 4.7: Simulated E_y of the TE-like cavity mode. The cavity region is surrounded by the black line.

couple to a TE optical mode, they must not be anti-symmetric along all the xyz-axis, and the modes 1-3 satisfy this condition. The relative sign of the MB and PE contribution can be different depending on the structural design, the mechanical mode profile, and so on.

Our device is designed so that both MB and PE effects contribute comparably strongly to the total coupling rate. This is enabled by the sufficiently strong photoelastic coefficients of GaP (p_{11}, p_{12}, p_{44}) = (-0.23, -0.13, -0.10) [73], which are a factor of 2 larger than that of silicon (p_{11}, p_{12}, p_{44}) = (-0.094, 0.017,-0.051) [74]. Considering each contribution's origin naively, the greater surface area may result in a stronger MB contribution, while more bulk strain may lead to a larger PE contribution. The concept of the C-shape design in silicon devices [12,13] is to increase the g_0^{MB}, while our design is to have both contributions comparably.

4.5 Waveguide and Fiber Coupling

Here we present the details of another important component of the device; the waveguide. It is crucial to be a single-mode waveguide so the relevant mode transmits without loss or unwanted back-reflection. Fig. 4.9 shows the simulated absolute value of electric field $|E|$ of a mode frequency of 193.4 THz in the cross-section of the waveguide. For all the simulations, the thickness of the GaP waveguide is set to 260 nm. In simulations for widths of 600 and 550

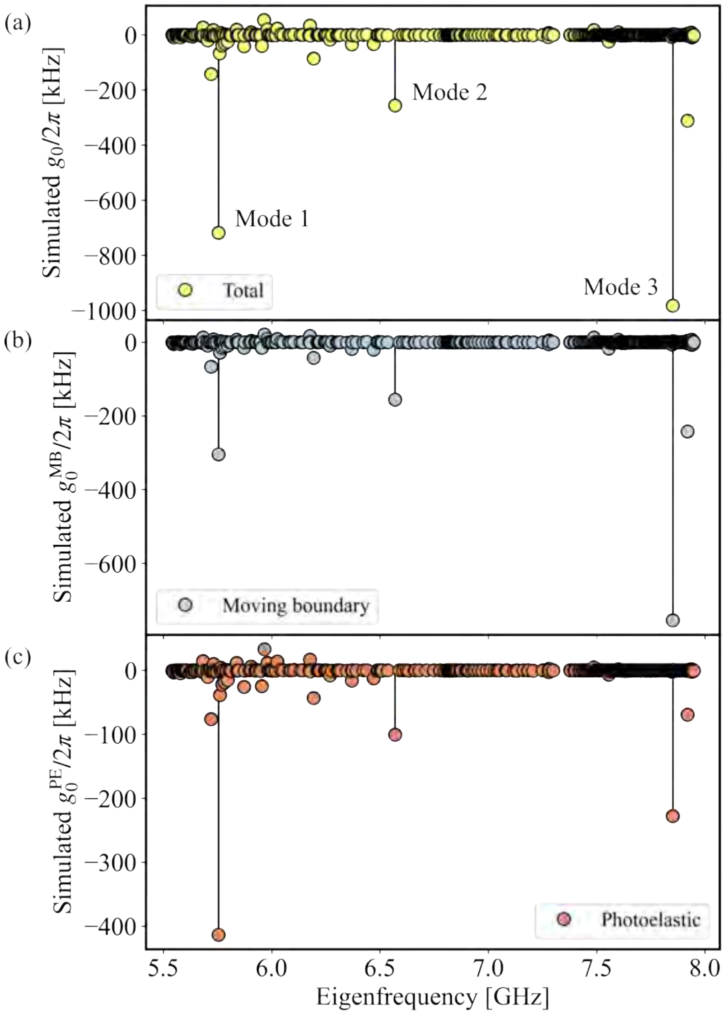

Figure 4.8: Simulated total vacuum coupling rate $g_0/2\pi$ (top), the MB contribution $g_0^{\mathrm{MB}}/2\pi$ (middle), and the PE contribution $g_0^{\mathrm{PE}}/2\pi$ (bottom). The modes of concern are indicated by the lines.

nm, there exists not only the fundamental mode but another irrelevant mode since the imaginary part of the effective mode index n_{eff} is negligible. Since both are TE modes, they can unintentionally couple each other resulting in unexpected back reflection or energy loss. For widths of 500 and 450 nm, the n_{eff} have a non-negligible imaginary part making the irrelevant mode lossy,

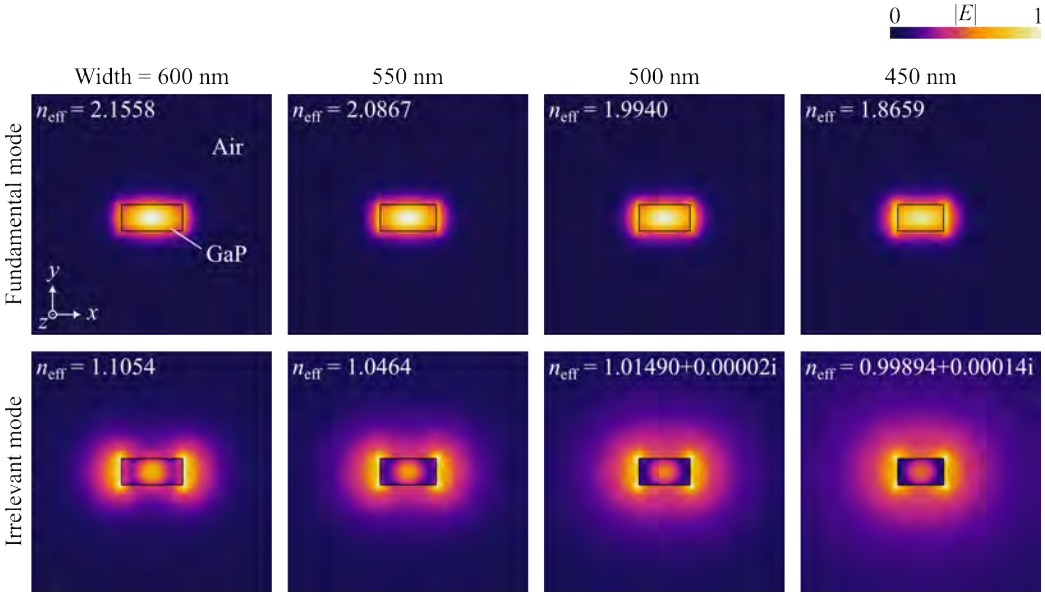

Figure 4.9: Simulated $|E|$ of waveguide cross-section with various widths. The thickness is set to 260 nm.

and thus enabling a single-mode waveguide. We employ 500 nm width for our devices.

We employ the fibre evanescent coupling to the access waveguide [75, 76] expecting its potential for high coupling efficiency (97% has been reported [75]) and for the ability to reduce vibrational noise from the fibre at cryogenic experiments. The principle of the coupling method is shown in Fig. 4.10. Both optical fibre and waveguide are tapered and touched around the tip. The input optical field gradually shifts from the low-loss travelling mode to the lossy evanescent mode through the optical fibre. The fibre evanescent mode is then coupled to that of the waveguide and eventually becomes waveguide travelling mode. It is necessary to precisely position the fibre onto the waveguide to maximise the coupling efficiency. This configuration is expected to reduce the vibrational noise of the fibre as it mechanically touches the device. It is also compatible with the cryogenic packaging of the whole device [77, 78] for more simplified and accessible cryogenic experiments.

We examine how the evanescent couplings occur with optical simulations. Fig. 4.11 shows the simulated $|E|$ with a mode frequency of 193.4 THz in the cross-section with different fibre radii and waveguide widths. The refractive

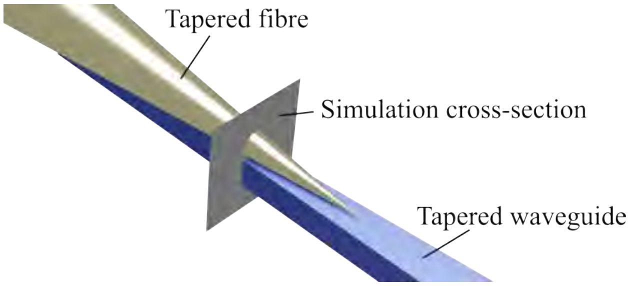

Figure 4.10: Schematic image of the fibre-waveguide coupling configuration. Both fibre and waveguide are tapered forming the hybridized travelling mode.

index of the fibre is set to $n = 1.452$ in the simulation. In the limit of full waveguide width and small fibre radius (width = 500 nm, radius = 200 nm), most of the electric field is confined within the waveguide. This becomes the opposite in the case of a narrow waveguide and large fibre radius (width = 200 nm, radius = 500 nm); the electric field mostly exists in the fibre. However, in other situations where both fibre and waveguide can not confine the mode completely, there is a hybridized mode which interfaces the optical modes between them. The simulation also reveals that, for an effective transfer, the width of the waveguide tip needs to be at least narrower than 200 nm, otherwise the electric energy does not travel between the waveguide and the fibre.

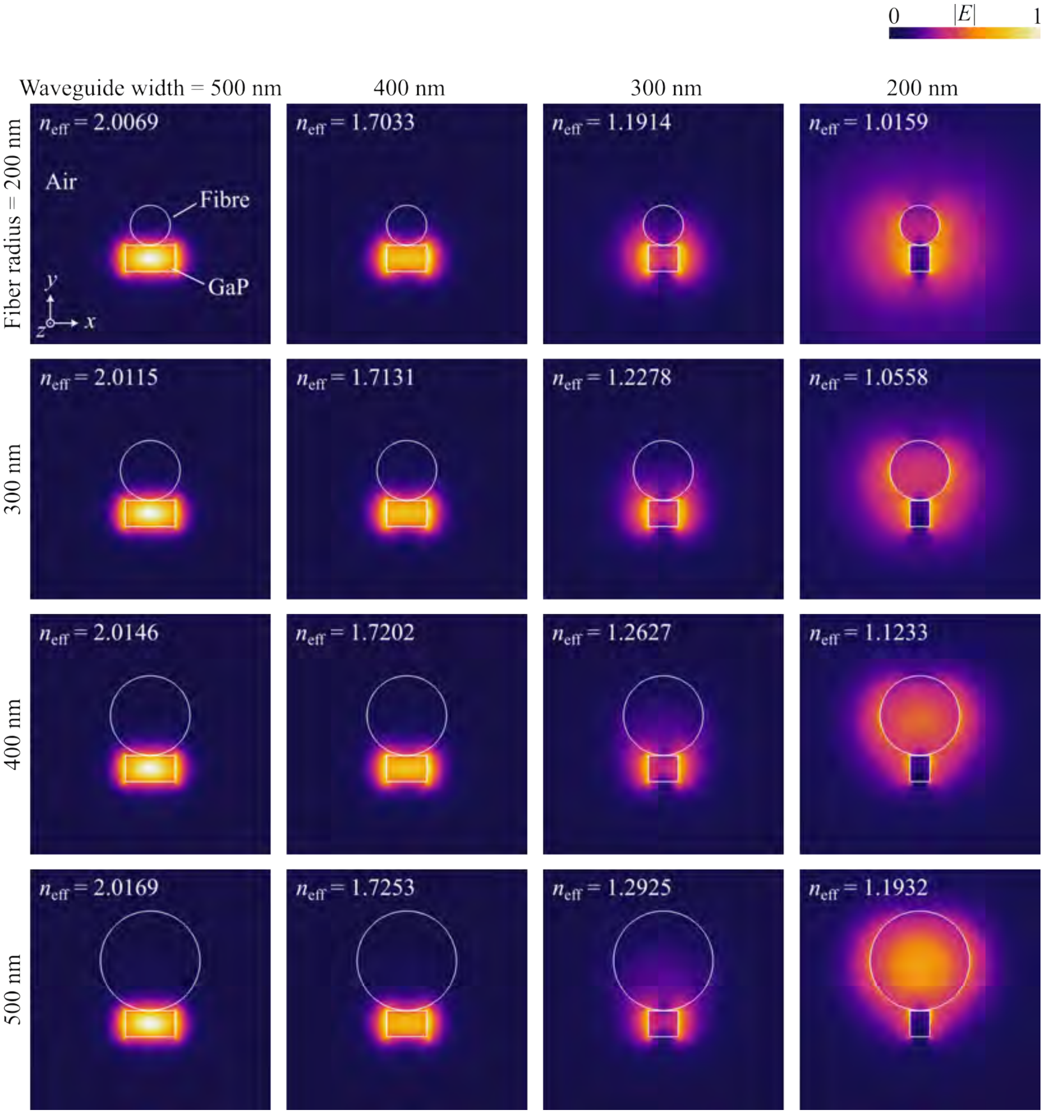

Figure 4.11: Simulated $|E|$ of waveguide-fibre cross-section with various waveguide width and fibre radius. The mode analysis frequency is 193.4 THz.

Chapter 5

SSH Topological Optomechanical Crystal

In this chapter, we provide a different class of OMC design based on the Su–Schrieffer–Heeger (SSH) topological model. The SSH model is one of the one-dimensional topological insulators, and the corresponding mode is topologically protected. We apply this concept to an OMC device expecting robust mechanical and optical modes. Our design comprises a periodical ellipse dimer whose alternating gap distances correspond to the single- and double-bonds in polyacetylene molecules. We design several configurations that connect two topologically different SSH chains to discuss how the edge mode appears.

5.1 Structural Design

The SSH model is a 1-dimensional lattice made of dimers, now classified as a type of 1D topological insulators [79]. It was originally proposed theoretically to explain the electric energy of a long chain of polyacetylene $(CH)_x$ [25], and later experimentally verified [80]. In those molecules, the methylidynes (CH) are bonded together by alternating single- and double-bonds (Fig. 5.1(a)), which forms effective dimers. The chain Fig. 5.1(a) has a degenerated configuration with interchange single- and double-bonds, and they are topologically different. The SSH model for polyacetylene consists of tight-bounded π-electrons which can hop to neighbouring CH sites. The Hamiltonian is

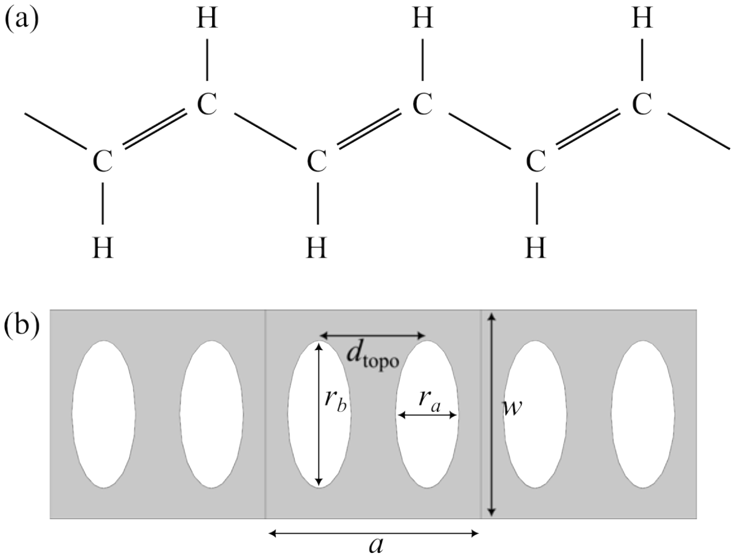

Figure 5.1: (a) Chemical structure of a polyacetylene molecule. (b) Unit cell design of an SSH topological optomechanical crystal.

given as [25, 80]

$$H = -(t+\Delta_{\text{hop}})\sum_{n\in\text{odd}}\left(c^{\dagger}_{n+1}c_n + \text{ h.c. }\right) - (t-\Delta_{\text{hop}})\sum_{n\in\text{even}}\left(c^{\dagger}_{n+1}c_n + \text{ h.c. }\right) \tag{5.1}$$

, where c_n is the fermionic annihilation operator of π-electron at the n-th site. t is the average hopping energy and $2\Delta_{\text{hop}}$ is the hopping imbalance between the single- and double-bonds. By connecting those chains results in the topological soliton which is considered a stable state.

Inspired by the electrons in polyacetylene, researchers have developed SSH-based photonic platforms [81, 82] for more stable and efficient light propagation. Here, we propose an SSH-based optomechanical platform where the optical and mechanical modes are expected to be topologically protected and robust against disorders such as fabrication errors or dust particles.

Our unit cell design Fig. 5.1(b) resembles a polyacetylene molecule, where methylidynes (CHs) are replaced by ellipse holes on a nanobeam and the chemical bonds are interpreted as the gap between ellipses. In the figure, d_{topo} corresponds to the double-bond and $a - d_{\text{topo}}$ to the single-bond. Note

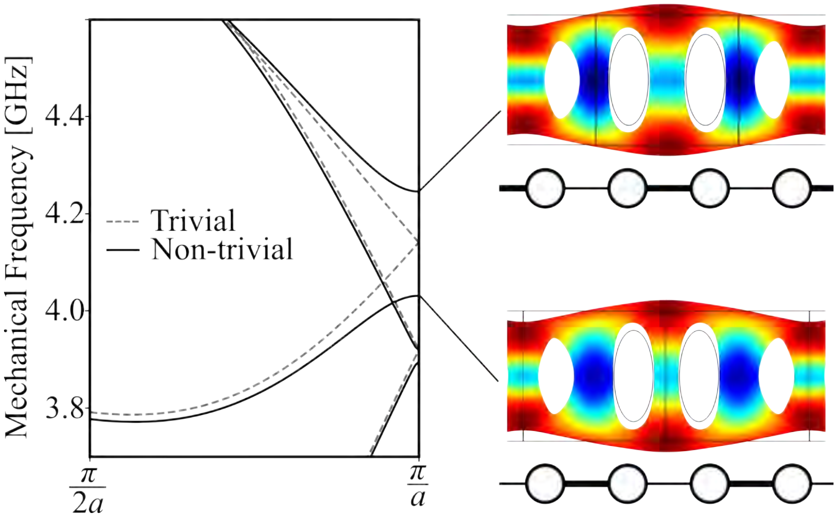

Figure 5.2: Mechanical band diagram of the trivial and non-trivial structure. $d_{\mathrm{topo}} = a/2$ for trivia and d_{topo}=295 nm for non-trivial. The insets show the mechanical mode profile for the upper and lower modes of the non-trivial case. The thick (thin) lines in the schematic images represent large (small) gap distances between ellipses.

that if $d_{\mathrm{topo}} = a/2$, the structure is simply a periodical ellipse with a lattice constant of $a/2$. A basic idea to realise topologically protected modes is to connect two chains, namely a chain with $d_{\mathrm{topo}} > a$ and $d_{\mathrm{topo}} < a$ jus like the soliton in a polyacetylene molecule.

5.2 Numerical Simulation

First, we simulate the band structures of the unit cell. We choose GaP for the nanobeam expecting the suppressed laser heating at the telecom C-band. As the geometrical parameters, we set $(a, r_a, r_b, w) = (550, 150, 350, 500)$ nm and a thickness of 260 nm, also assuming the [100] crystalline axis is parallel to the nanobeam. Fig. 5.2 shows the band diagram of the mechanical modes for trivial (non-trivial) cases where $d_{\mathrm{topo}} = a/2 = 275$ nm $(= 295$ nm$)$. It can be seen that the trivial design has two degenerated modes at 4.14 GHz which is opened for the trivial case resulting in a lower (upper) frequency of 4.03

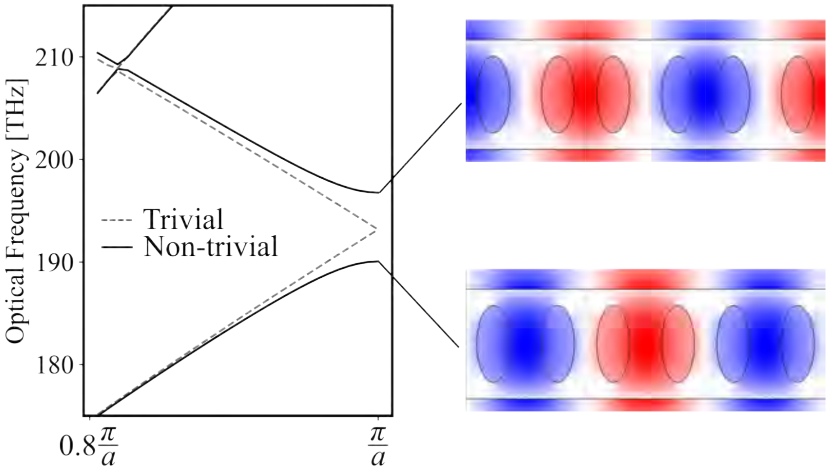

Figure 5.3: Optical band diagram of the trivial and non-trivial structure. The insets show the E_y of the upper and lower modes of the non-trivial case.

(4.25) GHz. This can be understood by looking at the mode profiles shown in the same figure. Both upper and lower bands have breathing-like modes whose displacement is localised at the gap between ellipses. The mechanical eigenfrequencies split due to the difference in the gap distance, which is originally degenerated in the trivial case where the gap distance is equal for all the ellipses. In our design, the longer gap distance gives rise to a higher mechanical frequency, while the shorter gap shows a lower frequency. Note that there are multiple mechanical modes which also show similar frequency splitting although we only consider the breathing mode expecting sufficiently strong optomechanical coupling. The corresponding energy splitting can be seen in the electrons in polyacetylene as well [25].

Together with the mechanical modes, the optical mode also shows the same energy splitting shown in Fig. 5.3. Opposite to the mechanics, the optical mode confined in the shorter gap has higher eigenfrequency. This is probably because the optical mode requires more energy to be confined in a smaller region. We find that the trivial structure has a degenerated frequency at 193.1 THz while the non-trivial structure has a lower (upper) frequency of 190.0 (196.7) THz.

Now we try to create the edge mode by connecting two SSH chains with different topological phases [83]. In our dimer model, the order of short and

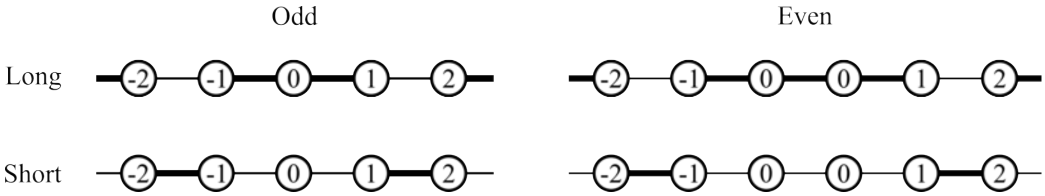

Figure 5.4: Designs of connection for SSH chains. The thick (narrow) bars correspond to large (small) gaps between ellipses. The number 0 is the centre ellipse(s) where these SSH chains are connected.

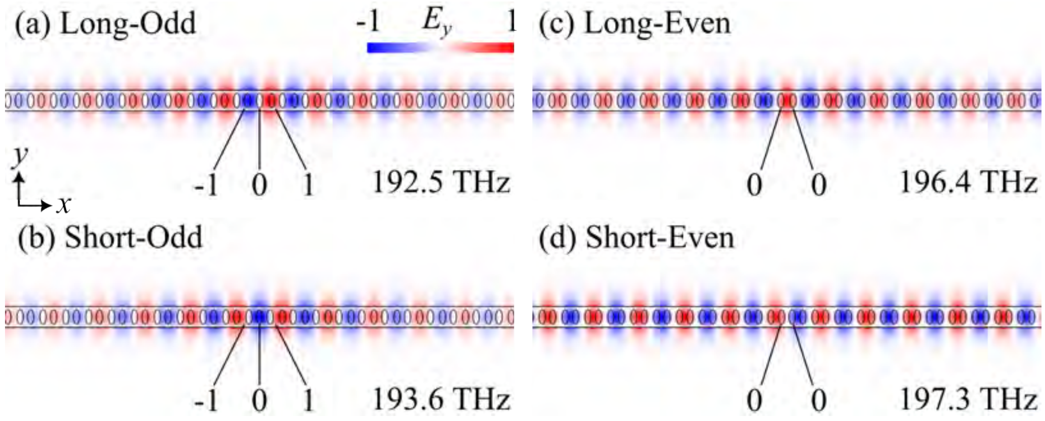

Figure 5.5: Simulated full optical modes for SSH topological nanobeams with different connections.

long gap distances between ellipses creates different topological phases, i.e. the short-long-short configuration is topologically different from the long-short-long configuration. Unlike polyacetylene molecules, we can arbitrarily design how to connect these chains and create the edge mode. We especially think of four configurations shown in Fig. 5.4. They are labeled as Long or Short, and Odd or Even. The Long (Short) configurations are two chains connected by large (small) gap distances. The Odd (Even) configuration has an odd (even) total ellipse number with one (two) central ellipse(s). Especially, the Odd configuration can be seen in the polyacetylene molecules [80].

We simulate the optical mode for those designs. Fig. 5.5 shows simulated E_y. The simulated geometry has 25 dimer unit cells on each side and the

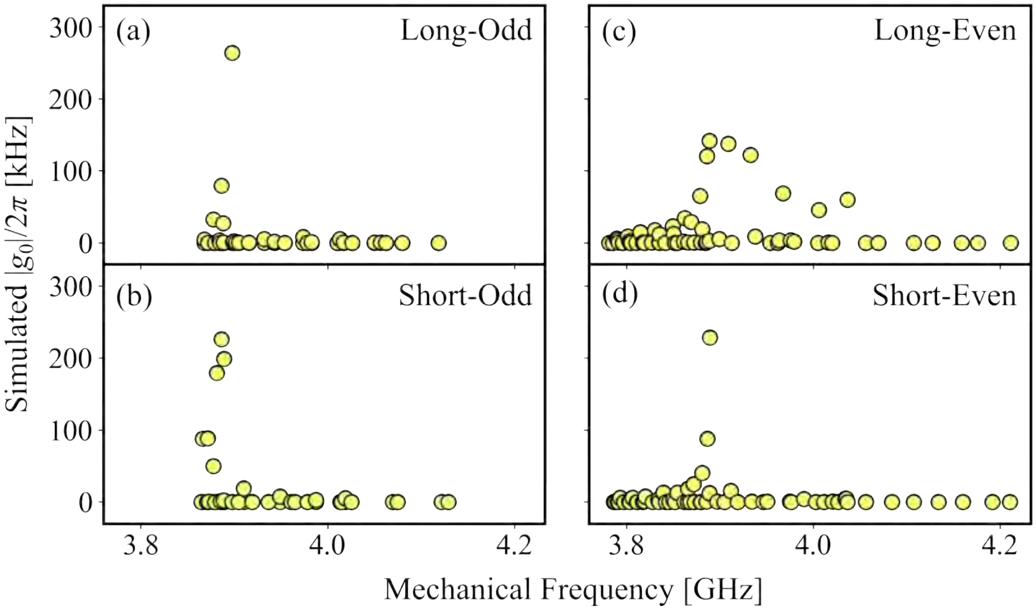

Figure 5.6: Simulated g_0 for SSH topological nanobeams with various connection configurations.

central ellipse(s). The mode profiles are different for each design. The Odd configurations have the optical mode whose energy is confined within the ellipse holes. The mode is confined to the odd-numbered holes in the Long-Odd design, while it is confined to the even-numbered holes in the Short-Odd design. On the other hand, the optical mode mostly exists in the ellipse gaps for the Even configurations. Similar to the Odd case, the high intensity exists either even (for Long-Even) or odd (for Short-Even) numbered-gap. These mode profiles with high intensity at alternating sites are quite similar to the electron probability distribution in polyacetylene [25, 80]. This suggests the optical mode originates from the topological feature.

Fig. 5.6 shows the simulated optomechanical coupling rate in those configurations. Among these, (a) Long-Odd and (d) Short-Even connections have a distinct mechanical mode with sufficient coupling strength, while others have several modes coupled to the optical mode. Some potential applications such as quantum memory require only one coupled mechanical mode, otherwise, the photon is transduced to one of many mechanical modes randomly and hard to retrieve it again. The Long-Odd has a slightly higher coupling rate $g_0/2\pi = 264$ kHz than that of the Short-Even $g_0/2\pi = 229$ kHz.

(a) Long-Odd (c) Long-Even

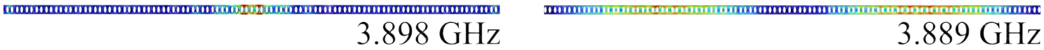

(b) Short-Odd (d) Short-Even

Figure 5.7: Simulated mechanical modes with the highest optomechanical coupling rate for each configuration.

Fig. 5 shows the simulated mechanical modes with the highest coupling rate for each configuration. (a) Long-Odd has the most strongly confined mode while the others have broader distributions. In terms of mechanical quality, we expect (a) Long-Odd configuration will have the highest quality factor when fabricated although it is difficult to estimate it with simulations. Considering optical and mechanical simulations as well as the coupling rate, (a) Long-Odd configuration shows the most favourable result.

Unlike the optical mode, the mechanical mode profile is more complex probably due to its mechanical anisotropy. This makes it difficult to optimise the geometry so that it possesses both a well-confined mode and a sufficient coupling rate. One of the straightforward solutions for further improvement is to modify the connection design. We have only examined the long and short gap distance at the connection which in principle can be arbitrary. More optimisation by sweeping the connection gap distance will increase the mode confinement. Another possible solution is to change the structural design itself. One example is a ring-shaped resonator with the same periodical dimers [84] rather than a nanobeam. Fig. 5.8 shows schematic images for the ring design idea with the SSH chain. These structures have no actual 'edge' of the device, therefore, the topological edge mode is expected to exist only at the connection region.

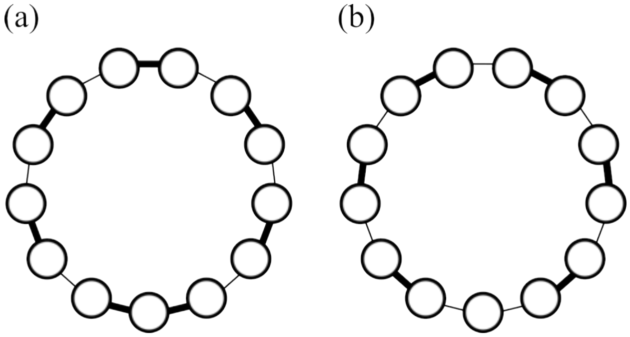

Figure 5.8: Schematic of ring-shaped SSH chain for future design. (a,b) Connections with Long-Odd and Short-Odd configurations respectively.

Chapter 6

Device Preparation

This chapter details how actual devices are fabricated and prepared for measurement. The etching process that creates the OMC pattern in the GaP layer is explained. Also, we show our effort in optimising the design suitable for the evanescent fibre coupling. For that, we show samples from the early stage of the work and discuss how it does not work. Finally, the fabrication technique of tapered fibre tips is explained.

Théo Martel and Rémy Braive at C2N, Paris-Saclay contribute to the fabrication process.

6.1 GaP Device Fabrication

OMC designs generally require quite high fabrication precision to achieve their ∼nm scale design. This is especially strict when realising the snowflake shapes due to its complex geometry compared to conventional ellipses. Our devices are fabricated with processes depicted in Fig. 6.1. As the first step, a chip, made of a GaP device layer on top of a GaAs substrate, is prepared. A 260 nm thick layer of GaP is epitaxially grown on the substrate. Then we deposit a thin (∼5 nm thick) silicon dioxide (SiO_2) layer on top with a chemical vapour deposition (CVD) reactor, making the following e-beam resist adhere to GaP. We make a 300 nm thick hydrogen silsesquioxane (HSQ) e-beam resist layer composed of a mixture of FOx-15 flowable oxide and methyl isobutyl ketone (MIBK) by spin-coating and soft baking. The chip is then installed in an electron beam (e-beam) writer and the OMC structure is drawn with a dose range of ∼4000 μC/cm^2 (Fig. 6.1(a)). The e-beam

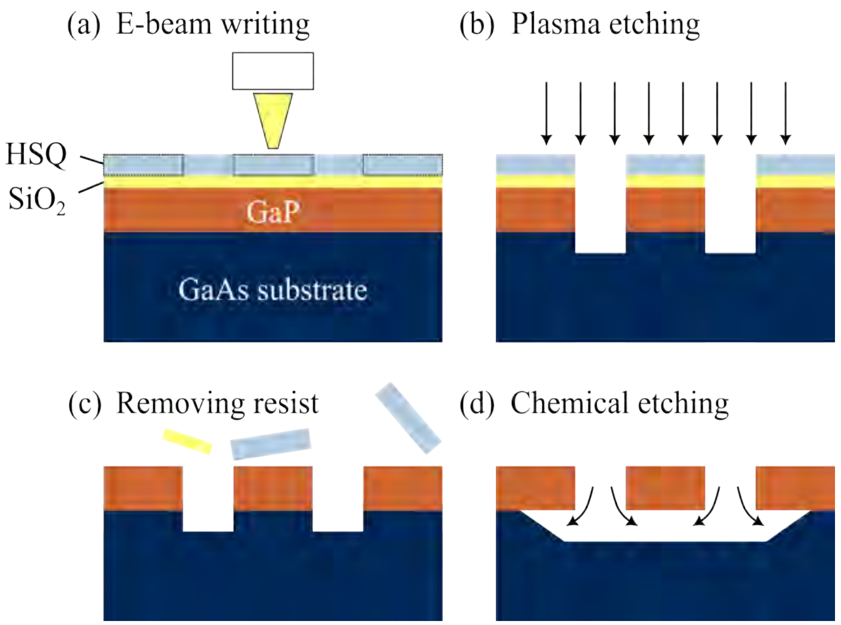

Figure 6.1: Device fabrication process. (a) Electron beam writing to draw the OMC pattern. (b) Development and plasma etching. (c) Removal of the resist and SiO_2 layer. (d) Chemical etching to undercut the device.

creates crosslinks between HSQ molecules and hardens them in the exposed area thus working as a negative resist.

After the development with buffered potassium hydroxide (KOH) based developer AZ® 400K, an inductively coupled plasma (ICP) reactive ion etcher creates the OMC pattern on the GaP layer (Fig. 6.1(b)). We use a gas mixture of HBr, O_2 and He for the etching. The remaining SiO_2 and HSQ are removed by submerging the chip in a buffered hydrofluoric acid (HF) solution (Fig. 6.1(c)). At this time the chip needs to be diced into 3 to 4 pieces according to a device arrangement. To do this, we cover the entire chip with a 10 μm thick AZ® 10XT resist to protect it from damage during the dicing process. Then the chip is precisely diced by a spinning diamond blade from its top side. The protection is cleaned with acetone and then with an isopropanol solution.

Further chemical etch process is required since our optical and mechanical modes are designed only for a free-standing device layer which is one of the current standards (although there are quite recent studies on non-suspended

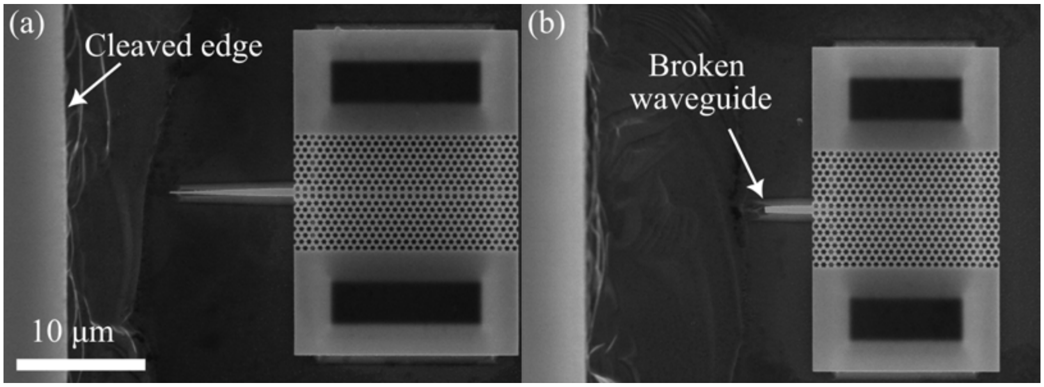

Figure 6.2: Scanning electron microscope images of early-stage devices. (a,b) Devices with survived and broken waveguide tips respectively.

OMCs, e.g. a clamped structure [24, 85], or bound-state in the continuum design [86, 87]). For this, we use a chemical solution composed of H_2SO_4, H_2O_2 and H_2O that selectively etches the GaAs substrate to release the GaP OMC.

6.2 Device Optimisation

Devices are not perfect from the beginning, rather they are required to be optimised for our measurements. Especially, we have tried a lot of device designs for better optical coupling. At the early stage of this work, we employed the butt-coupling with a lensed fibre which allows us fast alignment. Fig. 6.2 shows fabricated samples from that stage. OMCs are located on the edge of the chip which is cleaved in the dicing process mentioned above. They have ∼10 μm free-standing access waveguides attached to the OMCs. One of the key points here is the distance between the waveguide tip and the edge of the chip. It limits the closest distance a lensed fibre can approach to the waveguide and thus determines the optical coupling efficiency. We can control this by changing the position of the diamond dicing blade, and successful devices can have gap distances of ≤ 5 μm. However, as shown in Fig. 6.2(b), the waveguide tip can be easily damaged if they are cleaved too close.

The resulting chip is mounted on an aluminium plate shown in Fig. 6.3.

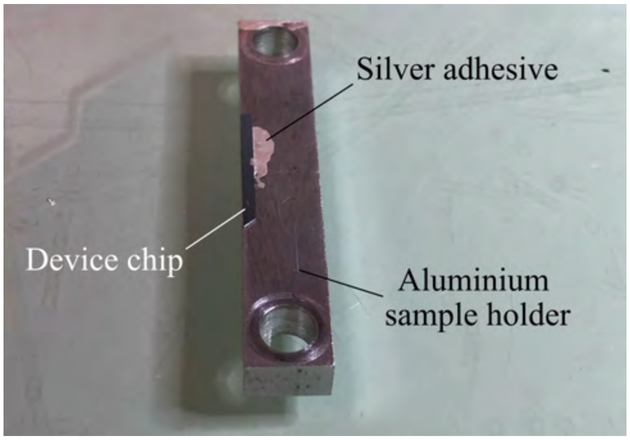

Figure 6.3: Sample holder for the earl-stage sample. A chip is mounted very close to the edge of an aluminium holder and glued with a silver adhesive.

The chip is positioned on the edge of (or slightly exceeds the edge) the holder so that a lensed fibre can approach it. Here OMCs are fabricated on the edge side. We use thermal conductive adhesive with silver to fix the chip position. This glue can diffuse the heat quickly and is expected to work in future cryogenic experiments.

As the next step, we have changed the optical coupling method from butt-coupling to more efficient fibre evanescent coupling [75]. Originally we tried to access the early-stage design with a tapered fibre. However, we have found it difficult to precisely position the fibre onto such a short free-standing waveguide. Therefore, we have redesigned the longer waveguide shown in Fig. 6.4. The total length is more than 30 μm and the waveguide is supported in the middle and on the tip by clamps. Also, the waveguide is bent by 45° in the middle to prevent the approaching fibre from touching the OMC structure directly which may damage the OMC. We have tested different support widths to find out the narrowest possible width as too wide supports may disturb the travelling optical mode. Fig. 6.4(a-c) shows 3 designs with 120, 80, and 40 nm support widths respectively. We have found the 40 nm width is too narrow to suspend the waveguide, and because of that, we have concluded at least 80 nm width of support is necessary. Note that this test is only for the feasibility of device fabrication not to ensure their resilience against the tapered fibre. Therefore, we employ a rather wider

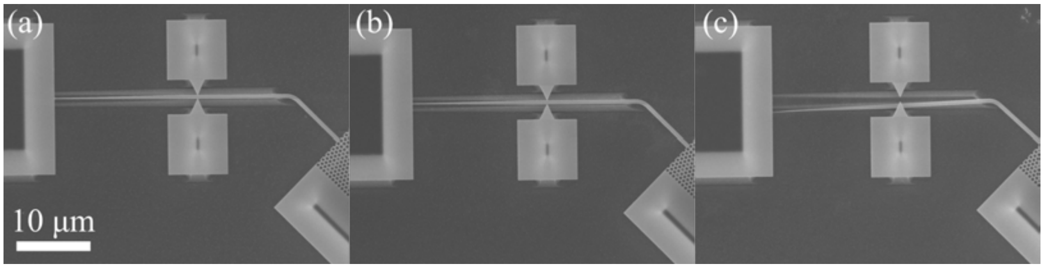

Figure 6.4: Test fabrication with different clamp widths. (a,b,c) The waveguide is supported by 120, 80 and 40 nm width of clamps on the side and end. 40 nm of width is not strong enough and the waveguide is detached.

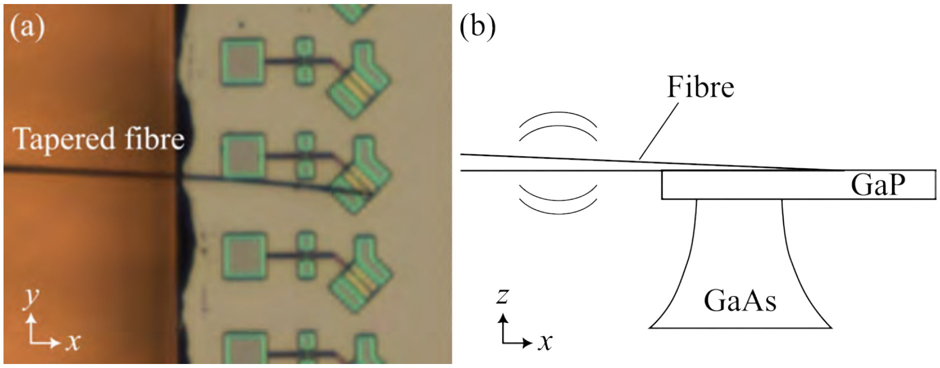

Figure 6.5: (a) An optical microscope image of failed fibre alignment. (b) Schematic to illustrate the fibre configuration for the unstable alignment.

width of 120 nm for further experiments.

With the devices in Fig. 6.4, we have tested the tapered fibre coupling, and unfortunately, it has ended in a quite disappointing result. Fig. 6.5(a) shows a typical failure of the fibre alignment with those devices where the tapered fibre lands far from the waveguide and is stuck in a gap below the GaP layer. We observed there are mainly 2 reasons to make it difficult. One is the waveguide is so narrow (500 nm) that the fibre slips away even when it touches. This happens because the waveguide is almost exposed and nothing prevents the fibre from slipping. The other reason is the fibre landing area is too small. Fig. 6.5(b) illustrates this issue. Even though the fibre tip touches the GaP device, the rest of the fibre still moves due to its flexibility makes

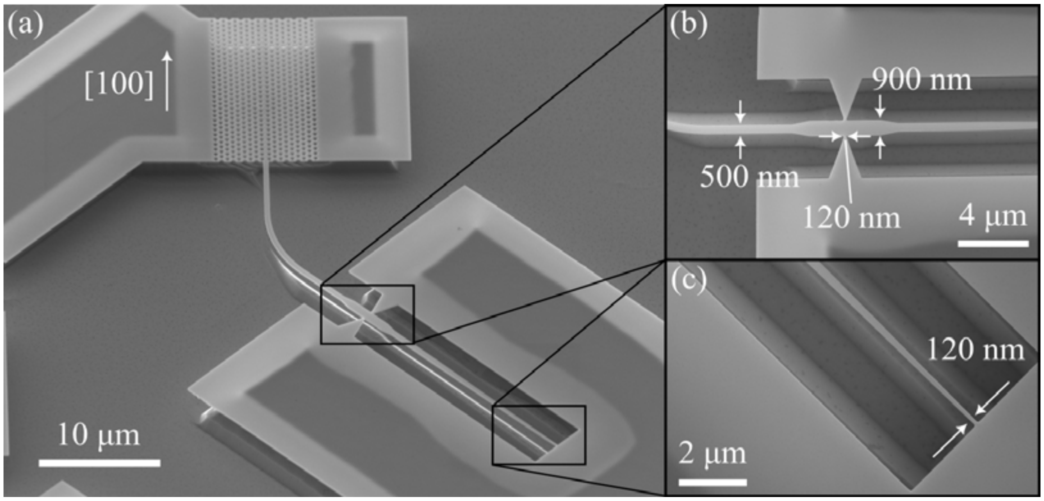

Figure 6.6: Scanning electron microscope images of a 2D GaP OMC device. (a) The overall view of the entire device. (b,c) Close-up image of a waveguide support and a tapered tip of the waveguide.

it unstable.

6.3 Final Design

To solve those alignment problems we have finally come to the final design shown in Fig. 6.6. The basic design is similar to the previous design but the waveguide is now surrounded by a bulk GaP layer which prevents the fibre from slipping away. The access waveguide has two clamps as shown in Fig. 6.6(b) to support the waveguide beam. To reduce the effect of the support, which often causes back-reflection or additional loss of the travelling field, a part of the waveguide is widened to 900 nm from the original 500 nm. Those supports touch the waveguide with a 120 nm width. The tip of the waveguide is then tapered and clamped to a part of the bulk (Fig. 6.6(c)). The tip width is set to 120 nm which is also expected to be narrow enough for the evanescent coupling to a fibre according to the simulation results from the previous chapter. To reduce the fibre motion, which caused fibre drifts, we enlarge the fibre landing area to $\sim$1 mm so that the fibre touches its long part. The landing area does not degrade the coupling efficiency as the

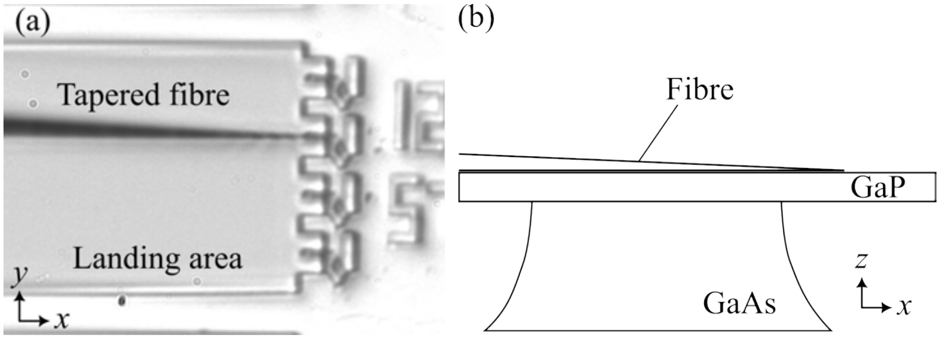

Figure 6.7: (a) An optical microscope image of successful fibre alignment. (b) Schematic to illustrate the fibre configuration for the stable alignment.

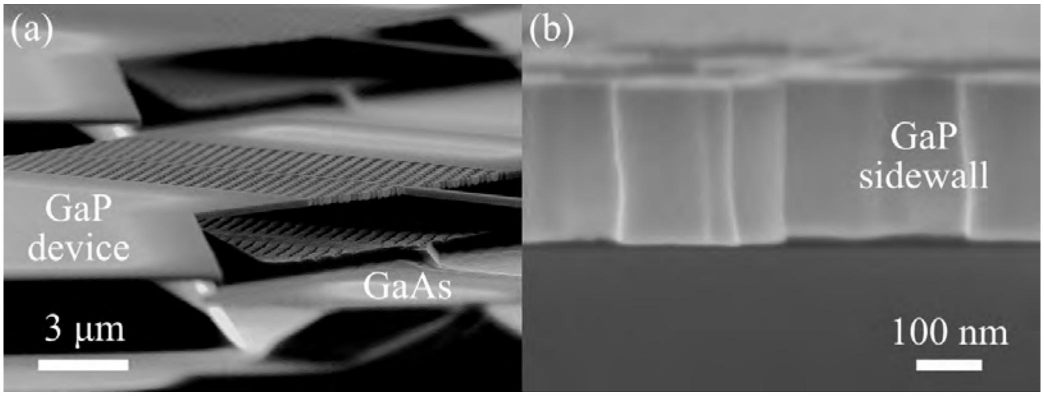

Figure 6.8: (a) Tilted SEM image for the side view of a device. (b) A cleaved sidewall of an OMC.

evanescent field only exists around the tip of the tapered fibre which is far enough from that area.

Finally, we examine the sidewall of the device. Fig. 6.8(a) is an SEM image of an angled view of a structure. This confirms that the OMC region is suspended well thanks to the chemical etching and detached from the substrate thanks to the chemical etch process. We further cleave one of the chips along the OMC with a manual diamond chip cleaver. From an SEM image of the cleaved cross-section Fig. 6.8(b), we find the side walls of our device have slight curves possibly originating from the ICP etching process. This curved side wall itself, however, does not seem to degrade the device performance, e.g. g_0, but differences in the curve profile from one position to another might limit the performance (see appendix for further detail).

6.4 Tapered Fibre Fabrication

Optical coupling to the OMC devices is viewed as an essential part that determines if single-photon operations are possible. For our tapered fibre coupling method, a very sharp tip (<1 μm) is necessary due to the narrow access waveguide of 500 nm width and to hold the evanescent field around it. Those micro- and nano-fibre have been intensely utilised in various fields ranging from nanophotonics [71, 72, 75] to atomic physics [88], both of which employ the strong evanescent filed around the fibre.

Two of the commonly used techniques to fabricate such fibres are the conventional heat-and-pull (HaP) [89–92] and relatively recent chemical etching methods [76]. The HaP method uses a heat source, either a flame torch or a CO_2 laser, that softens the fibre and then pulls it at both ends. The fibre gets elongated and the result is one connected tapered fibre if the process is stopped before the fibre gets split. When the fibre is pulled very quickly after some elongation, it becomes two split fibres with sharp tapered tips. This method is, at least for preparing fibre tips, not as reproducible as the chemical etching due to the randomness when the quick pulling motion splits it. Also, only two fibres can be fabricated in one process.

On the other hand, we employ the chemical etching scheme due to its high controllability, reproducibility, and capability to produce many fibres in one process. Fig. 6.8(a) shows our fibre etching setup in a cleanroom. $\sim$16 of single-mode (SM) fibres are stripped at the end and mounted to a fibre holder which is placed on a digitally controllable motorised stage. Then the fibres are submerged in a 40% HF etching solution for roughly 4 cm. The motorised stage pulls up the fibres at a constant speed $\sim$7 μm/s resulting in cone shape tips. The stage speed and concentration of the HF solution determine the angle of the cone shape. Fig. 6.8(b) shows a schematic image of the solution and the fibre during the process. The stripped bare SM fibres are immersed in the solution. The surface of the solution is covered by a *o*-Xylene liquid layer which prevents the HF from evaporating during the process. At the end of the process, those fibres are slowly submerged in an isopropanol solution for a couple of minutes for cleaning.

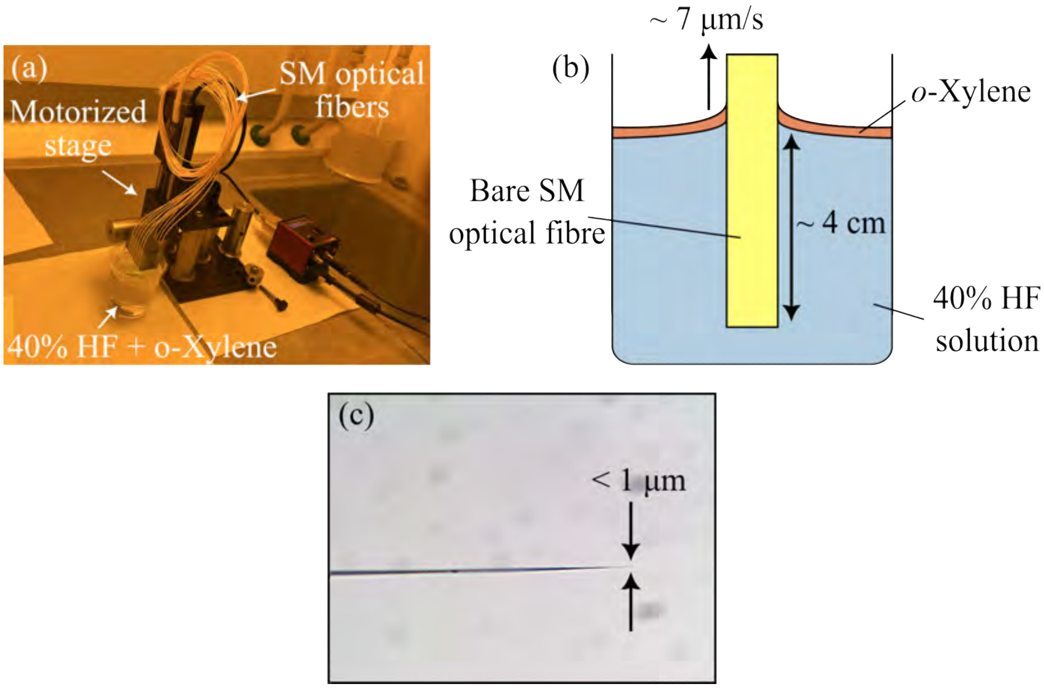

Figure 6.9: (a) Fibre etching setup in a cleanroom. (b) Schematic of the etching process. (c) Optical microscope image of an etched fibre tip.

Chapter 7

Device Characterisation

In this chapter, we characterise our device fabricated in the previous chapter. The first section provides optical properties and our setup for the fibre-waveguide coupling to the OMC. The next section shows the mechanical features of the device. We find three mechanical modes as predicted from the numerical simulation. We analyse the dynamical backaction effect for more detailed mechanical properties. Finally, we measure the vacuum optomechanical coupling rate g_0 with the calibration tone method.

7.1 Optical Mode

Here we characterise the optical properties of our device, e.g. eigenfrequency and linewidth. Fig. 7.1 is a schematic of the experimental setup. Throughout the experiments, we use a TLB-6728 tunable diode laser whose output wavelength ranges from 1520 to 1570 nm. An optical isolator right after the laser blocks undesired reflection from coming back to the laser. The laser intensity is attenuated by a variable optical attenuator (VOA) which a Redpitaya digitally controls. This is necessary to avoid the unwanted thermo-optical nonlinearity [93] but yet to sustain sufficient signal-to-noise ratio of the mechanical signal in later experiments. The thermo-optical nonlinearity shifts the optical resonance toward a lower frequency as the laser power increases. Polarisation of the field is manually controlled by a fibre polarisation controller so that it matches the relevant optical mode of the travelling waveguide and OMC modes. An optical circulator delivers the input field into a device path. A bare fibre coupler (BFC) connects the fibre patch cable to a bare

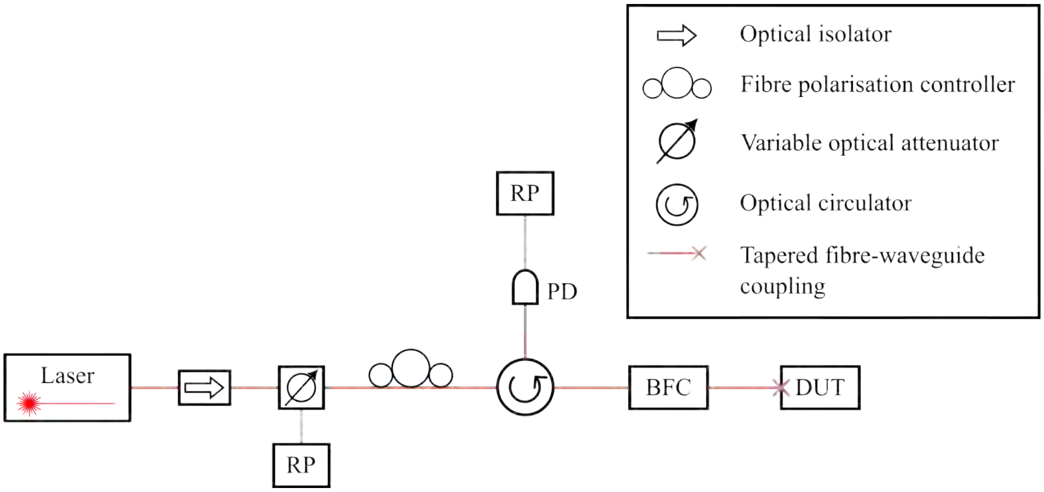

Figure 7.1: Schematic of the measurement setup for optical characterisation. RP: Redpitaya, PD: photodetector, BFC: bare fibre coupler, and DUT: device under test.

fibre whose other end is tapered in the etching process. Then the tapered fibre tip couples to a waveguide of a device under test (DUT). Reflection is sent to a photodetector (PD) and another RP analyses its photocurrent.

The evanescent fibre coupling method requires precise alignment such that the fibre tip touches the 500 nm wide waveguide. Fig. 7.2(a) is our fibre alignment setup. The input fibre is mounted on a v-groove fibre holder whose position is controlled by manual translational stages. The fibre angle is also manually controllable. Our device chip is glued on a copper device holder with silver conductive adhesive. The holder is placed on digitally controlled piezo motorised stages. First, the fibre is roughly placed above the desired OMC structure with the manual translational stages. Then the piezo motors precisely move the sample position by monitoring the reflection intensity with the PD and RP. Polarisation of the input field is also controlled during the process.

Fig. 7.2(b) depicts the image of the fibre-waveguide coupling configuration. We monitor the rough fibre position with a long working distance microscope while positioning the fibre.

We estimate the evanescent fibre coupling efficiency by comparing the input and output power from the device. The input is measured right after the BFC with another cable patch fibre and a power meter, while the output

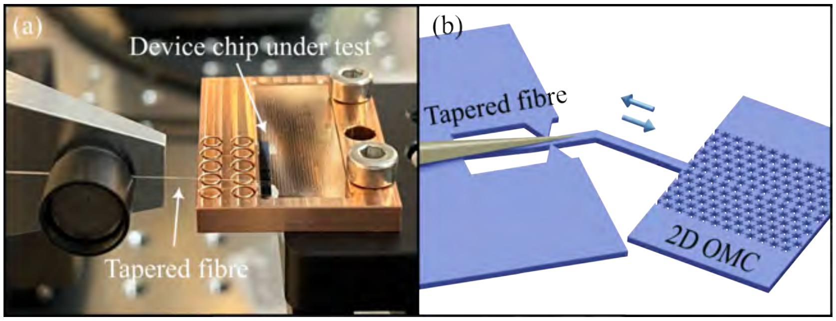

Figure 7.2: (a) Image of the fibre coupling setup. (b) Schematic of the coupling configuration.

from the OMC is measured at the output port of the optical isolator. The wavelength of the laser is set to far enough from the optical resonance of the OMC so that we get strong reflection during the estimation. We adjust the polarisation to maximise the reflection. By taking the additional losses from BFC, isolator and other fibre connectors into account, we estimate the coupling efficiency achieves ∼60%. This can be further improved by adjusting the waveguide geometry and the angle of the cone tip. Typically, a sharper fibre tip angle extends the range of the evanescent field. This contributes to more efficient coupling as the light transfers from the fibre to the waveguide more gradually. However, this requires a longer contact distance where the fibre and waveguide must be aligned. Also, the evanescent field may diffuse through the substrate if the fibre is too sharp resulting in additional loss.

The optical spectrum is obtained by sweeping the laser wavelength while measuring the reflection intensity with the PD. A broad wavelength sweep results in Fig. 7.3(a) that shows a narrow dip at $\lambda_0 = 1533.1$ nm corresponds to the optical resonance of our OMC. The sinusoidal background seems to be some interference effect possibly due to back reflection from the waveguide or fibre. Theoretical analysis reveals that this parasitic back reflection may affect measurements on optomechanical coupling rate g_0 (see appendix).

Another fine scanning Fig. 7.3(b) shows the detail of the optical resonance. Laser detuning $\Delta/2\pi$ ranging $\sim \pm 40$ GHz shows optical resonance $\omega_0/2\pi = 195.55$ THz and a loaded linewidth $\kappa/2\pi = 2.47$ GHz (quality factor $Q_\text{o} = 79{,}200$). The Fano fit curve for the reflection $R(\Delta)$

$$R(\Delta) = h - A\frac{(1-q^2)\kappa/2 - q\Delta}{\kappa^2/4 + \Delta^2}, \tag{7.1}$$

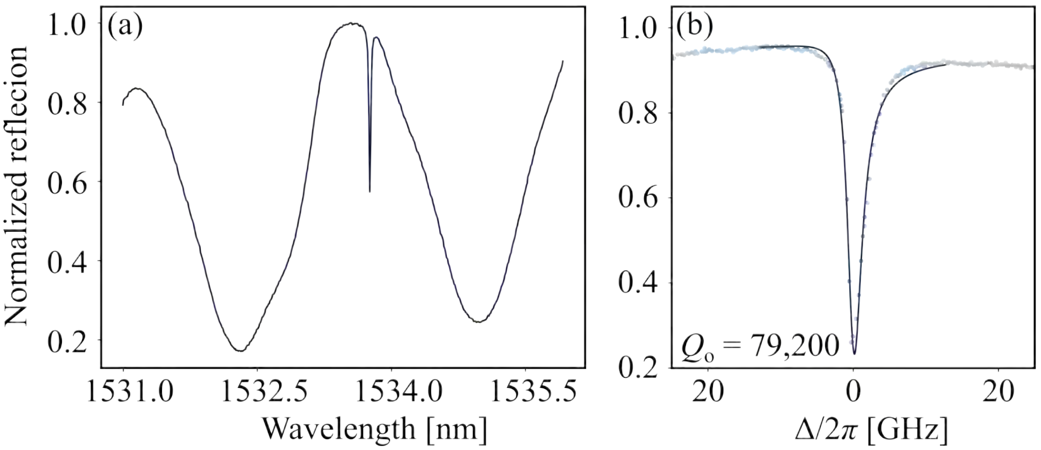

Figure 7.3: (a) Broad scan of the optical spectrum. A narrow optical resonance is found at 1533.1 nm. (b) Finer scan of the optical spectrum with different detuning Δ around the optical resonance $\omega_0/2\pi = 195.55$ THz.

describes our optical resonance. Here we define the offset h, amplitude parameter A, and Fano parameter q. This suggests that parasitic interferences exist possibly due to the back reflection from the waveguide or tapered fibre (see appendix A.3).

7.2 Mechanical Mode

Now we characterise the mechanical motion of the OMC. The simulation from the previous chapter predicts there must be mechanical resonances around 5-8 GHz. Mechanical spectra can be obtained by measuring the intensity modulation of output light. This is because mechanical displacement shifts the phase of the incoming optical field thus resulting in phase modulation at the mechanical frequency. In the case of a cavity optomechanical system, where the mechanics interact with cavity photons, the phase modulation is transferred into intensity modulation due to the quadrature rotation of light by the optical cavity. Fig. 7.4 is the measurement setup for mechanical properties. A difference from the optical measurement setup is that the reflection light from DUT is now split into two paths with a 1:99 ratio. Most of the light is further amplified by an erbium-doped fibre amplifier (EDFA)

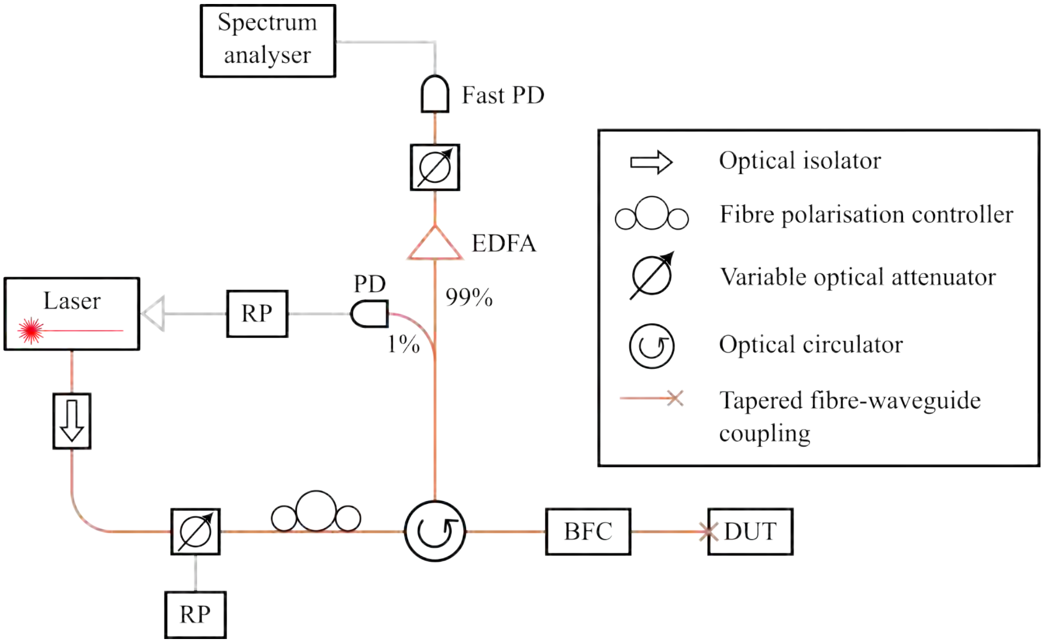

Figure 7.4: Schematic of the measurement setup for mechanical characterisation.

so the fast PD can detect small signals. Our fast PD can acquire signals from DC to 10 GHz frequency components. The photocurrent from the fast PD is analysed by a spectrum analyser which shows the mechanical spectrum.

First, we measure the mechanical frequencies. To do so, we take a broad frequency scan with the spectrum analyser shown in Fig. 7.5. We find three narrow peaks in the power spectral density (PSD) at around $\Omega_{\mathrm{m}}/2\pi = 5.7$, 6.5, 7.7 GHz, as predicted from the simulation. We label them as mode 1-3 and the corresponding simulated mechanical mode profiles are shown in the insets. We find that the mechanical frequencies of those modes exceed the optical linewidth, placing them in the resolved-sideband regime $\kappa < \Omega_{\mathrm{m}}$. This is a prerequisite for some quantum applications as we can selectively realise either the beam-splitter or two-mode squeezing Hamiltonian according to the detuning. In the unresolved-sideband regime $\kappa \not< \Omega_{\mathrm{m}}$, both of the above Hamiltonians inevitably exist simultaneously.

The mechanical motion is always influenced by the optical cavity mode called the dynamical backaction [34], therefore the mechanical frequency and linewidth can change depending on the intensity and detuning of the input

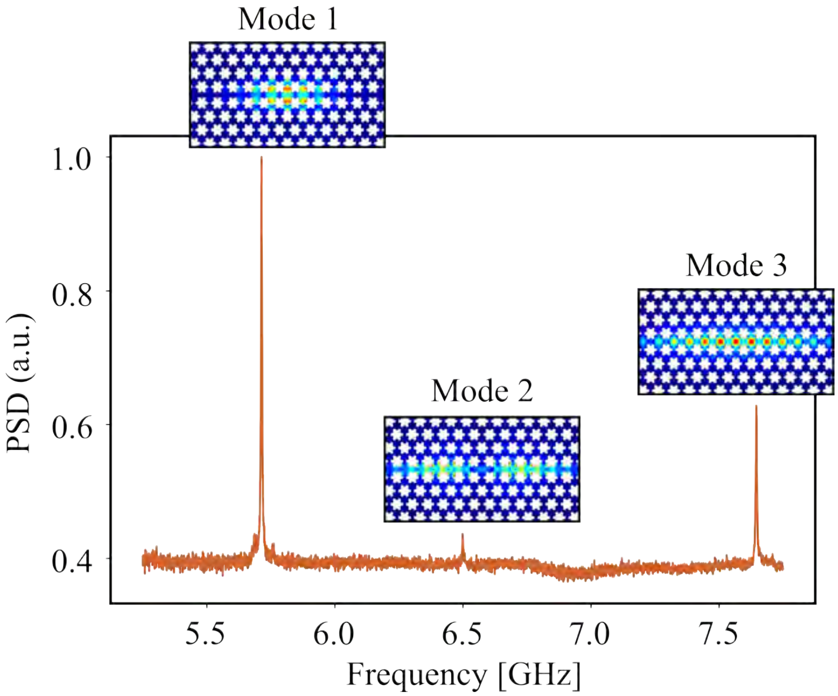

Figure 7.5: Broad scan of the mechanical power spectrum density. Insets show the simulated mechanical displacement for each mode.

laser. In order to obtain the intrinsic mechanical parameters, we analyse the mechanical spectra with different laser detuning at a fixed input power. 1% of reflection is monitored by a PD and an RP which is then used for a feedback control to lock the wavelength to a desired detuning.

Fig. 7.6 shows the detail of how to obtain detunings during the characterisation. The optical spectrum is measured before and after the mechanical measurement to compensate for the drifts of the optical spectrum due to e.g. fibre or polarisation drift. When we take the mechanical spectrum, a DC component of the reflection power is also monitored so we compare the reflected power to the fitted optical curve. This gives us detunings for locked points. In our setup, the locking range is limited to roughly within the optical linewidth ($|\Delta| \lesssim \kappa$) because the feedback relies on the slope of the optical spectrum and the slope is too flat at $|\Delta| \gtrsim \kappa$. For the same reason, it can not lock the wavelength exactly in the vicinity of the optical resonance.

Fig. 7.7 shows measured shifts in the mechanical frequency and linewidth

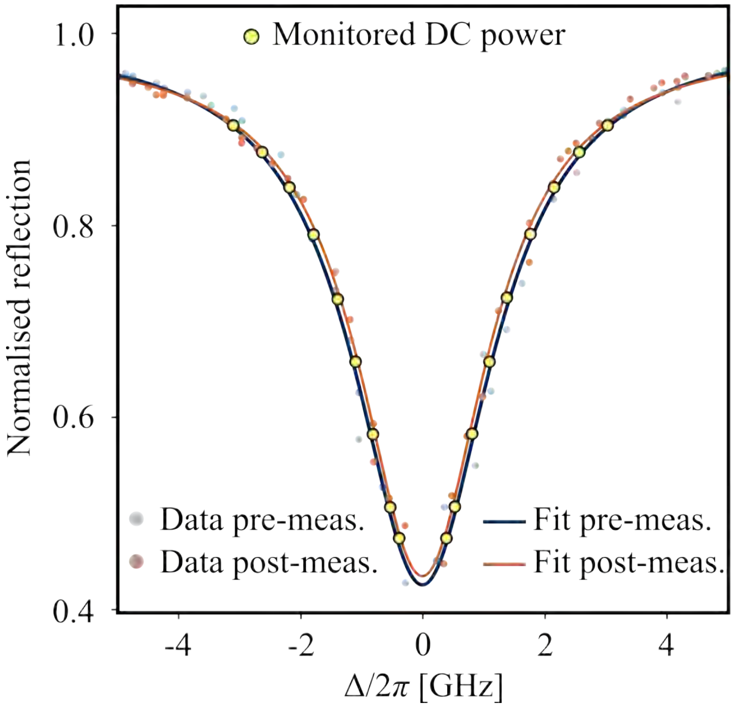

Figure 7.6: A typical optical spectrum for determining laser detuning. Spectra are taken before and after the mechanical measurement cycles. The monitored DC powers are compared to the mean value of those fitted curves.

with various detuning for modes 1 and 3. The error bar of each data point is the standard deviation of the Lorentz curve fitting the individual mechanical spectra. For the shifts, we use the fitting curves

$$\Omega_{\mathrm{eff}} = \Omega_{\mathrm{m}} + \delta\Omega_{\mathrm{m}}, \tag{7.2}$$

$$\delta\Omega_{\mathrm{m}} = g_0^2 \frac{\kappa_{\mathrm{ex}}}{\Delta^2 + (\kappa/2)^2} \frac{P}{\hbar\omega_{\mathrm{L}}} \left(\frac{\Delta - \Omega_{\mathrm{m}}}{\kappa^2/4 + (\Delta - \Omega_{\mathrm{m}})^2} + \frac{\Delta + \Omega_{\mathrm{m}}}{\kappa^2/4 + (\Delta + \Omega_{\mathrm{m}})^2} \right), \tag{7.3}$$

$$\Gamma_{\mathrm{eff}} = \Gamma_{\mathrm{m}} + \delta\Gamma_{\mathrm{m}}, \tag{7.4}$$

$$\delta\Gamma_{\mathrm{m}} = g_0^2 \frac{\kappa_{\mathrm{ex}}}{\Delta^2 + (\kappa/2)^2} \frac{P}{\hbar\omega_{\mathrm{L}}} \left(\frac{\kappa}{\kappa^2/4 + (\Delta + \Omega_m)^2} - \frac{\kappa}{\kappa^2/4 + (\Delta - \Omega_m)^2} \right), \tag{7.5}$$

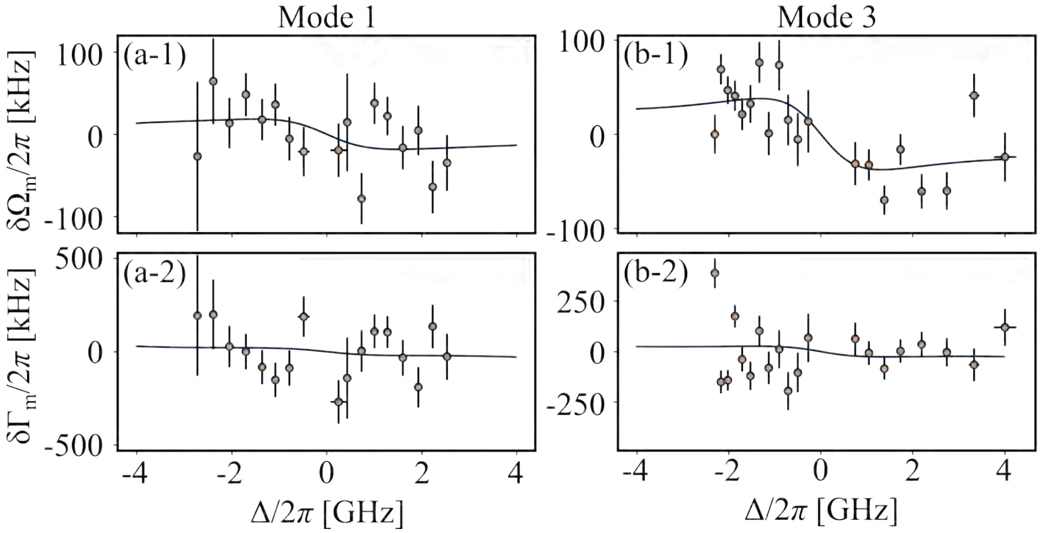

Figure 7.7: Dynamical back-action measurement results. (a,b) Shifts in the frequency and linewidth for modes 1 and 3, respectively. Laser power is set to constant while the wavelength is locked to some detunings.

where we define intrinsic frequency Ω_m, linewidth Γ_m, input power to the optical cavity P, and external cavity loss κ_ex. The detuning Δ is estimated by comparing optical reflection power to the Lorentzian shape of the cavity mode. From the fitting, we estimate $(\Omega_\mathrm{m},\Gamma_\mathrm{m})/2\pi$ = (5.71±0.01 GHz, 4.57±0.03 MHz) for mode 1 and (7.65±0.01 GHz, 4.91±0.03 MHz) for mode 3, respectively. This corresponds to mechanical quality factors $Q_\mathrm{m} \coloneqq \Omega_\mathrm{m}/\Gamma_\mathrm{m}$ $= 1.25\times10^3$ for mode 1 and 1.56×10^3 for mode 3. We ignore mode 2 because of the relatively small mechanical signal due to the small coupling rate g_0.

It can be seen that the dynamical backaction effect above is rather small and it is not really clear, especially for the mechanical linewidths. This is because all of the modes are sideband-resolved quite well and the laser detunings are only within the optical linewidth. One can expect a larger effect when the detuning is set to one of the sideband $\Delta\pm\Omega_\mathrm{m}$. However, in our measurement setup, the slope locking only allows us to lock the wavelength within the optical linewidth.

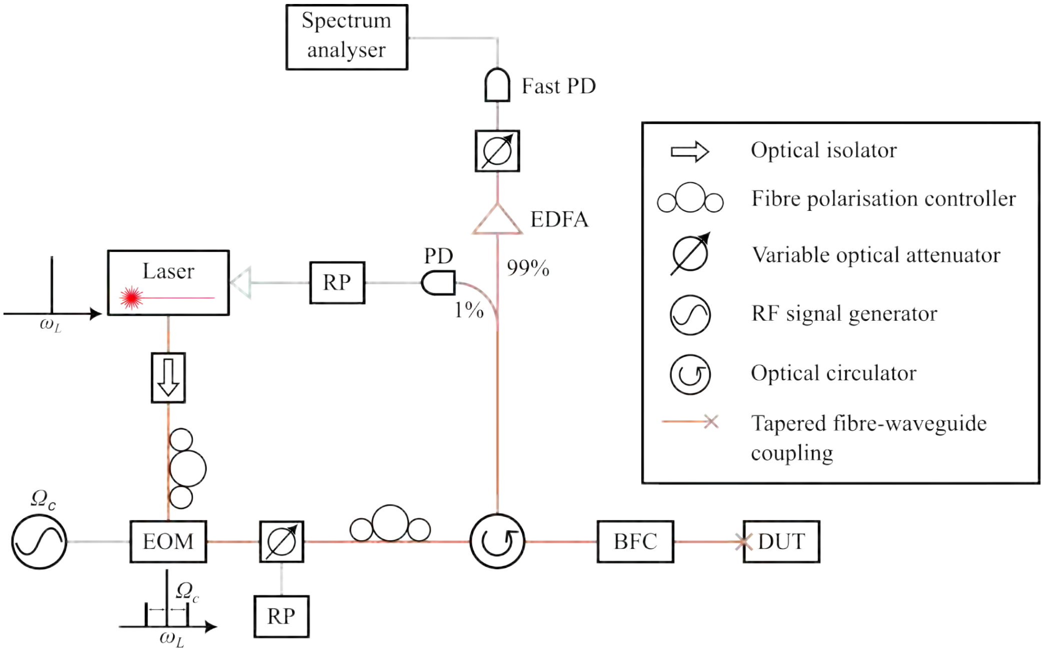

Figure 7.8: Schematic of the measurement setup to determine g_0 with the calibration method.

7.3 Optomechanical Coupling

Furthermore, we estimate one of the most important parameters, the vacuum optomechanical coupling rate g_0. Among several methods such as taking mechanical broadening [40] or sideband assymetry [15], we employ the calibration method [94]. This method does not require the knowledge of intra cavity photon numbers.

To do so, we use the measurement setup shown in Fig.7.8. A difference from the mechanical measurement setup is that now we phase-modulate the input field with an electro-optic modulator (EOM). With a radio frequency drive at Ω_c, the EOM creates two calibration tones to the carrier frequency as

$$E_0 e^{-i\omega_\mathrm{L} t} \rightarrow E_0 e^{-i\omega_\mathrm{L} t} \left(1 + \frac{\phi_0}{2} e^{-i\Omega_\mathrm{c} t} - \frac{\phi_0}{2} e^{i\Omega_\mathrm{c} t}\right), \tag{7.6}$$

where we define the laser amplitude E_0, carrier frequency ω_L, modulation depth ϕ_0 as well as calibration frequency Ω_c. Our measurement is insensitive

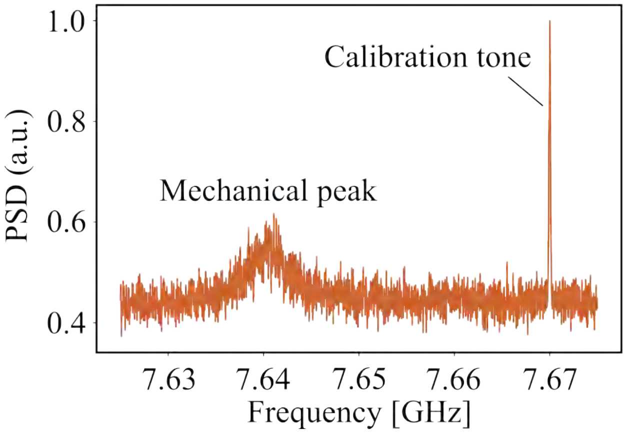

Figure 7.9: Typical power spectral density for the calibration method.

to the phase modulation eq.(7.6). However, according to the detuning, the optical cavity transduces the phase modulation to intensity modulation with the quadrature rotation. Assuming the quadrature rotation occurs equally to both the mechanical signal and calibration tone, the vacuum optomechanical coupling rate g_0 is estimated by comparing the areas below the two peaks. The exact expression is given as [94]:

$$g_0 \approx \sqrt{\frac{\phi_0^2 \Omega_\mathrm{c}^2}{4 \langle n_\mathrm{th} \rangle} \frac{S_{II}^\mathrm{meas}(\Omega_\mathrm{m}) \Gamma_\mathrm{m}/4}{S_{II}^\mathrm{meas}(\Omega_\mathrm{c}) f_\mathrm{ENBW}}}, \tag{7.7}$$

where f_ENBW is the effective noise bandwidth (ENBW) of the spectrum analyser in linear frequency, $S_{II}^\mathrm{meas}(\Omega)$ the symmetrised noise power spectral density at Ω, and thermal occupation of the mechanical motion$\langle n_\mathrm{th} \rangle \approx k_\mathrm{B} T/\hbar\Omega_\mathrm{m}$. Here we simply multiply the peak heights by their linewidths and compare them, instead of comparing the area directly. The modulation depth ϕ_0 is given as

$$\phi_0 = \frac{\pi V}{V_\pi}, \tag{7.8}$$

where V is the driving voltage of the RF signal generator and $V_\pi = 6.5$ V in our EOM.

A typical power spectral density for the calibration method looks Fig. 7.9. Mechanical frequency and linewidth are extracted by fitting the mechanical

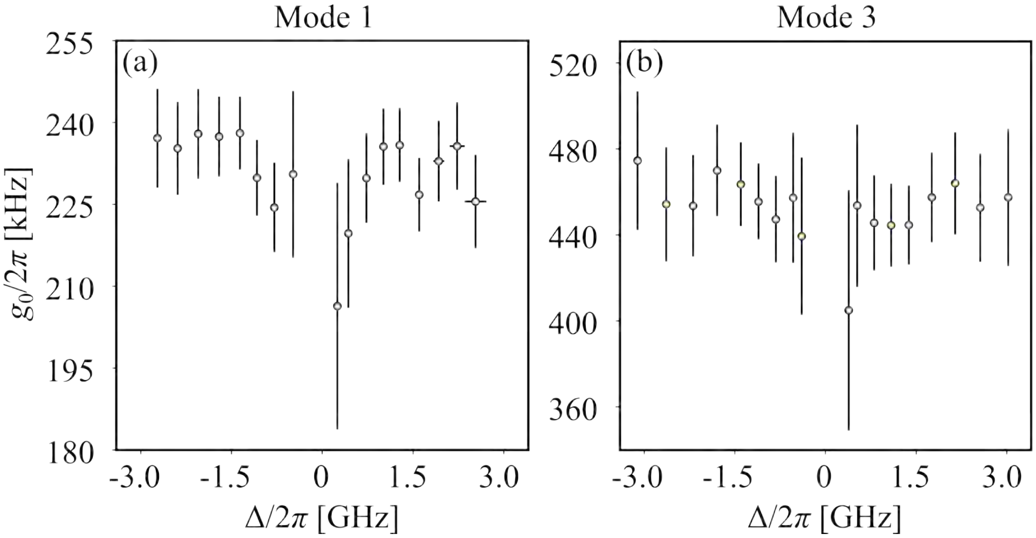

Figure 7.10: (a,b) Measured vacuum optomechanical coupling rate g_0 for mode 1 and 3.

peak with a Lorentz shape. On the other hand, the calibration tone is so narrow and the spectrum analyser can not resolve it. Instead, the width of the calibration tone depends on the bandwidth of the spectrum analyser called ENBW, which can be digitally changed, thus resulting in a Gaussian distribution. For all the characterisations, the calibration frequency is set to no farther than 40 MHz from the mechanical frequency to let the measurement setup respond equally to both signals. Also note that eq.(7.7) only gives the absolute value of the coupling rate. However, it does not make a significant difference as, in this work, the sign is out of our scope.

The results of the calibration method are shown in Fig. 7.10 for modes 1 and 3. By taking a mean value over the detuning, we obtain $g_0/2\pi = 231\pm13$ (452 ± 32) kHz for mode 1 (3). Compared to the simulated results, the measured values are a factor of 2-3 small. Previous studies on 1D GaP optomechanical crystals at room temperatures have also reported a similar order of reduction [14, 17]. As discussed in those works, one possible explanation relates to our imperfect knowledge of the material properties of GaP, particularly its photoelasticity. Our simulations use the photoelastic constants at 632.8 nm because, to the best of our knowledge, sufficient research has not been conducted at 1550 nm yet. Another also possible origin of this reduction is the fabrication imperfection which causes random disorder in

Mode	Measured parameters				
	$\Omega_\mathrm{m}/2\pi$ [GHz]	$\Gamma_\mathrm{m}/2\pi$ [MHz]	Ω_m/κ	$g_0/2\pi$ [kHz]	$\mathcal{C}_0 = 4g_0^2/\Gamma_\mathrm{m}\kappa$
This work					
Mode 1	5.71 ± 0.01	4.57 ± 0.04	**2.31**	231 ± 13	1.89×10^{-5}
Mode 2	6.50 ± 0.01	3.93 ± 0.41	**2.63**		
Mode 3	7.65 ± 0.01	4.91 ± 0.03	**3.10**	452 ± 32	6.74×10^{-5}
Schneider *et al.* [14]	2.90	3.13	0.92	370-680	$5.55\text{-}18.8 \times 10^{-5}$
Hönl *et al.* [17]					
Mode A	3.28	2.55	1.12	191	1.96×10^{-5}
Mode B	3.31	2.81	1.13	283	3.90×10^{-5}
Mode C	3.33	2.56	1.14	293	4.59×10^{-5}
Stockill *et al.* [15]	2.91	**0.014** (@ 7 mK)	0.56	**845**	$\mathbf{4.03 \times 10^{-2}}$

Table 7.1: Comparison of measured parameters from different GaP OMCs.

the OMC design. We have seen the sidewalls are slightly rounded in the previous chapter, which may disturb the optical and mechanical confinement. We discuss this part with numerical simulation in an appendix.

Theoretically, the calibration method works at any detuning giving a constant value. However, actual devices may show distorted results due to dynamical backaction or imperfect optical lineshape originating from unexpected back-reflection.

Comparison of our device with other relevant devices reveals significant advantages to our 2D design. Table 7.1 compares our results with 3 other works on GaP OMC by Schneider *et al.* [14], Hönl *et al.* [17], and Stockill *et al.* [15]. Our device shows by far the highest mechanical frequencies; they are 2-3 times higher than those of the 1D devices thanks to the 2D geometry. This is reasonably expected considering studies on 1D and 2D silicon OMCs [21,40]. This allows our device to have the highest Ω_m/κ ratio (Ω_m/κ=3.1 for mode 3 while other 1D designs have typically $\Omega_\mathrm{m}/\kappa \sim 1$); thus placing it in the resolved-sideband regime easily. Given that, our device will be a favourable candidate for the optomechanical state conversion as we can selectively turn on the beam-splitter Hamiltonian at red detuning while suppressing the two-mode squeezing Hamiltonian. Our device possesses one of the highest vacuum optomechanical coupling rates g_0 and mechanical quality factor Q_m among the room temperature experiments.

With the measured g_0, as well as previous mechanical and optical characterisation, we can estimate the single-photon cooperativity $\mathcal{C}_0 = 4g_0^2/\Gamma_\mathrm{m}\kappa$, a figure of merit to assess how favourable the device is for quantum operations. The value can be understood as the optomechanical cooperativity per cavity photon. We achieve $\mathcal{C}_0 = 6.74 \times 10^{-5}$ for mode 3 being one of the highest among the room temperature GaP OMCs studied so far. For cryogenic and quantum operations, one of the most important figures of merit is the quantum cooperativity $\mathcal{C}_\mathrm{q} = n_\mathrm{cav}\mathcal{C}_0/n_\mathrm{th}$. In the situation where $\mathcal{C}_\mathrm{q} > 1$, optomechanical state conversions take place faster than the mechanical decoherence, allowing us to realise quantum mechanical memories. For that application, one needs a large cavity photon number n_cav while suppressing mechanical thermal occupation n_th which also can be heated by the cavity photons [12, 13]. Naively assuming $\mathcal{C}_0$ is unchanged from room to cryogenic temperature and a condition $n_\mathrm{th} \leq 1$, rather large amount of cavity photons $n_\mathrm{cav} = 10^4 - 10^5$ is required. However, comparing 1D GaP OMC at room temperature [14] with the one at low temperature [15], $\mathcal{C}_0$ increases by three orders of magnitude. If this is also applied to our 2D structure, we require a much smaller number of photons $n_\mathrm{cav} = 10 - 100$, and would be less laser heating.

Chapter 8

Conclusions

8.1 Summary of the Results

In this thesis, we have explored the OMC designs made of GaP. This is motivated by the large electron gap of GaP which is expected to suppress the two-photon absorption at telecom frequency. We present two OMC designs, the two-dimensional and SSH topological ones based on FEM simulations. The characterisation experiment reveals the 2D design achieves the resolved sideband regime with $\Omega_{\mathrm{m}}/\kappa = 3.10$, the highest among previously reported GaP OMCs. The measured vacuum optomechanical coupling rate $g_0/2\pi = 452$ kHz and the single-photon cooperativity $\mathcal{C}_0 = 6.74 \times 10^{-5}$ are both one of the highest compared to similar devices. Considering the characterisation results and the optical properties of GaP, our device will be a promising candidate for quantum memories of light.

We also develop the fibre optical coupling method. The best result we obtain is 60% of coupling efficiency which we can improve even more. We believe this method will enable a package of the device and access fibre which will be cryogenic compatible.

8.2 Outlook

This PhD has started in the context of collaboration work in the Hy-Q research center at the Niels Bohr Institute with a strong motivation to control single photons with an optomechanical system. At the early stage of the project, we concluded that an OMC was probably the most suitable platform which was completely new to us. Therefore, this PhD work has encountered a lot of difficulties due to the lack of experience.

Although we managed to obtain sufficient outcomes in the end, three and a half years was not enough for the author to complete this ambitious project. Therefore, the author believes it is worth providing an outlook of future work, given the considerable time and effort spent on planning. Here, we provide how we will move on to the cryogenic experiments and the protocol for the single-photon memory.

8.2.1 Improving Fibre Coupling

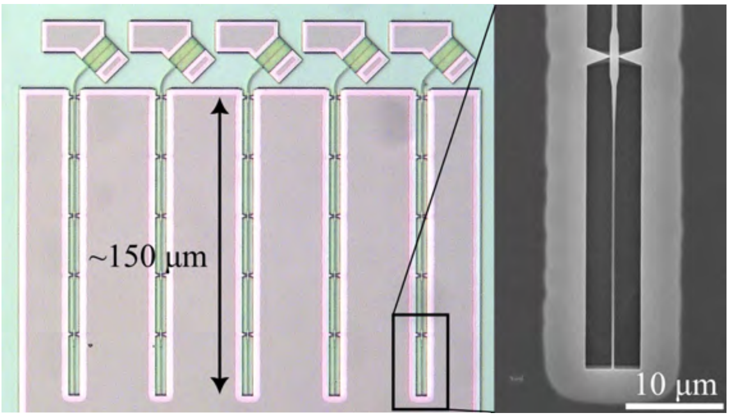

Figure 8.1: Microscope images of the preliminary waveguide. The total length is roughly 150 μm. The tip of the waveguide is a simply narrowed rectangle with width of 120 nm.

The first problem we need to solve is the fibre-waveguide coupling efficiency since the 60% of coupling may not be enough for effective photon storage. One of the most promising methods for improving the coupling is to optimise the waveguide shape. This is because the fibre tip shape is not precisely controllable although we can roughly change the tip angle by changing the pulling speed at the chemical etching. On the other hand, the waveguide is drawn by the e-beam writer and can be precisely controlled in an nm scale.

More precisely, the coupling efficiency is limited by the difficulty of the alignment. The efficiency is extremely sensitive to where the fibre contacts the waveguide, which can not be perfectly controlled in our setup. Therefore, a promising solution will be to redesign the waveguide so that it is easier to align the fibre and less sensitive to the fibre position. Fig. 8.1 shows microscopic images of a preliminary waveguide design. They are more than 5 times longer than that shown in this thesis. We expect this design to enable longer fibre-waveguide contact which will make the alignment easier. Also, the waveguide has a simply narrowed tip rather than a tapered one. This will allow the evanescent field to exist longer range also reducing the sensitivity to the fibre position.

8.2.2 Cryogenic Packaging of a Device

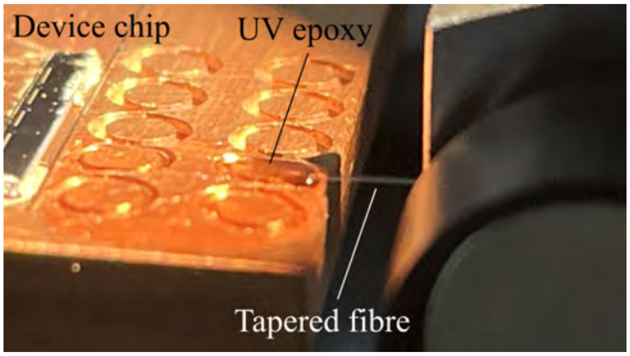

Figure 8.2: Optical image of a glued fibre tip. The device chip is mounted on a copper holder with silver adhesive. The tapered fibre is glued with a UV epoxy drop.

To conduct experiments at low temperatures, we employ the cryogenic packaging method [77, 78, 95] that can significantly simplify the optical coupling to a device in a dilution refrigerator. Those methods require fixing the fibre position to a certain place with an adhesive such as UV epoxy. We especially follow the same method previously achieved on a diamond photonic crystal cavity [78]. In that study, a tapered fibre is placed on the coupling waveguide and then glued to the mounting plate with droplets of UV epoxy. The study has reported the fibre stays in contact even after several cycles of cooling process down to 77 K.

We have also tried this method and Fig. 8.2 shows our trial. We mount the device chip on a recessed region of a copper plate with a silver adhesive (Agar Silver Paint G302). First, some droplets of UV epoxy (Norland Optical Adhesive 88) are placed on the copper plate in front of the chip, then the fibre is aligned to the waveguide. The circle slits on the plate are to prevent the droplets from flowing and spreading. During the fibre alignment, the fibre is always immersed in a droplet. Once the alignment is completed, we shine UV light to cure the droplet and fix the fibre position.

However, at the time of submitting this thesis, our trial has not yet succeeded. This is because the fibre drifts slightly during the UV curing and the tip appears detached from the waveguide. We believe the volume of the UV adhesive changes when it coagulates. We can try other adhesives with different viscosity or durability. Also, we expect the previously mentioned longer waveguide design will be more tolerant to the drift thanks to the longer contact distance.

8.2.3 Quantum Memory with OMC

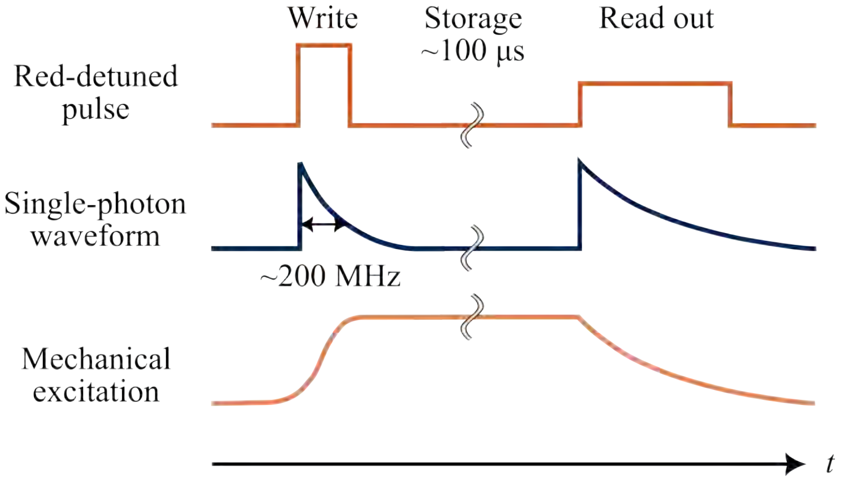

Figure 8.3: Schematic of an optomechanical memory protocol for single-photons.

Lastly, we discuss the protocol of the single-photon quantum memory with an OMC which represents the ultimate objective of this work. We assume a situation where a photon is emitted by a GaAs-based quantum dot (QD) single-photon source [60]. QD is currently considered one of the most common and reliable single-photon sources thanks to its high efficiency and emission rate. Fig. 8.3 shows a schematic of the storage scheme. The coming single-photon has an exponentially decaying temporal waveform due to the spontaneous emission. The linewidth of the photon ∼200 MHz has been reported [96] at around 950 nm wavelength which can be converted into that of telecom C-band [97] so it resonates with the optical mode of the OMC. Here, the linewidth of the emitted photon is an important factor that determines the storage efficiency. An optomechanical system must have the optomechanical conversion rate $\Gamma_{\mathrm{opt}} = 4n_{\mathrm{cav}}g_0^2/\kappa$ matched to the single-photon's linewidth. It should be noted that, in reality, we can not arbitrarily enhance Γ_{opt} by increasing the laser power due to the added noise originating from the laser heating.

During the "write" process of the OMC quantum memory, a red-detuned driving pulse is injected together with the single-photon. The pulse mediates the beam-splitter Hamiltonian which converts the single-photon to a mechanical excitation. The intensity must be sufficiently strong for efficient conversions. Once the photon is stored in the mechanical mode, the driving laser is turned off which preserves the information for its coherent time. We aim at ∼100 μs of mechanical coherence time at cryogenic temperature. Then we inject another red-detuned pulse when the information needs to be read out which converts the mechanical excitation to photon emission. It is important to note that the temporal waveform of the read-out photon depends on the pulse intensity. By lowering the intensity, for example, we make the OMC emit the photon slowly. This results in a longer waveform than that of the original single-photon and, therefore narrower linewidth. This also suggests another interesting possibility that is the arbitrary waveform generator with an optomechanical system. We can, in principle, engineer the waveform in the desired shape such as exponentially increasing function by controlling the intensity of the red-detuned pulse. A theoretical treatment for the protocol is given in the appendix.

List of Publications

The work presented in this thesis has led to the following preprint article:

- [98] Sho Tamaki, Mads Bjerregaard Kristensen, Théo Martel, Rémy Braive, and Albert Schliesser. A two-dimensional gallium phosphide optomechanical crystal in the resolved-sideband regime. *arXiv:2408.12474*, 2024.

The following is the previous preprint article with the contribution of the author with no link to the work presented in this thesis:

- [99] Sho Tamaki, Tomohiro Yokoyama, and Hajime Ishihara. Nonlocal inelastic scattering of light: Enhanced and noiseless signals in remote-coupled optomechanical systems. *arXiv:2110.00193*, 2021.

Appendix A

Appendices

A.1 FEM Simulations with COMSOL

A.1.1 Full Geometry

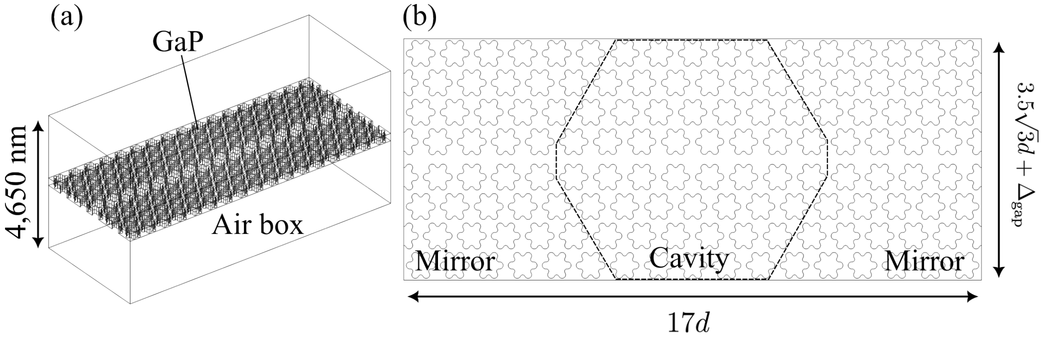

Figure A.1: Simulated geometries. (a) A tilted view of the entire geometry. (b) A top image of the geometry.

COMSOL [66] is one of the most used FEM solver software in various fields of science and engineering. It is a power tool to simulate multiple physics e.g., electromagnetism and solid mechanics of the same structure. However, because of the high functionality, even a small difference in the setting parameter can cause totally different simulation results. This appendix presents the details of the COMSOL simulation we use for the simulation results in the main chapters. We take the 2D OMC simulation as an example here.

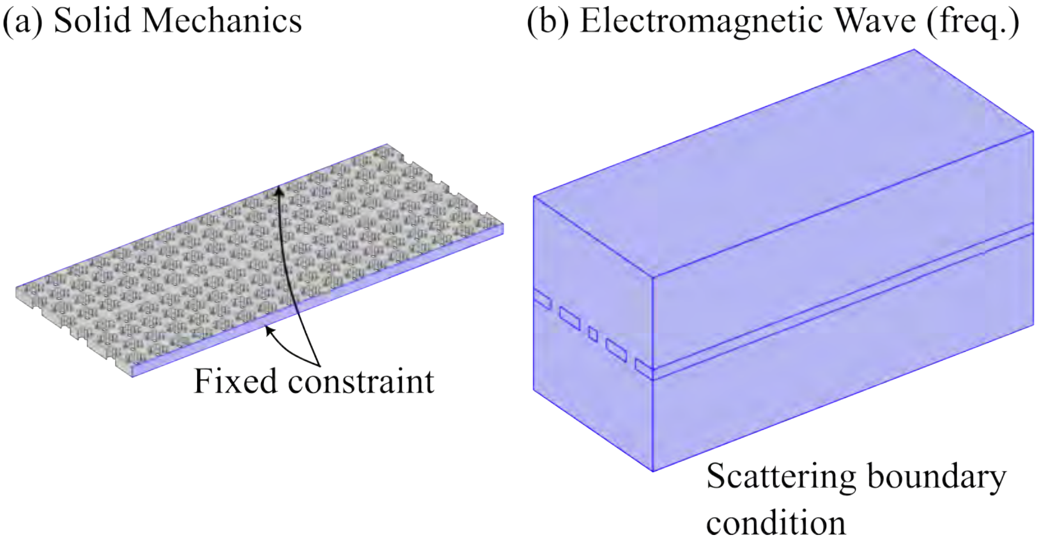

Figure A.2: (a) Fixed boundary condition for the solid mechanics. (b) Scattering boundary condition for the electromagnetic wave, frequency domain.

Fig. A.1 shows the entire simulated geometry consisting of the GaP device slab and an air box surrounding it. The height of the air box is set to large enough $3 \times 1{,}550$ nm $= 4{,}650$ nm so that the optical cavity mode is well held inside. The depth (size in the y-axis) of the air box (and therefore the GaP slab too), is set to $3.5\sqrt{3}d + \Delta_{\mathrm{gap}}$ which is the exact size to hold a total of 8 rows of snowflakes including the waveguide gap Δ_{gap}. The depth seems reasonable considering the strong confinement of the optical and mechanical modes shown in the main text. The width (size in the x-axis) spans $17d$ which hold 17 snowflakes. Since it is an odd number, the snowflakes on the edge are cut in half, which is also the case for the fabricated device. We apply the Solid Mechanics module to the GaP slab and the Electromagnetic Wave (Frequency Domain) module to the whole geometry.

A.1.2 Physics Setting

In FEM simulations, the boundary condition is one of the crucial parts which significantly affects the simulation results. We require somewhat different conditions for mechanics and optics. The mechanical motion needs to be fixed on the edges as the real device is clamped as well, and the optical mode requires no scattering from the boundary. Fig. A.2 depicts the boundary conditions for those physics modules. The boundary condition for the solid mechanics is relevantly straight forward, where we set the fixed constraint boundary on the edge of the GaP slab, as shown in (a). Now mechanical displacement is not allowed on this condition ($\mathbf{u} = 0$ at the boundary). This is quite reasonable considering the actual device is clamped on those edges (see Fig. 6.6).

The optics part is more complex because there are some options to reduce the back reflection. In principle, one should add the perfectly matched layer (PML) so that the electric field only dissipates and does not get reflected by the surface. PML is the additional domain whose permittivity and permeability have imaginary parts, decaying the transmitting electromagnetic field. However, due to the limitations of our computer, PML is computationally expensive. We then apply the scattering boundary condition (SBC) to all the boundaries. To understand the SBC, we restrict ourselves to a 2D plane shown in Fig. A.3. Here, we only consider the electric field with the out-of-plane component scattered from the modelling region to the outside. The 1st order SBC is given as [66]

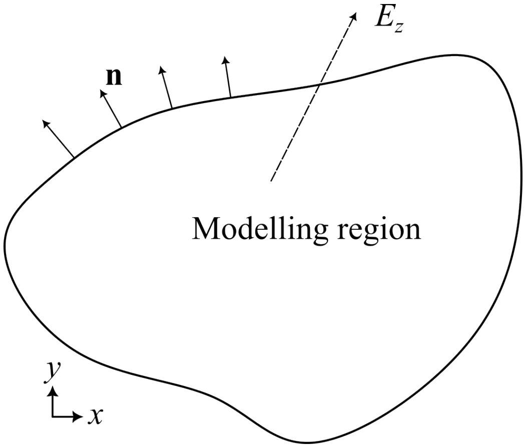

Figure A.3: Schematic of a 2D modelling region for the scattering boundary condition.

$$\mathbf{n} \cdot (\nabla E_z) + ik_0 E_z = 0, \tag{A.1}$$

where we define the unit normal vector to the surface of the modelling region: $\mathbf{n}$, the out-of-plane scattered electric field: E_z, and the wavenumber: k_0.

Also, the 2nd order SBC is given as

$$\mathbf{n} \cdot (\nabla E_z) + ik_0 E_z - \frac{i}{2k_0} \nabla_t^2 E_z = 0, \tag{A.2}$$

where ∇_t^2 is the second tangential derivative along the boundary. In the software version we use (5.6 and 6.2), the 2nd order SBC is automatically applied to the selected boundaries.

Now we move on to the setting for the solid mechanics module. GaP is a mechanically anisotropic material, so we need to include it in the setting. This can be done at "Solid Mechanics" > "Linear Elastic Material" > "Material symmetry" and then by choosing "Anisotropic", shown in Fig. A.4. In the same setting, we need to input the anisotropic elastic tensor of the simulated material. In the case of GaP or other cubic crystals, the tensor is given as eq.(4.1). This setting makes the x-axis of the geometry the [100] crystalline axis of the device, therefore we may need to align those axes according to the OMC structure. For that, one can either physically rotate the geometry or redefine the coordinate system in "Definitions" > "Base Vector Systems" and then apply it to the solid mechanics module.

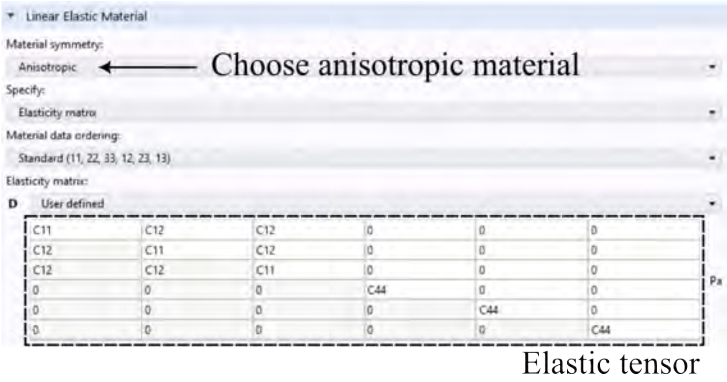

▾ Linear Elastic Material

Material symmetry:
Anisotropic

Choose anisotropic material

Specify:
Elasticity matrix

Material data ordering:
Standard (11, 22, 33, 12, 23, 13)

Elasticity matrix:
D User defined

C11	C12	C12	0	0	0
C12	C11	C12	0	0	0
C12	C12	C11	0	0	0
0	0	0	C44	0	0
0	0	0	0	C44	0
0	0	0	0	0	C44

Pa

Elastic tensor

Figure A.4: A screenshot of the setting for the mechanical anisotropy.

A.1.3 Optomechanical Coupling

The vacuum optomechanical coupling rate is one of the most important parameters of the device's performance. It can also be calculated using the same software. First of all, we need to normalise the mechanical displacement and the electric energy stored as they are in principle arbitrary values. The mechanical motion can be normalised by taking the absolute value of the maximum displacement over the geometry. This can be obtained in ”Results” > ”Derived Values” > ”Volume Maximum” and by typing,

```
Maximum Displacement [m]: sqrt(abs(u)^2+abs(v)^2+abs(w)^2)
```

which gives us the maximum displacement in the unit of length ([m] by default). For the rest of the analysis, the mechanical displacement $\mathbf{u}(\mathbf{r})$ is divided by this value. With this, we can obtain the effective mass of the motion m_{eff}. In ”Volume Integral”, it is calculated by

```
  Effective mass [kg*m^2]: solid.rho*( abs(u)^2 + abs(v)^2 +
      abs(w)^2 )
```

and by normalising it with $\max(\mathbf{u}(\mathbf{r}))$.

Similar to solid mechanics, we can calculate the electric energy stored in the geometry which is used to normalise the electric field. In ”Volume Integral”, we can use

```
  Stored electric energy [J]: epsilon0_const*epsilon_GaP*(
      abs(Ex)^2 + abs(Ey)^2 + abs(Ez)^2 )
```

where we define the relative permittivity of GaP, `epsilon_GaP`=9.3262. We can define parameters in ”Results” > ”Parameters”. The stored electric energy is exactly the integral that appears in the denominator of eq. (3.4) and eq. (3.19). Now we get the energy shift due to the photoelastic and moving boundary contributions. They can be calculated in ”Volume Integral” as

```
Photoelastic energy [J]: real(-epsilon0_const*(n_GaP^4)*(
    2*real(conj(Ex)*Ey)*p44*solid.eXY +
    2*real(conj(Ex)*Ez)*p44*solid.eXZ +
    2*real(conj(Ey)*Ez)*p44*solid.eYZ + (abs(Ex)^2)*(
    p11*solid.eXX+p12*(solid.eYY+solid.eZZ) ) + (abs(Ey)^2)*(
    p11*solid.eYY + p12*(solid.eXX+solid.eZZ) ) + (abs(Ez)^2)*(
    p11*solid.eZZ + p12*(solid.eXX+solid.eYY) ) ) )
Moving boundary energy [J]: real(u*nX+v*nY+w*nZ)*(
    epsilon0_const*(epsilon_GaP-1)*(
    abs(ewfd.tEx)^2+abs(ewfd.tEy)^2+abs(ewfd.tEz)^2 ) -
```

```
(1/epsilon0_const)*((1/epsilon_GaP)-1)*( (abs(nX*ewfd.Dx))^2
+ (abs(nY*ewfd.Dy))^2 + (abs(nZ*ewfd.Dz))^2 ) ).
```

Here we define the refractive index of GaP `n_GaP`, and the photoelastic tensor components `p11`, `p22`, and `p44`. Note that they correspond to the spacial integrals that appear in the numerator of eq. (3.19) and eq. (3.4).

We finally arrive at the coupling rate g_0 with those simulated values. We have

$$m_{\mathrm{eff}} = \frac{\texttt{Effective mass}}{\texttt{Maximum Displacement}^2} \tag{A.3}$$

$$x_{\mathrm{zpf}} = \sqrt{\frac{\hbar}{2m_{\mathrm{eff}}\Omega_{\mathrm{m}}}} \tag{A.4}$$

$$g_0^{\mathrm{PE}} = -\frac{\omega_{\mathrm{o}}}{2}\frac{x_{\mathrm{zpf}} \times \texttt{Photoelestic energy}}{\texttt{Max Displacement}\times\texttt{Stored electric energy}} \tag{A.5}$$

$$g_0^{\mathrm{MB}} = -\frac{\omega_{\mathrm{o}}}{2}\frac{x_{\mathrm{zpf}} \times \texttt{Moving boundary energy}}{\texttt{Max Displacement}\times\texttt{Stored electric energy}}. \tag{A.6}$$

A.2 Effect from the curved sidewall

In the fabrication chapter of the main text, we have seen the sidewalls of our OMC device are not perfectly straight but rather rounded. This is possibly due to the proximity effect during the e-beam process or lack of optimisation of the gas mixture during the plasma etching, and so on. It is important to understand how vulnerable our device is to such fabrication imperfection although it is usually difficult to reproduce those effects in simulations. In this appendix section, we consider a very simplified model shown in Fig. A.5 trying to give a somewhat qualitative explanation for the huge difference in measured and simulated g_0. As we can see in Fig. A.5(a,b) the upper half of the slab looks quite straight while the bottom half is rounded. Based on those images, we think of a model structure Fig. A.5(c) with a quadratic curve only on the bottom half of the snowflakes. The widest part of the snowflake hole is set to 5% wider than that of the straight part. We simulate this structure assuming the widened ratio is constant in the whole device.

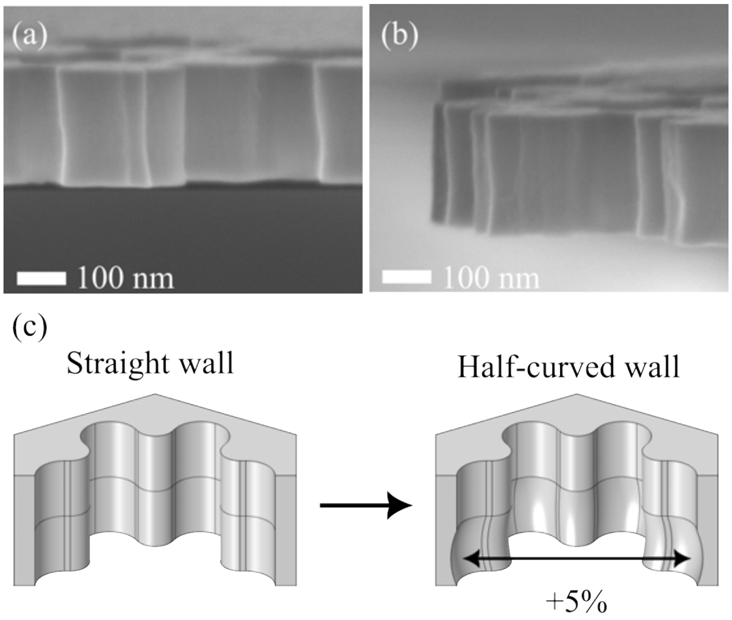

Figure A.5: (a,b) SEM image of a cleaved GaP OMC from different angles. (c) Simulation model for quadratically curved sidewall.

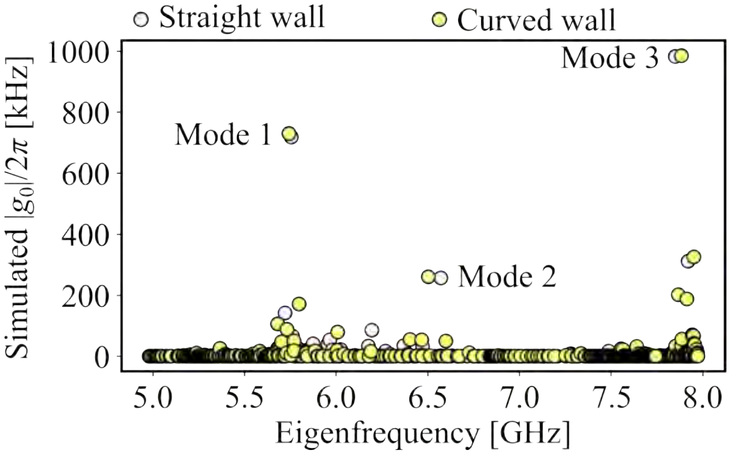

Figure A.6: Simulated $|g_0|$ for straight- and curved-sidewall devices.

By following the same simulation method already discussed in chapter 4, we obtained the cavity optical and mechanical modes and calculated the vacuum optomechanical coupling rates. Fig. A.6 shows the absolute value of the total coupling rate $|g_0|$ for each mechanical eigenmode in the case of straight- and curved-sidewall. First of all, the curved wall slightly shifts both mechanical and optical frequencies. We find mechanical frequency changes from (5.754, 6.570, 7.850) GHz to (5.743, 6.504, 7.883) GHz for modes 1 to 3, respectively, and optical frequency from 192.7 THz to 195.1 THz. We also find g_0 changes slightly although they are too small compared to the huge decline we have observed in the experiments.

We can conclude that our design is not really susceptible to the sidewall itself because such a small curve will not change the mechanical and optical mode profiles significantly. However, we can still speculate that, if the curve appears randomly from one point to another then device performances could be degraded. This is quite reasonable by recalling our cavity design; the cavity region has only 3% smaller snowflakes than that of bulk.

Another possible explanation for the big degradation, other than our imperfect knowledge of the photoelasticity of GaP, is the surface roughness of devices. There could have existed any type of thin oxide layer on the surface or a non-smooth surface which might degrade the optical mode. Since we have not seen any degradation over time, such surface impurity might have originated from our fabrication process itself.

A.3 Residual Back-Reflection Effect

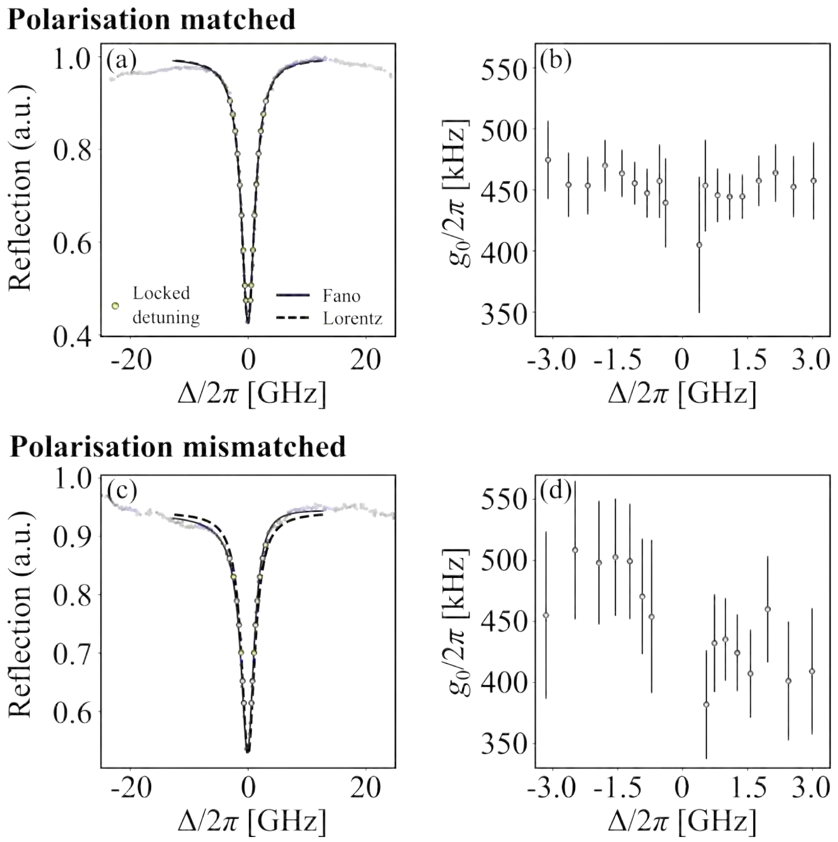

Figure A.7: Comparison of vacuum optomechanical measurements in different polarisation conditions. (a,b) Optical spectrum and resulting g_0 in matched polarisation. (c,d) Results in mismatched polarisation.

The calibration tone method to characterise g_0 can be easily degraded by the polarisation mismatch of the input field from the waveguide mode. This is due to the parasitic back reflection at the fiber-waveguide section which creates a sinusoidal optical spectrum background. For a polarisation condition, where the optical spectrum is symmetric Fig.A.7(a), the calibration presents consistent g_0 over detuning Fig.A.7(b). Here, the yellow dots represent the locked laser detuning. However, under the polarisation mismatched condition Fig.A.7(c) where optical lineshape is not perfectly symmetric, estimated g_0 deviates from the intrinsic value as in Fig.A.7(d), even without dynamical back-action. This condition significantly depends on fibre position relative to the waveguide.

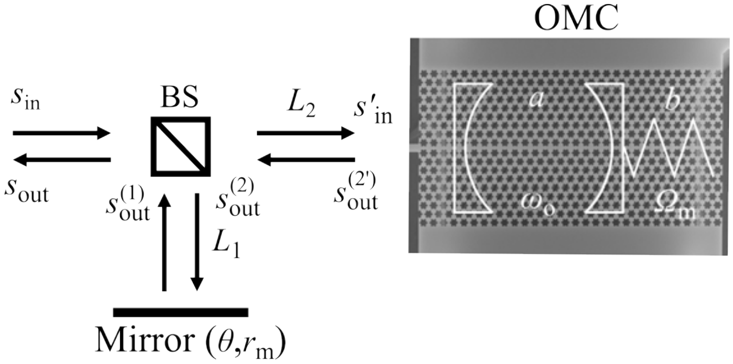

Figure A.8: Schematic image of the model

Here we consider the origin of the deviation that appears in the calibration tone method to determine g_0. We assume there is a residual back reflection from the fiber-waveguide coupling. We consider a model composed of a beam splitter (BS) and a mirror as well as our optomechanical crystal (OMC) explained in Fig. A.8.

The phase-modulated input field is expressed as:

$$s_{\rm in} = \left(s_0 + s_{\rm c}e^{-i\Omega_{\rm c}t} - s_{\rm c}e^{+i\Omega_{\rm c}t}\right)e^{-i\omega_{\rm L}t}, \tag{A.7}$$

where we define the laser frequency $\omega_{\rm L}$ and modulation frequency $\Omega_{\rm c}$. Here we assume the amplitude of each frequency component to be real $s_0, s_{\rm c} \in \mathbb{R}$. The Langevin equation of motion for the optical annihilation operator a is

$$\frac{d}{dt}a = -\left(i\omega_{\rm o} + \frac{\kappa}{2}\right)a + ig_0 a\left(b^\dagger + b\right) + \sqrt{\kappa_{\rm ex}}s_{\rm in}, \tag{A.8}$$

where b is the annihilation operator of the mechanical mode. Here, we take a Fourier-like expansion of optical and mechanical operators [**?**, 100],

$$a = \left(a_0 + a_- e^{-i\omega t} + a_+ e^{i\omega t}\right)e^{-i\omega_{\rm L}t}, \tag{A.9}$$
$$b^\dagger + b = x = x_0 + x_{\rm m}e^{-i\Omega_{\rm m}t} + x^*_{\rm m}e^{i\Omega_{\rm m}t}. \tag{A.10}$$

where $x = b^\dagger + b$ is a unitless mechanical displacement. We explicitly assume that the mechanical motion has only a frequency component at $\Omega_{\rm m}$

by postulating there is no overlap between mechanical and calibration tone ($|\Omega_\mathrm{m} - \Omega_\mathrm{c}| \gg \Gamma_\mathrm{m}$). Inserting the above expression into the equation of motion and solving for the steady states, we get

$$\bar{a}_0 = \sqrt{\kappa_\mathrm{ex}} s_0 \chi(0), \tag{A.11}$$

$$\bar{a}_-(\omega) = \begin{cases} \sqrt{\kappa_\mathrm{ex}} s_\mathrm{c} \chi(\Omega_\mathrm{c}) & \text{for} \quad \omega = \Omega_\mathrm{c} \\ i\sqrt{\kappa_\mathrm{ex}} g_0 x_\mathrm{m} s_0 \chi(0) \chi(\Omega_\mathrm{m}) & \text{for} \quad \omega = \Omega_\mathrm{m} \end{cases}, \tag{A.12}$$

$$\bar{a}_+(\omega) = \begin{cases} -\sqrt{\kappa_\mathrm{ex}} s_\mathrm{c} \chi(-\Omega_\mathrm{c}) & \text{for} \quad \omega = \Omega_\mathrm{c} \\ i\sqrt{\kappa_\mathrm{ex}} g_0 x_\mathrm{m}^* s_0 \chi(0) \chi(-\Omega_\mathrm{m}) & \text{for} \quad \omega = \Omega_\mathrm{m} \end{cases}, \tag{A.13}$$

where we define the optical susceptibility

$$\chi(\omega) \coloneqq \frac{1}{\kappa/2 - i(\Delta + \omega)}. \tag{A.14}$$

Here we used the displaced detuning $\Delta' \coloneqq \Delta + g_0 x_0$ from the bare detuning $\Delta \coloneqq \omega_\mathrm{L} - \omega_\mathrm{o}$ to account for the constant optical frequency shift, then redefine the detuning as $\Delta' \to \Delta$. Now we introduce the two paths; one leads to a mirror which corresponds to residual back reflection from the imperfect fiber-waveguide coupling or waveguide itself, and the other to our OMC. The output field from the mirror path $s_\mathrm{out}^{(1)}$ becomes

$$s_\mathrm{out}^{(1)} = r r_\mathrm{m} e^{i\theta} e^{2ikL_1} \left(s_0 + s_\mathrm{c} e^{-i(\Omega_\mathrm{c} t - 2\phi_1(\Omega_\mathrm{c}))} - s_\mathrm{c} e^{i(\Omega_\mathrm{c} t - 2\phi_1(\Omega_\mathrm{c}))} \right) e^{-i\omega_\mathrm{L} t}, \tag{A.15}$$

where we define

$$\phi_j(\Omega) \coloneqq \frac{nL_j}{c}\Omega \qquad \text{for} \qquad i = 1, 2, \tag{A.16}$$

$$k \coloneqq \frac{n\omega_\mathrm{L}}{c} \tag{A.17}$$

and refractive index n, phase shift by the mirror θ, reflectance of the mirror r_m, path length of each path $L_{j=1,2}$.

On the other hand, the fields impinging on the OMC obtain phase shifts in addition to those of eq.(A.7), by travelling the distance L_2. These phase shifts amount to:

$$s_0 e^{-i\omega_\mathrm{L} t} \to s_0 e^{-i\omega_\mathrm{L} t} e^{ikL_2}, \tag{A.18}$$

$$s_\mathrm{c} e^{-i(\omega_\mathrm{L} + \Omega_\mathrm{c})t} \to s_\mathrm{c} e^{-i(\omega_\mathrm{L} + \Omega_\mathrm{c})t} e^{i(kL_2 + \phi_2(\Omega_\mathrm{c}))}, \tag{A.19}$$

$$-s_\mathrm{c} e^{-i(\omega_\mathrm{L} - \Omega_\mathrm{c})t} \to -s_\mathrm{c} e^{-i(\omega_\mathrm{L} - \Omega_\mathrm{c})t} e^{i(kL_2 - \phi_2(\Omega_\mathrm{c}))}. \tag{A.20}$$

Therefore, the phase-shifted input field at the OMC, $s_{\text{in}}^{'}$, is given by

$$s_{\text{in}}^{'} = te^{ikL_2}\left(s_0 + s_{\text{c}}e^{i\phi_2(\Omega_{\text{c}})}e^{-i\Omega_{\text{c}}t} - s_{\text{c}}e^{-i\phi_2(\Omega_{\text{c}})}e^{+i\Omega_{\text{c}}t}\right)e^{-i\omega_{\text{L}}t}, \tag{A.21}$$

These modify the steady-state optical fields to:

$$\bar{a}_0 \to t\sqrt{\kappa_{\text{ex}}}\chi(0)s_0e^{ikL_2}, \tag{A.22}$$

$$\bar{a}_-(\omega) \to \begin{cases} t\sqrt{\kappa_{\text{ex}}}s_{\text{c}}\chi(\Omega_{\text{c}})e^{i(kL_2+\phi_2(\Omega_{\text{c}}))} & \text{for} \quad \omega = \Omega_{\text{c}} \\ it\sqrt{\kappa_{\text{ex}}}g_0x_{\text{m}}s_0\chi(0)\chi(\Omega_{\text{m}})e^{ikL_2} & \text{for} \quad \omega = \Omega_{\text{m}} \end{cases}, \tag{A.23}$$

$$\bar{a}_+(\omega) \to \begin{cases} -t\sqrt{\kappa_{\text{ex}}}s_{\text{c}}\chi(-\Omega_{\text{c}})e^{i(kL_2-\phi_2(\Omega_{\text{c}}))} & \text{for} \quad \omega = \Omega_{\text{c}} \\ it\sqrt{\kappa_{\text{ex}}}g_0x_{\text{m}}^*s_0\chi(0)\chi(-\Omega_{\text{m}})e^{ikL_2} & \text{for} \quad \omega = \Omega_{\text{m}} \end{cases}. \tag{A.24}$$

From the input-output theory and taking the transmission of the beamsplitter into account, the output field right after the OMC $s_{\text{out}}^{(2')}$ is,

$$s_{\text{out}}^{(2')}(\omega) = s_{\text{in}}' - \sqrt{\kappa_{\text{ex}}}a(\omega), \tag{A.25}$$

where $t = \sqrt{1-r^2}$. Therefore, we can calculate the calibration tone component of the output field from the OMC just before the beam splitter,

$$\begin{aligned} s_{\text{out}}^{(2)}(\Omega_{\text{c}}) = ts_{\text{c}}e^{i(-\omega_{\text{L}}t+2kL_2)}\Big[&\big\{1-\kappa_{\text{ex}}\chi(\Omega_{\text{c}})\big\}e^{-i(\Omega_{\text{c}}t-2\phi_2(\Omega_{\text{c}}))} \\ &- \big\{1-\kappa_{\text{ex}}\chi(-\Omega_{\text{c}})\big\}e^{i(\Omega_{\text{c}}t-2\phi_2(\Omega_{\text{c}}))}\Big], \end{aligned} \tag{A.26}$$

and the mechanical component,

$$\begin{aligned} s_{\text{out}}^{(2)}(\Omega_{\text{m}}) = -it\kappa_{\text{ex}}g_0\chi(0)s_0e^{i(-\omega_{\text{L}}t+2kL_2)}\Big[&x_{\text{m}}\chi(\Omega_{\text{m}})e^{-i(\Omega_{\text{m}}t-\phi_2(\Omega_{\text{m}}))} \\ &+ x_{\text{m}}^*\chi(-\Omega_{\text{m}})e^{i(\Omega_{\text{m}}t-\phi_2(\Omega_{\text{m}}))}\Big], \end{aligned} \tag{A.27}$$

and finally the carrier frequency component,

$$s_{\text{out}}^{(2)}(0) = te^{i(-\omega_{\text{L}}t+2kL_2)}\big\{1-\kappa_{\text{ex}}\chi(0)\big\}s_0. \tag{A.28}$$

The total output field we measure is the combined field after the beam splitter which is,

$$s_{\text{out}} = rs_{\text{out}}^{(1)} + ts_{\text{out}}^{(2)}. \tag{A.29}$$

From the above expressions for $s_{\mathrm{out}}^{(1)}$ and $s_{\mathrm{out}}^{(2)}$, we have the total output field for each frequency component as,

$$e^{i(\omega_{\mathrm{L}}t-2kL_2)}s_{\mathrm{out}}(0) = \left[r^2 r_{\mathrm{m}} e^{i(\theta+2k\Delta L)} + t^2\left\{1-\kappa_{\mathrm{ex}}\chi(0)\right\}\right] s_0 =: A, \tag{A.30}$$

$$\begin{aligned} e^{i(\omega_{\mathrm{L}}t-2kL_2)}s_{\mathrm{out}}(\Omega_{\mathrm{c}}) &= \left[r^2 r_{\mathrm{m}} e^{i(\theta+2k\Delta L+2\phi_1(\Omega_{\mathrm{c}}))} + t^2\left\{1-\kappa_{\mathrm{ex}}\chi(\Omega_{\mathrm{c}})\right\}e^{2i\phi_2(\Omega_{\mathrm{c}})}\right] s_{\mathrm{c}}e^{-i\Omega_{\mathrm{c}}t} \\ &\quad - \left[r^2 r_{\mathrm{m}} e^{i(\theta+2k\Delta L-2\phi_1(\Omega_{\mathrm{c}}))} + t^2\left\{1-\kappa_{\mathrm{ex}}\chi(-\Omega_{\mathrm{c}})\right\}e^{-2i\phi_2(\Omega_{\mathrm{c}})}\right] s_{\mathrm{c}}e^{i\Omega_{\mathrm{c}}t} \\ &=: B_{\mathrm{c}}e^{-i\Omega_{\mathrm{c}}t} + C_{\mathrm{c}}e^{i\Omega_{\mathrm{c}}t}, \end{aligned} \tag{A.31}$$

$$\begin{aligned} e^{i(\omega_{\mathrm{L}}t-2kL_2)}s_{\mathrm{out}}(\Omega_{\mathrm{m}}) &= -it^2\kappa_{\mathrm{ex}}g_0\chi(0)s_{\mathrm{c}}\Big\{x_{\mathrm{m}}\chi(\Omega_{\mathrm{m}})e^{-i(\Omega_{\mathrm{m}}t-\phi_2((\Omega_{\mathrm{m}}))} \\ &\qquad + x_{\mathrm{m}}^*\chi(-\Omega_{\mathrm{m}})e^{i(\Omega_{\mathrm{m}}t-\phi_2((\Omega_{\mathrm{m}}))}\Big\} \end{aligned} \tag{A.32}$$

$$=: B_{\mathrm{m}}e^{-i\Omega_{\mathrm{m}}t} + C_{\mathrm{m}}e^{i\Omega_{\mathrm{m}}t}. \tag{A.33}$$

where we define $\Delta L := L_1 - L_2$. The calibration frequency Ω_{c} component of intensity modulation of the output field is

$$\left|s_{\mathrm{out}}\right|^2(\Omega_{\mathrm{c}}) = s_{\mathrm{out}}(0)s_{\mathrm{out}}^*(\Omega_{\mathrm{c}}) + \mathrm{h.c.} \tag{A.34}$$

$$= \left(A^*B_{\mathrm{c}} + AC_{\mathrm{c}}^*\right)e^{-i\Omega_{\mathrm{c}}t} + \mathrm{h.c.} \tag{A.35}$$

Applying the same procedure for the mechanical frequency component, we have

$$\left|s_{\mathrm{out}}\right|^2(\Omega_{\mathrm{m}}) = s_{\mathrm{out}}(0)s_{\mathrm{out}}^*(\Omega_{\mathrm{m}}) + \mathrm{h.c.} \tag{A.36}$$

$$= \left(A^*B_{\mathrm{m}} + AC_{\mathrm{m}}^*\right)e^{-i\Omega_{\mathrm{m}}t} + \mathrm{h.c.} \tag{A.37}$$

To estimate the impact on g_0, we define the mechanics/calibration power ratio $\eta_g(\Delta)$:

$$\eta_g(\Delta) := \left|\frac{A^*B_{\mathrm{m}} + AC_{\mathrm{m}}^*}{A^*B_{\mathrm{c}} + AC_{\mathrm{c}}^*}\right|^2, \tag{A.38}$$

which is proportional to the measured g_0. We assume that the dynamical backaction is small enough so the mechanical linewidth and mechanical peak height are unchanged over detuning.

Fig. A.9 shows plots of $|A(\Delta)|^2$ and $\eta_g(\Delta)$ with parameters of $\omega_{\mathrm{o}}/2\pi$ = 195.55 THz, n = 3.05, ΔL = -140 μm, $\kappa_0/2\pi$ = 1.5 GHz, $\kappa_{\mathrm{ex}}/2\pi$ = 1 GHz, $\Omega_{\mathrm{m}}/2\pi$ = 7.65 GHz, and $\Omega_{\mathrm{c}}/2\pi$ = 7.65 GHz. Fig. A.9(a) corresponds to the

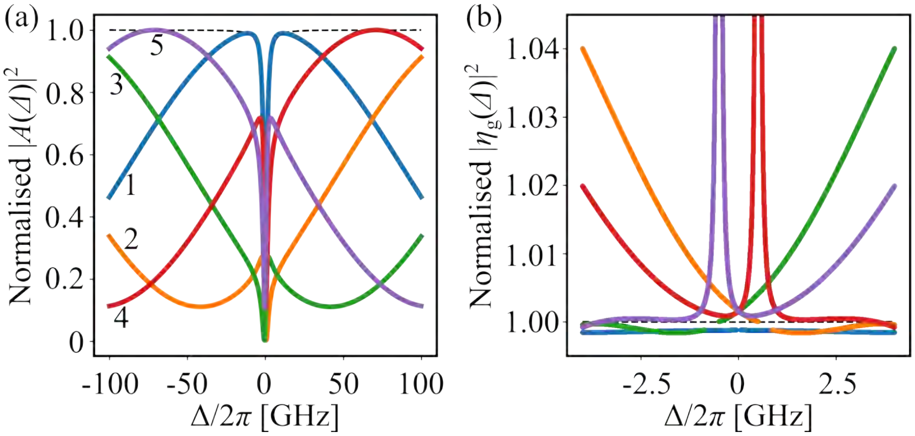

Figure A.9: (a)Reflection coefficient and (b) Mechanical/-calibration ratio η_g over detuning. Used parameters are $\omega_o/2\pi$ = 195.55 THz, n = 3.05, ΔL = -140 μm, $\kappa_0/2\pi$ = 1.5 GHz, $\kappa_{ex}/2\pi$ = 1 GHz, $\Omega_m/2\pi$ = 7.65 GHz, and $\Omega_c/2\pi$ = 7.65 GHz. For curves 1 to 5, $\theta - 2n\omega_L\Delta L/c$ = $0, 0.77\pi, -0.77\pi, 0.4\pi, -0.4\pi$ respectively. Dashed black curves are references with $r = 0$.

optical spectra in polarisation-matched (unmatched) conditions for curve 1 (curve 2-5). (b) plots the $\eta_g(\Delta)$ for each condition which is proportional to the measured g_0 [94]. As it shows, the measured g_0 depends on laser detuning if the optical spectrum is in polarisation unmatched condition regardless of dynamical backaction. Here we skip the points where the denominator of eq.(A.38) is small corresponding to the calibration tone being too small to detect. With the realistic parameters of our OMC device, we find the measured g_0 can change roughly 4% over ± 4 GHz of detuning depending hugely on the phase θ. This deviation is still smaller than what we have obtained from the measurements. A possible reason is that our model is oversimplified and other mechanisms give larger phase differences in the mechanical and calibration components. In the actual device, we may speculate the reflectance r of the BS is frequency-dependent or that there are multiple BSs, which may show more complex behaviour. Still, this result strongly suggests that the parasitic back reflection in the waveguide affects the measurement on g_0. Further optimization of the fibre-waveguide coupling will suppress the back reflection of propagating light.

In addition to the g_0 deviation, this model predicts the Fano-like reflection spectrum observed in Fig. A.7(c). To this end, we write $|s_{\text{out}}|^2$, disregarding the calibration tone and mechanical sidebands, i.e. retaining only

$$
\begin{aligned}
|A|^2 &= |s_0|^2 |r^2 r_m e^{i(\theta + 2k\Delta L)} + t^2 \left(1 - \kappa_{\text{ex}} \chi(0)\right)|^2 && \text{(A.39)} \\
&= |s_0|^2 \Bigg(\left(|r^2 r_m| + |t|^2 \cos(\theta + 2k\Delta L)\right)^2 && \text{(A.40)} \\
&\quad - 2|t|^4 \kappa (\eta_c - \eta_c^2) \frac{\frac{\kappa}{2}\left(1 + \frac{r^2 r_m}{|t|^2(1-\eta_c)} \cos(\theta + 2k\Delta L)\right) + \Delta \frac{r^2 r_m}{|t|^2(1-\eta_c)} \sin(\theta + 2k\Delta L)}{\left(\frac{\kappa}{2}\right)^2 + \Delta^2} \Bigg). && \text{(A.41)}
\end{aligned}
$$

Now, eq. (7.1) in the main text follows from eq. (A.39) by identifying

$$
\begin{aligned}
h &= |s_0|^2 \left(|r^2 r_m| + |t|^2 \cos(\theta + 2k\Delta L)\right)^2, && \text{(A.42)} \\
A &= 2|s_0|^2 |t|^4 \kappa (\eta_c - \eta_c^2), && \text{(A.43)} \\
q &= \frac{r^2 r_m}{|t|^2(1-\eta_c)} \sin(\theta + 2k\Delta L) && \text{(A.44)}
\end{aligned}
$$

by requiring $\cos(\theta + 2k\Delta L) = -\sin(\theta + 2k\Delta L)^2$. As is shown in Fig. A.9(a), eq. (A.39) exhibit similar Fano-like reflection spectra for a range of interferometer phases θ. In practice, we further approximate $h \approx$ const. by restricting our fitting region to the vicinity of the cavity resonance.

A.4 Output pulse shape from optomechanical systems

This appendix will theoretically explore the potential usage of an optomechanical system as a quantum memory and optical arbitrary wave generator(AWG) [101, 102]. In various fields of quantum optics, temporal waveforms of photons are of great importance as well as their quantum states. This is because they determine the efficiency of photon absorption by quantum systems such as atoms or qubits. Especially, exponentially increasing temporal waveforms of photons are considered a promising form which is effectively absorbed by other systems because these waveforms are the exact time-reversal of that of emitted photons (exponentially decaying function). We will explore the possible implementation of optomechanical systems and theoretically consider what operation we need to store and shape the photons.

A.4.1 Write Process of Memory

Here, we consider the write process of the memory protocol. The goal is to obtain the dynamic of the mechanical excitation when the single-photon and the red-detuned pulse are injected. As a possible state of the single-photon, we consider a Fock state [103]

$$|1_\xi\rangle = \int dt\ \xi(t)\hat{a}_{\mathrm{in}}^\dagger(t)\,|0\rangle\,, \tag{A.45}$$

where $\xi(t)$ is the temporal wave-packet of the input photon and is normalised $\int dt|\xi(t)|^2 = 1$. As for single-photons emitted from atoms or quantum dots, it is an exponentially decaying function. Notice that

$$\hat{a}_{\mathrm{in}}(t)\,|1_\xi\rangle = \xi(t)\,|0\rangle\,, \tag{A.46}$$

$$\langle 1_\xi|\,\hat{a}_{\mathrm{in}}^\dagger(t)\hat{a}_{\mathrm{in}}(t)\,|1_\xi\rangle = |\xi(t)|^2, \tag{A.47}$$

where we use the commutation relation $[\hat{a}_{\mathrm{in}}(t), \hat{a}_{\mathrm{in}}^\dagger(t')] = \delta(t - t')$. Starting from the Langevin equation for the time-dependent red-detuned Hamiltonian by keeping the input photon term,

$$\frac{d}{dt}\hat{a} = \left(-i\Omega_{\mathrm{m}} - \frac{\kappa}{2}\right)\hat{a} + ig(t)\hat{b} + \sqrt{\kappa_{\mathrm{ex}}}\hat{a}_{\mathrm{in}}(t), \tag{A.48}$$

$$\frac{d}{dt}\hat{b} = \left(-i\Omega_{\mathrm{m}} - \frac{\Gamma_{\mathrm{m}}}{2}\right)\hat{b} + ig(t)\hat{a}. \tag{A.49}$$

By assuming the linewidth of the photon is narrow enough so that the mechanical mode can follow the dynamics, and the optical mode decays faster than other modes, one can take the adiabatic approximation for the optical mode:

$$\frac{d}{dt}\hat{a} = 0 \tag{A.50}$$

$$\hat{a} = \frac{1}{i\Omega_\mathrm{m} + \kappa/2}\left(ig(t)\hat{b}(t) + \sqrt{\kappa_\mathrm{ex}}\hat{a}_\mathrm{in}(t)\right). \tag{A.51}$$

This is actually a strong assumption that; usually the linewidth of single-photons from quantum dots is roughly 200MHz [96] or more (although a sub-megaherz linewidth has been achieved in a rubidium atom [104]).

The equation of motion of the mechanical mode then becomes

$$\frac{d}{dt}\hat{b}(t) = -\left(\frac{\Gamma_\mathrm{eff}(t)}{2} + i\Omega_\mathrm{eff}(t)\right)\hat{b}(t) + h(t)\hat{a}_\mathrm{in}(t), \tag{A.52}$$

where $h(t) \coloneqq i\sqrt{\kappa_\mathrm{ex}}g(t)/(\kappa/2 + i\Omega_\mathrm{m})$ and

$$\Gamma_\mathrm{eff}(t) \coloneqq \Gamma_\mathrm{m} + \frac{g^2(t)\kappa}{\Omega_\mathrm{m}^2 + \kappa^2/4} \tag{A.53}$$

$$\Omega_\mathrm{eff}(t) \coloneqq \Omega_\mathrm{m} - \frac{g^2(t)\Omega_\mathrm{m}}{\Omega_\mathrm{m}^2 + \kappa^2/4}. \tag{A.54}$$

By solving this equation under the initial condition $\hat{b}(t_0) = 0$, we get

$$\begin{aligned}\hat{b}(t) =& \int_{t_0}^{t} dt''\ h(t'')\hat{a}_\mathrm{in}(t'') \exp\left[\int_{t_0}^{t''} dt' \left(i\Omega_\mathrm{eff}(t') + \frac{\Gamma_\mathrm{opt}(t')}{2}\right)\right] \\ &\times \exp\left[-\int_{t_0}^{t} dt' \left(i\Omega_\mathrm{eff}(t') + \frac{\Gamma_\mathrm{eff}(t')}{2}\right)\right] \\ =& e^{-P(t)-iQ(t)} \int_{t_0}^{t} dt''\ e^{P(t'')+iQ(t'')}h(t'')\hat{a}_\mathrm{in}(t''),\end{aligned} \tag{A.55}$$

where we define $P(t) \coloneqq \int_{t_0}^{t} \frac{\Gamma_\mathrm{eff}(t')}{2} dt'$ and $Q(t) \coloneqq \int_{t_0}^{t} \Omega_\mathrm{eff}(t')dt'$. Note that the temporal wave function of photon appears when one takes the mean value e.g., $\langle 1_\xi | \hat{a}_\mathrm{in}^\dagger(t)\hat{a}_\mathrm{in}(t) | 1_\xi \rangle = |\xi(t)|^2$. The number of phonons is given as

$$\langle \hat{b}^\dagger(t)\hat{b}(t)\rangle = e^{-2P(t)} \left| \int_{t_0}^{t} dt' e^{P(t')+iQ(t')}h(t')\xi(t') \right|^2. \tag{A.56}$$

Since in the input is a single-photon, eq.(A.56) should be as close as unity.

A.4.2 Read Process of Memory

The output field, on the other hand, is obtained from the input-output theorem as,

$$\begin{aligned}
\hat{a}_{\mathrm{out}}(t) =&\hat{a}_{\mathrm{in}}(t) - \sqrt{\kappa_{\mathrm{ex}}}\hat{a}(t) \\
=&\hat{a}_{\mathrm{in}}(t) - \frac{\sqrt{\kappa_{\mathrm{ex}}}}{i\Omega_{\mathrm{m}} + \kappa/2}\left\{ig(t)\hat{b}(t) + \sqrt{\kappa_{\mathrm{ex}}}\hat{a}_{\mathrm{in}}(t)\right\} \\
=&\frac{i\Omega_{\mathrm{m}} + (\kappa/2 - \kappa_{\mathrm{ex}})}{i\Omega_{\mathrm{m}} + \kappa/2}\hat{a}_{\mathrm{in}}(t) - h(t)\hat{b}(t) \\
=&r(-\Omega_{\mathrm{m}})\hat{a}_{\mathrm{in}}(t) \\
&- h(t)e^{-P(t)-iQ(t)}\int_{t_0}^{t} dt''\ e^{P(t'')+iQ(t'')}h(t'')\hat{a}_{\mathrm{in}}(t''),
\end{aligned} \tag{A.57}$$

where we define the reflection coefficient from the optical resonator as:

$$r(\Delta) := \frac{-i\Delta + (\kappa/2 - \kappa_{\mathrm{ex}})}{-i\Delta + \kappa/2}. \tag{A.58}$$

The output photon flux becomes

$$\begin{aligned}
&\langle\hat{a}_{\mathrm{out}}^{\dagger}(t)\hat{a}_{\mathrm{out}}(t)\rangle \\
=&|r(-\Omega_{\mathrm{m}})|^2|\xi(t)|^2 \\
&+ |h(t)|^2e^{-2P(t)}\left|\int_{t_0}^{t} dt' e^{P(t')+iQ(t')}h(t')\xi(t')\right|^2 \\
&+ 2\mathrm{Re}\Bigg[r(-\Omega_{\mathrm{m}})^*h(t)e^{-P(t)-iQ(t)}\xi^*(t) \\
&\qquad\times\int_{t_0}^{t} dt''\ e^{P(t'')+iQ(t'')}h(t'')\xi(t'')\Bigg]
\end{aligned} \tag{A.59}$$

Combining eq.(A.56) and eq.(A.59) the whole dynamics of both photon mode and the mechanical excitation are obtained.

A.4.3 AWG with an Optomechanical System

Here we think more simplified situation where the mechanical mode is already prepared in a single-phonon state. Then we discuss how to control the temporal mode of the output photon in the read-out process. We start with the linearised red-detuned Hamiltonian:

$$\hat{H}/\hbar = \Omega_\mathrm{m}\hat{a}^\dagger\hat{a} + \Omega_\mathrm{m}\hat{b}^\dagger\hat{b} - g(t)(\hat{a}\hat{b}^\dagger + \hat{a}^\dagger\hat{b}), \tag{A.60}$$

where $g(t) = g_0\sqrt{n_{\mathrm{cav}(t)}}$. We assume we can control the effective optomechanical coupling rate $g(t)$ by arbitrarily changing the power of the driving laser at detuning $\Delta = \Omega_\mathrm{m}$ thus the cavity photons $n_\mathrm{cav}(t)$ over time. A key to the optomechanical AWG is that the photon emission rate scales with $g(t)$.

From this Hamiltonian, the Langevin equation leads,

$$\frac{d}{dt}\hat{a} = \left(-i\Omega_\mathrm{m} - \frac{\kappa}{2}\right)\hat{a} + ig(t)\hat{b} + \sqrt{\kappa_\mathrm{ex}}\hat{a}_\mathrm{in}(t), \tag{A.61}$$

$$\frac{d}{dt}\hat{b} = \left(-i\Omega_\mathrm{m} - \frac{\Gamma_\mathrm{m}}{2}\right)\hat{b} + ig(t)\hat{a} + \sqrt{\Gamma_\mathrm{m}}\hat{f}_\mathrm{m}. \tag{A.62}$$

Now we assume that the time scale of the optical mode is much shorter than that of any other mode. Taking the adiabatic approximation and ignoring the noise terms,

$$\frac{d}{dt}\hat{a} = 0 \tag{A.63}$$

$$\hat{a} = \frac{ig(t)}{i\Omega_\mathrm{m} + \kappa/2}\hat{b} \tag{A.64}$$

Then the differential equation of the mechanical mode leads,

$$\begin{aligned}\frac{d}{dt}\hat{b}(t) &= -(i\Omega_\mathrm{m} + \kappa/2)\hat{b} - \frac{g^2(t)}{i\Omega_\mathrm{m} + \kappa/2}\hat{b} \\ &= -\left\{\left(\frac{\Gamma_\mathrm{m}}{2} + \frac{g^2(t)\kappa/2}{\Omega_\mathrm{m}^2 + \kappa^2/4}\right) + i\left(\Omega_\mathrm{m} - \frac{\Omega_\mathrm{m}g^2(t)}{\Omega_\mathrm{m}^2 + \kappa^2/4}\right)\right\}\hat{b}(t) \\ &:= -\left(\frac{\Gamma_\mathrm{eff}(t)}{2} + i\Omega_\mathrm{eff}(t)\right)\hat{b}(t).\end{aligned} \tag{A.65}$$

The solution of this differential equation is

$$\hat{b}(t) = \hat{b}(t_0)\exp\left[-\int_{t_0}^{t} dt'\left(\frac{\Gamma_\mathrm{eff}(t)}{2} + i\Omega_\mathrm{eff}(t)\right)\right]. \tag{A.66}$$

Note that the quantum feature of the mechanical mode doesn't really change over time as it's already determined by its initial state $\hat{b}(t_0)$. From the input-output theory, the output field $\hat{a}_{\text{out}}$ is given as

$$\begin{aligned}\hat{a}_{\text{out}}(t) &= \hat{a}_{\text{in}}(t) - \sqrt{\kappa_{\text{ex}}}\hat{a}(t) \\ &= \hat{a}_{\text{in}}(t) - i\frac{\sqrt{\kappa_{\text{ex}}}g(t)}{i\Omega_{\text{m}} + \kappa/2}\hat{b}(t).\end{aligned} \tag{A.67}$$

Let's think about a specific case where the mechanical mode is already excited and there is no input $\hat{a}_{\text{in}}(t) = 0$. The output photon flux is

$$\langle \hat{a}^\dagger_{\text{out}}(t)\hat{a}_{\text{out}}(t)\rangle = \frac{\kappa_{\text{ex}}|g(t)|^2}{\Omega_{\text{m}}^2 + \kappa^2/4}\exp\left(-\int_{t_0}^{t} dt'\ \Gamma_{\text{eff}}(t)\right)\langle \hat{b}^\dagger(t_0)\hat{b}(t_0)\rangle\,. \tag{A.68}$$

Here we define a unitless temporal function $F(t)$ as,

$$F(t) \coloneqq \frac{\kappa}{\Omega_{\text{m}}^2 + \kappa^2/4}\int_{t_0}^{t} dt\ g^2(t). \tag{A.69}$$

Then the photon flux becomes

$$\langle \hat{a}^\dagger_{\text{out}}(t)\hat{a}_{\text{out}}(t)\rangle = \eta\dot{F}(t)e^{-F(t)}\langle \hat{b}^\dagger(t_0)\hat{b}(t_0)\rangle\,, \tag{A.70}$$

where $\eta = \kappa_{\text{ex}}/\kappa$. If the desired temporal pulse shape is expressed as $S(t)$, then one can solve the differential equation below for $F(t)$:

$$\dot{F}(t)e^{-F(t)} = S(t), \tag{A.71}$$

$$S(t) = \frac{\langle \hat{a}^\dagger_{\text{out}}(t)\hat{a}_{\text{out}}(t)\rangle}{\eta\,\langle \hat{b}^\dagger(t_0)\hat{b}(t_0)\rangle} \tag{A.72}$$

As an example of $F(t) = \gamma t$ with a positive constant γ, it results in $S(t) \propto e^{-\gamma t}$ which is a canonical decaying output signal.

One of the most desired functions is exponentially increasing functions $S(t) = \alpha\left(e^{\gamma(t-t_0)} - 1\right)$, where α is a positive constant and t_0 is an initial time. This waveform will be suitable for the writing process of quantum memories thanks to its potentially high conversion efficiency. By solving the differential equation below,

$$\dot{F}(t)e^{-F(t)} = \alpha\left(e^{\gamma(t-t_0)} - 1\right), \tag{A.73}$$

where α is a constant with unit of $1/t$, the temporal function becomes

$$F(t) = -\log\left[C + \alpha t - \frac{\alpha}{\gamma}e^{\gamma(t-t_0)}\right]. \tag{A.74}$$

Imposing the initial condition $F(t_0) = 0$, we have

$$F(t) = -\log\left[1 + \alpha(t - t_0) + \frac{\alpha}{\gamma}\left(1 - e^{\gamma(t-t_0)}\right)\right]. \tag{A.75}$$

Therefore, the required optomechanical coupling to achieve this increasing exponential is

$$\begin{aligned} g(t) = g_0^2 n_{\mathrm{cav}}(t) \propto & \dot{F}(t) \qquad \text{(A.76)} \\ = & -\frac{\alpha\left\{1 - e^{\gamma(t-t_0)}\right\}}{1 + \alpha(t - t_0) + \frac{\alpha}{\gamma}\left\{1 - e^{\gamma(t-t_0)}\right\}}. \qquad \text{(A.77)} \end{aligned}$$

It should be noted that $F(t)$ and the denominator of eq.(A.76) diverges at the time t_{cutoff} given as

$$t_{\mathrm{cutoff}} = t_0 - \frac{1}{\alpha} - \frac{1}{\gamma} - \frac{W_0[-e^{(1+\gamma/\alpha)}]}{\gamma}, \tag{A.78}$$

where W_0 is the principal branch of the Lambert W function. This can be understood that we can not arbitrarily amplify the output photon, which is a quite reasonable result. With homodyne measurements, one can measure the quadrature of the output field $\hat{a}_{\mathrm{in}}^{\dagger}(t) \pm \hat{a}_{\mathrm{in}}(t)$. From (A.67) and $\hat{a}_{\mathrm{in}}(t) = 0$,

$$\begin{aligned} & \hat{a}_{\mathrm{out}}^{\dagger}(t) \pm \hat{a}_{\mathrm{out}}(t) \\ = & \frac{i\sqrt{\kappa_{\mathrm{ex}}}g(t)}{\Omega_{\mathrm{m}}^2 + \kappa^2/4}\left\{i\Omega_{\mathrm{m}}\left(\hat{b}^{\dagger}(t) \pm \hat{b}(t)\right) + \frac{\kappa}{2}\left(\hat{b}^{\dagger}(t) \mp \hat{b}(t)\right)\right\}, \end{aligned} \tag{A.79}$$

where $g(t)$ is given by eq.(A.76).

Bibliography

[1] T. H. Maiman. Stimulated Optical Radiation in Ruby. *Nature*, 187(4736):493–494, 1960.

[2] A. Ashkin, J. M. Dziedzic, J. E. Bjorkholm, and Steven Chu. Observation of a single-beam gradient force optical trap for dielectric particles. *Opt. Lett.*, 11(5):288, 1986.

[3] Jasper Chan, T. P.Mayer Alegre, Amir H. Safavi-Naeini, Jeff T. Hill, Alex Krause, Simon Gröblacher, Markus Aspelmeyer, and Oskar Painter. Laser cooling of a nanomechanical oscillator into its quantum ground state. *Nature*, 478(7367):89–92, 2011.

[4] Simon Gröblacher, Klemens Hammerer, Michael R. Vanner, and Markus Aspelmeyer. Observation of strong coupling between a micromechanical resonator and an optical cavity field. *Nature*, 460(7256):724–727, August 2009.

[5] David Mason, Junxin Chen, Massimiliano Rossi, Yeghishe Tsaturyan, and Albert Schliesser. Continuous force and displacement measurement below the standard quantum limit. *Nat. Phys.*, 15(8):745–749, 2019.

[6] Niccolò Fiaschi, Bas Hensen, Andreas Wallucks, Rodrigo Benevides, Jie Li, Thiago P.Mayer Alegre, and Simon Gröblacher. Optomechanical quantum teleportation. *Nature Photonics*, 15:817–821, 2021.

[7] H.-J. Briegel, W. Dür, J. I. Cirac, and P. Zoller. Quantum repeaters: The role of imperfect local operations in quantum communication. *Phys. Rev. Lett.*, 81:5932–5935, 1998.

[8] Brian Julsgaard, Jacob Sherson, J. Ignacio Cirac, Jaromír Fiurášek, and Eugene S. Polzik. Experimental demonstration of quantum memory for light. *Nature*, 432(7016):482–486, 2004.

[9] Zhen Sheng Yuan, Yu Ao Chen, Bo Zhao, Shuai Chen, Jörg Schmiedmayer, and Jian Wei Pan. Experimental demonstration of a BDCZ quantum repeater node. *Nature*, 454(7208):1098–1101, 2008.

[10] Andreas Wallucks, Igor Marinković, Bas Hensen, Robert Stockill, and Simon Gröblacher. A quantum memory at telecom wavelengths. *Nature Physics*, 16(7):772–777, 2020.

[11] Mads Bjerregaard Kristensen, Nenad Kralj, Eric C. Langman, and Albert Schliesser. Long-lived and efficient optomechanical memory for light. *Phys. Rev. Lett.*, 132:100802, 2024.

[12] Hengjiang Ren, Matthew H. Matheny, Gregory S. MacCabe, Jie Luo, Hannes Pfeifer, Mohammad Mirhosseini, and Oskar Painter. Two-dimensional optomechanical crystal cavity with high quantum cooperativity. *Nature Communications*, 11:3373, 2020.

[13] Sameer Sonar, Utku Hatipoglu, Srujan Meesala, David Lake, Hengjiang Ren, and Oskar Painter. High-Efficiency Low-Noise Optomechanical Crystal Photon-Phonon Transducers. *arXiv:2406.15701*, 2024.

[14] Katharina Schneider, Yannick Baumgartner, Simon Hönl, Pol Welter, Herwig Hahn, Dalziel J. Wilson, Lukas Czornomaz, and Paul Seidler. Optomechanics with one-dimensional gallium phosphide photonic crystal cavities. *Optica*, 6:577, 2019.

[15] Robert Stockill, Moritz Forsch, Grégoire Beaudoin, Konstantinos Pantzas, Isabelle Sagnes, Rémy Braive, and Simon Gröblacher. Gallium phosphide as a piezoelectric platform for quantum optomechanics. *Physical Review Letters*, 123, 2019.

[16] Robert Stockill, Moritz Forsch, Frederick Hijazi, Grégoire Beaudoin, Konstantinos Pantzas, Isabelle Sagnes, Rémy Braive, and Simon Gröblacher. Ultra-low-noise microwave to optics conversion in gallium phosphide. *Nature Communications*, 13(1):6583, 2022.

[17] Simon Hönl, Youri Popoff, Daniele Caimi, Alberto Beccari, Tobias J. Kippenberg, and Paul Seidler. Microwave-to-optical conversion with a gallium phosphide photonic crystal cavity. *Nat Commun*, 13(1):2065, 2022.

[18] Srujan Meesala, Steven Wood, David Lake, Piero Chiappina, Changchun Zhong, Andrew D. Beyer, Matthew D. Shaw, Liang Jiang, and Oskar Painter. Non-classical microwave–optical photon pair generation with a chip-scale transducer. *Nat. Phys.*, 20(5):871–877, 2024.

[19] Matt Eichenfield, Jasper Chan, Ryan M. Camacho, Kerry J. Vahala, and Oskar Painter. Optomechanical crystals. *Nature*, 462:78–82, 2009.

[20] Amir H. Safavi-Naeini and Oskar Painter. Design of optomechanical cavities and waveguides on a simultaneous bandgap phononic-photonic crystal slab. *Optics Express*, 18:14926, 2010.

[21] Amir H. Safavi-Naeini, Jeff T. Hill, Seán Meenehan, Jasper Chan, Simon Gröblacher, and Oskar Painter. Two-dimensional phononic-photonic band gap optomechanical crystal cavity. *Physical Review Letters*, 112:1–5, 2014.

[22] Hengjiang Ren, Tirth Shah, Hannes Pfeifer, Christian Brendel, Vittorio Peano, Florian Marquardt, and Oskar Painter. Topological phonon transport in an optomechanical system. *Nat Commun*, 13(1):3476, 2022.

[23] Jesse J. Slim, Clara C. Wanjura, Matteo Brunelli, Javier Del Pino, Andreas Nunnenkamp, and Ewold Verhagen. Optomechanical realization of the bosonic Kitaev chain. *Nature*, 627(8005):767–771, 2024.

[24] Johan Kolvik, Paul Burger, Joey Frey, and Raphaël Van Laer. Clamped and sideband-resolved silicon optomechanical crystals. *Optica*, 10(7):913, 2023.

[25] W. P. Su, J. R. Schrieffer, and A. J. Heeger. Solitons in Polyacetylene. *Phys. Rev. Lett.*, 42(25):1698–1701, 1979.

[26] A. Einstein, B. Podolsky, and N. Rosen. Can Quantum-Mechanical Description of Physical Reality Be Considered Complete? *Phys. Rev.*, 47(10):777–780, 1935.

[27] C. K. Hong, Z. Y. Ou, and L. Mandel. Measurement of subpicosecond time intervals between two photons by interference. *Phys. Rev. Lett.*, 59(18):2044–2046, 1987.

[28] Johannes KEPLER. *De cometis libelli tres.* Andreas Aperger, 1619.

[29] Dina Prialnik. Comets. In *Encyclopedia of Geology*, pages 160–173. Elsevier, 2021.

[30] A. Ashkin. Acceleration and Trapping of Particles by Radiation Pressure. *Phys. Rev. Lett.*, 24(4):156–159, 1970.

[31] Paolo Polimeno, Alessandro Magazzù, Maria Antonia Iatì, Francesco Patti, Rosalba Saija, Cristian Degli Esposti Boschi, Maria Grazia Donato, Pietro G. Gucciardi, Philip H. Jones, Giovanni Volpe, and Onofrio M. Maragò. Optical tweezers and their applications. *Journal of Quantitative Spectroscopy and Radiative Transfer*, 218:131–150, 2018.

[32] Albert Schliesser. Lecture note for advanced quantum optics course. 2023.

[33] Carlton M. Caves. Quantum-Mechanical Radiation-Pressure Fluctuations in an Interferometer. *Phys. Rev. Lett.*, 45(2):75–79, 1980.

[34] Markus Aspelmeyer, Tobias J. Kippenberg, and Florian Marquardt. Cavity optomechanics. *Reviews of Modern Physics*, 86(4):1391–1452, 2014.

[35] Stephen M. Barnett and Paul M. Radmore. *Methods in theoretical quantum optics.* Number 15 in Oxford series in optical and imaging sciences. Clarendon Press, Oxford, reprint edition, 2005.

[36] Niccolò Fiaschi, Bas Hensen, Andreas Wallucks, Rodrigo Benevides, Jie Li, Thiago P. Mayer Alegre, and Simon Gröblacher. Optomechanical quantum teleportation. *Nature Photonics*, 15(11):817–821, 2021.

[37] L. M. Duan, M. D. Lukin, J. I. Cirac, and P. Zoller. Long-distance quantum communication with atomic ensembles and linear optics. *Nature*, 414(6862):413–418, 2001.

[38] Steven G. Johnson, M. Ibanescu, M. A. Skorobogatiy, O. Weisberg, J. D. Joannopoulos, and Y. Fink. Perturbation theory for Maxwell's equations with shifting material boundaries. *Physical Review E - Statistical Physics, Plasmas, Fluids, and Related Interdisciplinary Topics*, 65(6):1–7, 2002.

[39] Hannes Pfeifer. *Silicon optomechanical crystals for arrays - tunability, disorder and 2D designs for low temperature experiments.* PhD thesis, der Friedrich-Alexander-Universität Erlangen-Nürnberg, 2018.

[40] Jasper Chan, Amir H. Safavi-Naeini, Jeff T. Hill, Seán Meenehan, and Oskar Painter. Optimized optomechanical crystal cavity with acoustic radiation shield. *Applied Physics Letters*, 101(8), 2012.

[41] Chin-Lin Chen. *Foundations for Guided-Wave Optics.* Wiley, 1 edition, 2006.

[42] Amnon Yariv and Pochi Yeh. *Optical Waves in Crystals: Propagation and Control of Laser Radiation.* Wiley, 1984.

[43] Matthew A. Hopcroft, William D. Nix, and Thomas W. Kenny. What is the Young's Modulus of Silicon? *J. Microelectromech. Syst.*, 19(2):229–238, 2010.

[44] Gregory S. MacCabe, Hengjiang Ren, Jie Luo, Justin D. Cohen, Hengyun Zhou, Alp Sipahigil, Mohammad Mirhosseini, and Oskar Painter. Nano-acoustic resonator with ultralong phonon lifetime. *Science*, 370(6518):840–843, 2020.

[45] Michael J. Burek, Justin D. Cohen, Seán M. Meenehan, Nayera El-Sawah, Cleaven Chia, Thibaud Ruelle, Srujan Meesala, Jake Rochman, Haig A. Atikian, Matthew Markham, Daniel J. Twitchen, Mikhail D. Lukin, Oskar Painter, and Marko Lončar. Diamond optomechanical crystals. *Optica*, 3(12):1404, 2016.

[46] J. R. Olson, R. O. Pohl, J. W. Vandersande, A. Zoltan, T. R. Anthony, and W. F. Banholzer. Thermal conductivity of diamond between 170 and 1200 k and the isotope effect. *Phys. Rev. B*, 47:14850–14856, 1993.

[47] Mete Atatüre, Dirk Englund, Nick Vamivakas, Sang-Yun Lee, and Joerg Wrachtrup. Material platforms for spin-based photonic quantum technologies. *Nat Rev Mater*, 3(5):38–51, 2018.

[48] M. H. Abobeih, J. Cramer, M. A. Bakker, N. Kalb, M. Markham, D. J. Twitchen, and T. H. Taminiau. One-second coherence for a single electron spin coupled to a multi-qubit nuclear-spin environment. *Nat Commun*, 9(1):2552, 2018.

[49] D. D. Sukachev, A. Sipahigil, C. T. Nguyen, M. K. Bhaskar, R. E. Evans, F. Jelezko, and M. D. Lukin. Silicon-Vacancy Spin Qubit in Diamond: A Quantum Memory Exceeding 10 ms with Single-Shot State Readout. *Phys. Rev. Lett.*, 119(22):223602, 2017.

[50] M. K. Bhaskar, D. D. Sukachev, A. Sipahigil, R. E. Evans, M. J. Burek, C. T. Nguyen, L. J. Rogers, P. Siyushev, M. H. Metsch, H. Park, F. Jelezko, M. Lončar, and M. D. Lukin. Quantum Nonlinear Optics with a Germanium-Vacancy Color Center in a Nanoscale Diamond Waveguide. *Phys. Rev. Lett.*, 118(22):223603, 2017.

[51] Preeti Ovartchaiyapong, Kenneth W. Lee, Bryan A. Myers, and Ania C. Bleszynski Jayich. Dynamic strain-mediated coupling of a single diamond spin to a mechanical resonator. *Nat Commun*, 5(1):4429, 2014.

[52] J. Teissier, A. Barfuss, P. Appel, E. Neu, and P. Maletinsky. Strain Coupling of a Nitrogen-Vacancy Center Spin to a Diamond Mechanical Oscillator. *Phys. Rev. Lett.*, 113(2):020503, 2014.

[53] Byunggi Kim, Hodaka Kurokawa, Katsuta Sakai, Kazuki Koshino, Hideo Kosaka, and Masahiro Nomura. Diamond optomechanical cavity with a color center for coherent microwave-to-optical quantum interfaces. *Phys. Rev. Applied*, 20(4):044037, 2023.

[54] F. Fung, E. Rosenfeld, J. D. Schaefer, A. Kabcenell, J. Gieseler, T. X. Zhou, T. Madhavan, N. Aslam, A. Yacoby, and M. D. Lukin. Toward Programmable Quantum Processors Based on Spin Qubits with Mechanically Mediated Interactions and Transport. *Phys. Rev. Lett.*, 132(26):263602, 2024.

[55] Graham Joe, Cleaven Chia, Benjamin Pingault, Michael Haas, Michelle Chalupnik, Eliza Cornell, Kazuhiro Kuruma, Bartholomeus Machielse, Neil Sinclair, Srujan Meesala, and Marko Lončar. High Q -Factor Diamond Optomechanical Resonators with Silicon Vacancy Centers at Millikelvin Temperatures. *Nano Lett.*, 24(23):6831–6837, 2024.

[56] Krishna C. Balram, Marcelo Davanço, Ju Young Lim, Jin Dong Song, and Kartik Srinivasan. Moving boundary and photoelastic coupling in gaas optomechanical resonators. *Optica*, 1(6):414–420, 2014.

[57] Krishna C. Balram, Marcelo I. Davanço, Jin Dong Song, and Kartik Srinivasan. Coherent coupling between radiofrequency, optical and acoustic waves in piezo-optomechanical circuits. *Nature Photon*, 10(5):346–352, 2016.

[58] Moritz Forsch, Robert Stockill, Andreas Wallucks, Igor Marinković, Claus Gärtner, Richard A. Norte, Frank van Otten, Andrea Fiore, Kartik Srinivasan, and Simon Gröblacher. Microwave-to-optics conversion using a mechanical oscillator in its quantum ground state. *Nature Physics*, 16(1):69–74, 2020.

[59] A.I. Ekimov, Al.L. Efros, and A.A. Onushchenko. Quantum size effect in semiconductor microcrystals. *Solid State Communications*, 56(11):921–924, 1985.

[60] Peter Lodahl, Sahand Mahmoodian, and Soren Stobbe. Interfacing single photons and single quantum dots with photonic nanostructures. *Reviews of Modern Physics*, 87(2):347–400, 2015.

[61] Matthew Mitchell, Aaron C. Hryciw, and Paul E. Barclay. Cavity optomechanics in gallium phosphide microdisks. *Applied Physics Letters*, 104(14):141104, 2014.

[62] M. F. Colombano, G. Arregui, N. E. Capuj, A. Pitanti, J. Maire, A. Griol, B. Garrido, A. Martinez, C. M. Sotomayor-Torres, and D. Navarro-Urrios. Synchronization of Optomechanical Nanobeams by Mechanical Interaction. *Physical Review Letters*, 123(1):17402, 2019. Publisher: American Physical Society.

[63] Jasper Chan, Matt Eichenfield, Ryan Camacho, and Oskar Painter. Optical and mechanical design of a “zipper” photonic crystal optomechanical cavity. *Opt. Express*, 17(5):3802–3817, 2009.

[64] Rhys G. Povey, Ming-Han Chou, Gustav Andersson, Christopher R. Conner, Joel Grebel, Yash J. Joshi, Jacob M. Miller, Hong Qiao, Xuntao Wu, Haoxiong Yan, and Andrew N. Cleland. Two-dimensional optomechanical crystal resonator in gallium arsenide. *Phys. Rev. Appl.*, 21:014015, 2024.

[65] Yannick Seis, Thibault Capelle, Eric Langman, Sampo Saarinen, Eric Planz, and Albert Schliesser. Ground state cooling of an ultracoherent electromechanical system. *Nat Commun*, 13(1):1507, 2022.

[66] COMSOL Multiphysics® v. 5.6. www.comsol.com. COMSOL AB, Stockholm, Sweden.

[67] Y.K. Yo urtçu, A.J. Miller, and G.A. Saunders. Pressure dependence of elastic behaviour and force constants of GaP. *Journal of Physics and Chemistry of Solids*, 42(1):49–56, 1981.

[68] Yurii A. Vlasov, Martin O’Boyle, Hendrik F. Hamann, and Sharee J. McNab. Active control of slow light on a chip with photonic crystal waveguides. *Nature*, 438(7064):65–69, 2005.

[69] Yoshihiro Akahane, Takashi Asano, Bong-Shik Song, and Susumu Noda. High-Q photonic nanocavity in a two-dimensional photonic crystal. *Nature*, 425(6961):944–947, 2003.

[70] Yoshihiro Akahane, Takashi Asano, Bong-Shik Song, and Susumu Noda. Fine-tuned high-Q photonic-crystal nanocavity. *Opt. Express*, 13(4):1202, 2005.

[71] Paul E. Barclay, Kartik Srinivasan, Matthew Borselli, and Oskar Painter. Efficient input and output fiber coupling to a photonic crystal waveguide. *Opt. Lett.*, 29(7):697, 2004.

[72] Kartik Srinivasan, Paul E. Barclay, Matthew Borselli, and Oskar Painter. Optical-fiber-based measurement of an ultrasmall volume high- Q photonic crystal microcavity. *Phys. Rev. B*, 70(8):081306, 2004.

[73] B. G. Mytsyk, N. M. Demyanyshyn, and O. M. Sakharuk. Elasto-optic effect anisotropy in gallium phosphide crystals. *Appl. Opt.*, 54(28):8546, 2015.

[74] David K. Biegelsen. Photoelastic tensor of silicon and the volume dependence of the average gap. *Phys. Rev. Lett.*, 32(21):1196–1199, 1974.

[75] T. G. Tiecke, K. P. Nayak, J. D. Thompson, T. Peyronel, N. P. de Leon, V. Vuletić, and M. D. Lukin. Efficient fiber-optical interface for nanophotonic devices. *Optica*, 2(2):70, 2015.

[76] Michael J. Burek, Charles Meuwly, Ruffin E. Evans, Mihir K. Bhaskar, Alp Sipahigil, Srujan Meesala, Bartholomeus MacHielse, Denis D. Sukachev, Christian T. Nguyen, Jose L. Pacheco, Edward Bielejec, Mikhail D. Lukin, and Marko Lončar. Fiber-coupled diamond quantum nanophotonic interface. *Physical Review Applied*, 8(2), 2017.

[77] Timothy P. McKenna, Rishi N. Patel, Jeremy D. Witmer, Raphaël Van Laer, Joseph A. Valery, and Amir H. Safavi-Naeini. Cryogenic packaging of an optomechanical crystal. *Optics Express*, 27:28782, 2019.

[78] Beibei Zeng, Chawina De-Eknamkul, Daniel Assumpcao, Dylan Renaud, Zhuoxian Wang, Daniel Riedel, Jeonghoon Ha, Carsten Robens, David Levonian, Mikhail Lukin, Ralf Riedinger, Mihir Bhaskar, Denis Sukachev, Marko Loncar, and Bart Machielse. Cryogenic packaging of nanophotonic devices with a low coupling loss <1 dB. *Applied Physics Letters*, 123(16):161106, 2023.

[79] Andreas W W Ludwig. Topological phases: classification of topological insulators and superconductors of non-interacting fermions, and beyond. *Phys. Scr.*, T168:014001, 2016.

[80] Eric J. Meier, Fangzhao Alex An, and Bryce Gadway. Observation of the topological soliton state in the Su–Schrieffer–Heeger model. *Nat Commun*, 7(1):13986, 2016.

[81] Andrea Blanco-Redondo, Imanol Andonegui, Matthew J. Collins, Gal Harari, Yaakov Lumer, Mikael C. Rechtsman, Benjamin J. Eggleton, and Mordechai Segev. Topological Optical Waveguiding in Silicon and

the Transition between Topological and Trivial Defect States. *Phys. Rev. Lett.*, 116(16):163901, 2016.

[82] Dawn T. H. Tan. Topological Silicon Photonics. *Advanced Photonics Research*, 2(9):2100010, 2021.

[83] Ling Lu, John D. Joannopoulos, and Marin Soljačić. Topological photonics. *Nature Photon*, 8(11):821–829, 2014.

[84] Alexis Hotte-Kilburn and Pablo Bianucci. Implementation of the SSH model in an optical ring resonator. *J. Opt.*, 26(6):065006, 2024.

[85] Paul Burger, Joey Frey, Johan Kolvik, David Hambraeus, and Raphaël Van Laer. Design of a release-free piezo-optomechanical quantum transducer. *arXiv:2408.15134*, 2024.

[86] Hao Tong, Shengyan Liu, Mengdi Zhao, and Kejie Fang. Observation of phonon trapping in the continuum with topological charges. *Nat Commun*, 11(1):5216, 2020.

[87] Shengyan Liu, Hao Tong, and Kejie Fang. Optomechanical crystal with bound states in the continuum. *Nature Communications*, 13(1):3187, 2022.

[88] G. Sagué, E. Vetsch, W. Alt, D. Meschede, and A. Rauschenbeutel. Cold-Atom Physics Using Ultrathin Optical Fibers: Light-Induced Dipole Forces and Surface Interactions. *Phys. Rev. Lett.*, 99(16):163602, 2007.

[89] Limin Tong, Rafael R. Gattass, Jonathan B. Ashcom, Sailing He, Jingyi Lou, Mengyan Shen, Iva Maxwell, and Eric Mazur. Subwavelength-diameter silica wires for low-loss optical wave guiding. *Nature*, 426(6968):816–819, 2003.

[90] Jonathan M. Ward, Danny G. O'Shea, Brian J. Shortt, Michael J. Morrissey, Kieran Deasy, and Síle G. Nic Chormaic. Heat-and-pull rig for fiber taper fabrication. *Review of Scientific Instruments*, 77(8):083105, 2006.

[91] J. M. Ward, A. Maimaiti, Vu H. Le, and S. Nic Chormaic. Contributed Review: Optical micro- and nanofiber pulling rig. *Review of Scientific Instruments*, 85(11):111501, 2014.

[92] Donghwa Lee, Kwang Jo Lee, Jin-Hun Kim, Kyungdeuk Park, Dongjin Lee, Yoon-Ho Kim, and Heedeuk Shin. Fabrication method for ultra-long optical micro/nano-fibers. *Current Applied Physics*, 19(12):1334–1337, 2019.

[93] Tal Carmon, Lan Yang, and Kerry J. Vahala. Dynamical thermal behavior and thermal self-stability of microcavities. *Optics Express*, 12(20):4742, 2004.

[94] M. L. Gorodetsky, A. Schliesser, G. Anetsberger, S. Deleglise, and T. J. Kippenberg. Determination of the vacuum optomechanical coupling rate using frequency noise calibration. *Optics Express*, 18:23236, 2010.

[95] W. W. Wasserman, R. A. Harrison, G. I. Harris, A. Sawadsky, Y. L. Sfendla, W. P. Bowen, and C. G. Baker. Cryogenic and hermetically sealed packaging of photonic chips for optomechanics. *Opt. Express*, 30(17):30822, 2022.

[96] Freja T. Pedersen, Ying Wang, Cecilie T. Olesen, Sven Scholz, Andreas D. Wieck, Arne Ludwig, Matthias C. Löbl, Richard J. Warburton, Leonardo Midolo, Ravitej Uppu, and Peter Lodahl. Near transform-limited quantum dot linewidths in a broadband photonic crystal waveguide. *ACS Photonics*, 7(9):2343–2349, 2020.

[97] Beatrice Da Lio, Carlos Faurby, Xiaoyan Zhou, Ming Lai Chan, Ravitej Uppu, Henri Thyrrestrup, Sven Scholz, Andreas D. Wieck, Arne Ludwig, Peter Lodahl, and Leonardo Midolo. A Pure and Indistinguishable Single-Photon Source at Telecommunication Wavelength. *Adv Quantum Tech*, 5(5):2200006, 2022.

[98] Sho Tamaki, Mads Bjerregaard Kristensen, Théo Martel, Rémy Braive, and Albert Schliesser. A two-dimensional gallium phosphide optomechanical crystal in the resolved-sideband regime. *arXiv:2408.12474*, 2024.

[99] Sho Tamaki, Tomohiro Yokoyama, and Hajime Ishihara. Nonlocal inelastic scattering of light: Enhanced and noiseless signals in remote-coupled optomechanical systems. *arXiv:2110.00193*, 2021.

[100] M. J. Woolley and A. A. Clerk. Two-mode squeezed states in cavity optomechanics via engineering of a single reservoir. *Phys. Rev. A*, 89:063805, 2014.

[101] Steven T. Cundiff and Andrew M. Weiner. Optical arbitrary waveform generation. *Nature Photon*, 4(11):760–766, 2010.

[102] Kan Takase, Akito Kawasaki, Byung Kyu Jeong, Takahiro Kashiwazaki, Takushi Kazama, Koji Enbutsu, Kei Watanabe, Takeshi Umeki, Shigehito Miki, Hirotaka Terai, Masahiro Yabuno, Fumihiro China, Warit Asavanant, Mamoru Endo, Jun-ichi Yoshikawa, and Akira Furusawa. Quantum arbitrary waveform generator. *Sci. Adv.*, 8(43):eadd4019, 2022.

[103] Warwick P Bowen and Gerard J Milburn. *Quantum optomechanics.* CRC press, 2015.

[104] Markus Rambach, Aleksandrina Nikolova, Till J. Weinhold, and Andrew G. White. Sub-megahertz linewidth single photon source. *APL Photonics*, 1(9):096101, 2016.